

**Experimental Determinations and Modelling of the Viscosity of  
Multicomponent Natural Silicate Melts: Volcanological  
Implications.**

INAUGURALDISSERTATION  
ZUR ERLANGUNG DES DOKTORGRADES  
DER FAKULTÄT FÜR GEOWISSENSCHAFTEN  
DER LUDWIG-MAXIMILIANS-UNIVERSITÄT  
MÜNCHEN

VORGELEGT VON  
DANIELE GIORDANO

MÜNCHEN, 2002

Die vorliegende Arbeit wurde in der Zeit von Mai 1997 bis August 2000 am Bayerischen Forschungsinstitut für experimentelle Geochemie und Geophysik (BGI, Universität Bayreuth) und am Institut für Mineralogie, Petrologie und Geochemie der Ludwig-Maximilians-Universität, München angefertigt.

Tag des Rigorosums: 15. Juli 2002

Promotionskommissions-  
vorsizender

Prof. Dr. H. Igel

Referent:

Prof. Dr. D. B. Dingwell

Koreferent:

Prof. Dr. L. Masch

Ubrige Promotions-  
Kommissionsmitglieder

Prof. Dr.K.Weber-Diefenbach

## Acknowledgements

Thanks to Don Dingwell for originally proposing this subject and helping me along the way. You have been a perfect guide. Thanks for reading the proof and making suggestions that improved this work. Alex, you also helped me a lot to improve my english and you strongly supported me.....even though you threw me out of your office countless times. You're a friend. Cheers to Kelly and Joe: good friends and teachers.

Thanks to Prof. Steve Mackwell and Prof. Dave Rubie who gently gave me the opportunity to use the laboratories at Bayerisches Geoinstitut.

Cheers to everyone who I shared an office with and contributed somehow (scientifically and spiritually) to create a stimulating environment, at BGI and IMPG, particularly Marcel, Joe, Ulli, Oliver, Philippe, Conrad, Bettina, Wolfgang Schmitt, Kai-Uwe Hess.

Thanks to Conrad, Cliff Shaw and Claudia Romano, my trainers in the micropenetration and piston cylinder techniques.

Cheers to Harald Behrens who kindly invited me to the IM – Hannover University to use the Karl-Fisher Titration device.

Thanks to Hans Keppler, John Sowerby and Nathalie Bolfan-Casanova for showing me how to use FTIR.

I particularly appreciated the accurate work carried out by Hubert Schulze, Georg Hermannsdörfer, Oscar Leitner and Heinz Fischer in the BGI, whose technical suggestions and precise sample preparation made my work much easier.

Thanks to Detlef Krausse for your help in solving all the computer problems and providing the electron microprobe analyses.

Gisela Baum, Evi Löbl, Ute Hetschger and Lydia Arnold, I have to thank you for your kindness and help in sorting out the numerous beurocratic affairs.

Un ringraziamento sincero a Paolo Papale, Claudia Romano e Mauro Rosi per il loro supporto e contributo scientifico.

Un abbraccio a tutte le persone che grazie alla loro simpatia ed amicizia hanno reso il mio lavoro più leggero, contribuendo, ciascuno a proprio modo, a trasferirmi l'energia necessaria a perseguire questo obiettivo. In particolare: Marilena, Edoardo, Claudia, Ivan, Francisco, Pietro, Nathalie, Martin, Giuliano.

A mio padre, mia madre, Alessio e Nicola, che non mi hanno mai fatto mancare il loro totale supporto ed i buoni consigli.

Ad Erika, Martina ed Elisa, i cui occhi e sorrisi hanno continuamente illuminato la mia strada.

## Zusammenfassung

Gegenstand dieser Arbeit ist die Bestimmung und Modellierung der Viskositäten silikatischer Schmelzen mit unterschiedlichen, in der Natur auftretenden Zusammensetzungen.

Chemische Zusammensetzung, Temperatur, Druck, der Gehalt an Kristallen und Xenolithen, der Grad der Aufschäumung und der Gehalt an gelösten volatilen Stoffen sind alles Faktoren, die die Viskosität einer silikatischen Schmelze in unterschiedlichem Maße beeinflussen. Drücke bis 20 kbar und Festpartikelgehalte unter 30 Volumenprozent haben einen geringeren Effekt als Temperatur, Zusammensetzung oder Wassergehalt (Marsh, 1981, Pinkerton and Stevenson, 1992, Dingwell et al., 1993, Lejeune and Richet, 1995). Bei Eruptionstemperatur führen z.B. das Hinzufügen von 30 Volumenprozent Kristallen, die Verringerung des Wassergehaltes um 0,1 Gewichtsprozent oder die Erniedrigung der Temperatur um 30 K zu einer identischen Erhöhung der Viskosität (Pinkerton and Stevenson, 1992).

Im Rahmen dieser Arbeit wurde die Viskosität verschiedener vulkanischer Produkte von wichtigen, potenziell gefährlichen Vulkangebieten ( Vesuv, Flegräische Felder, Etna – Italien; Teide – Teneriffa; Povocao – Azoren; Eifel – Deutschland; Unzen – Japan) untersucht. Bimsablagerungen, pyroklastische Ströme und Lavaströme von jedem dieser Vulkangebiete wurden beprobt. Diese Proben decken einen kompositionellen Bereich von Basanit bis Phonolit, und von Dazit bis Trachyt ab.

Um eine Grundlage für die Modellierung der Newtonschen Viskosität in Abhängigkeit von chemischer Zusammensetzung und Temperatur zu schaffen, wurden ausführliche Experimente durchgeführt. Chemische Zusammensetzung, Viskosität und Dichte ausgewählter Proben wurden bei unterschiedlichen Wassergehalten bestimmt. Die experimentelle Vorgehensweise beinhaltete die Bestimmung der Viskosität trockener und wasserhaltiger Schmelzen unter Superliquidus und unterkühlten Bedingungen. Im Hochtemperaturbereich (1050-1600 °C) wurden Viskositäten zwischen  $10^{-0.5}$  und  $10^5$  Pas mit einer Konzentrischer-Zylinder Apparatur gemessen. Messungen an trockenen und wasserhaltigen Proben im Bereich tiefer Temperatur (616-860 °C) und hoher Viskosität ( $10^{8.5}$

–  $10^{12}$  Pa·s) wurden an abgeschreckten Hochtemperaturviskosimetrie Proben mit einem Mikropenetrationsdilatometer durchgeführt. Die verwendeten Apparaturen wurden an Hand von Standards kalibriert. Hierfür wurden NBS 711 vom National Bureau of Standards und DGG 1 (Natrium-Calcium-Silizium Glas) der Deutschen Glastechnischen Gesellschaft verwendet.

Wasserhaltige Proben für die Messung im unterkühlten Zustand wurden bei 1100-1600 °C und 10 kbar in einer Kolbenzylinder Apparatur synthetisiert. Die absoluten Wassergehalte wurden mittels Karl Fischer Titrationsmethode (KFT) am Institut für Mineralogie der Universität Hannover bestimmt, und lagen zwischen 0 und 3,78 Gewichtsprozent. Durch Fourier-Transformation Infrarot Spektroskopie (FTIR) wurde jeweils vor und nach den Experimenten überprüft, ob die Wasserverteilung in den Proben homogen ist und dass kein Wasser verloren wurde. Die Hauptelementzusammensetzung der trockenen, wiederaufgeschmolzenen Proben wurde an einer Elektronenstrahl Mikrosonde des Bayerischen Geoinstituts der Universität Bayreuth bestimmt. Von einigen natürlichen Proben wurde nur die glasige Matrix experimentell untersucht. An diesen Proben wurden vor und nach den Experimenten Vergleichsmessungen mit der Mikrosonde durchgeführt. Die Ergebnisse dieser Messungen belegen dass beim Aufschmelzen auch sehr alkalireicher Proben keine Alkalimetalle verloren gehen.

Kalorimetrische Glasübergangstemperaturen wurden mit einem Dynamischen Differenz-Kalorimeter (DSC) bestimmt. Die Kalorimetrische Glasübergangstemperatur ist definiert als die Temperatur bei der eine Probe die höchste spezifische Wärmekapazität bei konstantem Umgebungsdruck besitzt.

Die Newtonsche Viskosität silikatischer Schmelzen wurde im Bereich zwischen  $10^{-1}$  und  $10^{11.6}$  Pas untersucht und mit einer nicht linearen TVF Gleichung mit drei Parametern ( $A_{TVF}$ ,  $B_{TVF}$  and  $T_0$ ) modelliert. Um eine breite Anwendbarkeit des Modells zu gewährleisten, wurden die im Rahmen dieser Arbeit gewonnenen Daten auch mit älteren Daten von Whittington et al. (2000, 2001); Dingwell et al. (1996); Neuville et al. (1993) kombiniert.

Es zeigen sich starke numerische Korrelationen zwischen den Parametern  $A_{TVF}$ ,  $B_{TVF}$  und  $T_0$ , die den Zusammensetzungseffekt maskieren. Viele verschiedene Werte für  $A_{TVF}$ ,  $B_{TVF}$

und  $T_0$  können eingesetzt werden, um individuelle Datensätze zu beschreiben. Dies trifft auch für Datensätze zu, die umfangreich sind, sorgfältig gemessen wurden und einen großen Bereich experimenteller Bedingungen abdecken. Sogenannte "strong liquids" (Flüssigkeiten die nicht oder nur leicht von einem idealen Arrhenius Verhalten abweichen) lassen einen großen Bereich von Absolutwerten für  $A_{TVF}$ ,  $B_{TVF}$  und  $T_0$  zu, wohingegen sogenannte "fragile liquids" (Flüssigkeiten die eine starke Abweichung von einem idealen Arrhenius Verhalten zeigen) die möglichen Werte für  $A_{TVF}$ ,  $B_{TVF}$  und  $T_0$  stark einschränken. Deshalb sollten Strategien zur Modellierung von kompositionellen Effekten auf die Untersuchung von "fragile liquids" ausgelegt werden.

Die Beziehungen zwischen verschiedenen Parametern, die die Abweichung von einem Arrhenius Verhalten charakterisieren (z.B. die Fragilität  $F$ ), wurden mittels des strukturbezogenen Parameters  $NBO/T$  beschrieben.  $NBO/T$  ist ein Maß für den Grad der Polymerisierung einer silikatischen Schmelze, das heißt das Verhältnis zwischen sogenannten Trennstellensauerstoffen (non-bridging oxygens, NBO) und tetraedrisch koordinierten Kationen (T) (Mysen, 1988). Das Hinzufügen von netzwerkmodifizierenden Elementen zu einer vollkommen polymerisierten Flüssigkeit ( $NBO/T = 0$ ) führt zu einem drastischen Anstieg der Fragilität. Bei  $NBO/T$  Werten über 0,4-0,5 haben zusätzliche Netzwerkmodifizierer nur einen geringen Einfluß auf die Fragilität. Dies lässt den Schluß zu, dass die starke Veränderung der Beziehung von  $NBO/T$  und Fragilität auf einer plötzlichen Veränderung der konfigurationellen Eigenschaften und rheologischen Regime durch die Zugabe von netzwerkmodifizierenden Elementen beruht.

Die TVF Parametrisierung wurde auch dazu benutzt, ein vorhersagendes Modell für die Viskosität von Arrhenius- und nicht-Arrhenius Flüssigkeiten zu erstellen. Dieses Modell berücksichtigt den Einfluß der chemischen Zusammensetzung durch einen sogenannten "structure modifier" (SM) Parameter. SM ist die Summe der Molprozent der Oxide von Ca, Mg, Mn, Na, K, und der Hälfte von  $Fe_{tot}$ . Diese Elemente wurden gewählt, da sie in einer silikatischen Schmelze als Netzwerkmodifizierer wirken (Mysen, 1988). Dieser Ansatz wird

durch die hohe Erfolgsquote des Modells gerechtfertigt, das sämtliche im Bereich von 700-1600 °C gemessenen Werte von  $\log \eta$  auf 10 Prozent genau reproduziert.

Im Zusammenhang mit dem SM-Parameter konnte eine weitere wichtige Beobachtung gemacht werden. Trägt man Viskosität (bestimmt bei konstanter Temperatur) und SM-Parameter verschiedener Proben mit unterschiedlichen chemischen Zusammensetzungen in einem Diagramm gegeneinander auf, zeigt sich ein nicht linearer Trend. Dieser Trend bezeichnet einen systematischen Zusammenhang zwischen der Viskosität einer Schmelze und deren Gehalt an netzwerkmodifizierenden Elementen. Dieser Kurvenverlauf zeigt zudem eine annähernd parallele Verschiebung mit steigender Temperatur (zwischen 700 und 1600 °C) hin zu niedrigeren Viskositäten. Diese Parallelität deutet daraufhin, dass die Temperatur keinen großen Einfluß auf den kumulativen Effekt der netzwerkmodifizierenden Elemente hat.

Eine Kombination kalorimetrischer und viskosimetrischer Daten ermöglicht eine Vorhersage der Viskosität bei der Glasübergangstemperatur, d.h. bei der Temperatur bei der sich das rheologische Verhalten von flüssigkeitsähnlich zu feststoffähnlich ändert. Dies beruht auf der Gleichheit der Relaxationszeiten von Enthalpierrelexation und Scherspannungsrelaxation für eine Vielzahl verschiedener Schmelzzusammensetzungen (Gottsmann et al., 2002). Der Verschiebungsfaktor, der Abkühlraten mit der Viskosität bei der Glasübergangstemperatur in Beziehung setzt, scheint eine geringe Abhängigkeit von der Schmelzzusammensetzung zu besitzen.

Schließlich wurde auch der Einfluß des Wassergehaltes auf die Viskosität wasserhaltiger silikatischer Schmelzen mittels einer modifizierten TVF Gleichung parametrisiert (Giordano et al., 2000). Es zeigte sich, dass die Viskosität wasserhaltiger basaltischer Schmelzen niedriger ist als die wasserhaltiger phonolitischer Schmelzen, wogegen wasserhaltige trachytische Schmelzen eine Viskosität zwischen wasserhaltigen Phonoliten und hochviskosen wasserhaltigen Rhyoliten besitzen. Diese Feststellungen decken sich mit den beobachtbaren Eruptionsmechanismen. Eruptionen basaltischer Vulkane sind überwiegend effusiv, diejenigen phonolitischer Vulkane sind gemischt effusiv-explosiv, trachytische Vulkane (z.B. Flegräische Felder) sind überwiegend explosiv, und rhyolitische Vulkane sind hochexplosiv.

Die Viskosität trockener trachytischer Schmelzen mit unterschiedlichen Zusammensetzungen variiert um bis zu zwei Größenordnungen, die Viskosität wasserhaltiger Schmelzen um weniger als eine Größenordnung. Diese Unterschiede werden deutlich größer, wenn man die geschätzten Temperaturen verschiedener Eruptionen der Flegräischen Felder berücksichtigt.

Im Falle niedrigviskoser wasserhaltiger Schmelzen mit Temperaturen ähnlich denen natürlicher Magmen ist die Ungenauigkeit der Berechnungen groß. Diese Ungenauigkeit kann jedoch nicht genau quantifiziert werden, da es keine Messungen unter diesen Bedingungen gibt.

## Abstract

The main objective of this study is to investigate and model the viscosity of multicomponent natural silicate melts and constrain the compositional effects which affect such a parameter. The results of this study, relevant to all petrological and volcanological processes which involve some transport mechanism, will be applied to volcanic setting.

An extensive experimental study was performed, which constituted the basis for the general modelling of Newtonian viscosity in terms of composition and temperature. Composition, viscosity and density of selected samples were investigated at different water contents. The experimental method involved measuring the viscosity of dry and hydrated melts under superliquidus and supercooled conditions. In the high temperature range (1050 – 1600 °C) viscosities from  $10^{-0.5}$  to  $10^5$  Pa·s were obtained using a concentric cylinder apparatus. Measurements of both dry and hydrated samples in the low temperature (616-860 °C) - high viscosity ( $10^{8.5}$  –  $10^{12}$  Pa·s) interval, from glassy samples quenched after high temperature viscometry, were performed using the dilatometric method of micropenetration. Hydrated samples measured in the supercooled state were synthesized, using a piston cylinder apparatus, between 1100° and 1600° C at 10 kbar. Water contents were measured using the Karl Fischer Titration (KFT) method. Fourier-Transform Infrared (FTIR) spectroscopy was used before and after the experiments in order to check that the water content was homogeneously distributed in the samples and that water had not been lost. Major element compositions of the dry remelted samples were determined using an electron microprobe.

Newtonian viscosities of silicate liquids were investigated in a range between  $10^{-1}$  to  $10^{11.6}$  Pa s and parameterised using the non-linear 3 parameter ( $A_{TVF}$ ,  $B_{TVF}$  and  $T_0$ ) TVF equation. The data provided in this work are combined also with previous data from Whittington et al. (2000, 2001); Dingwell et al. (1996); Neuville et al. (1993).

There are strong numerical correlations between parameters ( $A_{TVF}$ ,  $B_{TVF}$  and  $T_0$ ) that mask the effect of composition. Wide ranges of  $A_{TVF}$ ,  $B_{TVF}$  and  $T_0$  values can be used to describe individual datasets. This is true even when the data are numerous, well-measured and span a wide range of experimental conditions. In particular, “*strong*” liquids (liquids that are Arrhenian or slightly deviate from Arrhenian behaviour) place only minor restrictions on the absolute ranges of  $A_{TVF}$ ,  $B_{TVF}$  and  $T_0$ . Therefore, strategies for modelling the effects on compositions should be built around high-quality datasets collected on non-Arrhenian liquids.

The relationships between important quantities such as the fragility  $F$ , characterizing the deviation from Arrhenian rheological behaviour, are quantified in terms of the chemical, structure-related parameter NBO/T. Initial addition of network modifying elements to a fully polymerised liquid (i.e. NBO/T=0) results in a rapid increase in  $F$ . However, at NBO/T values above 0.4-0.5 further addition of a network modifier has little effect on fragility. This parameterisation indicates that this sharp change in the variation of fragility with NBO/T is due to a sudden change in the configurational properties and rheological regimes, owing to the addition of network modifying elements.

The resulting TVF parameterisation has been also used to build up a predictive model for Arrhenian to non-Arrhenian melt viscosity. The model accommodates the effect of composition via an empirical parameter called here the “structure modifier” (SM). SM is the summation of molar oxides of Ca, Mg, Mn, half of the total iron Fetot, Na and K. This approach is validated by the highly predictive capability of the viscosity model. The model reproduces all the original data set with about 10%, of the measured values of  $\log \eta$  over the entire range of composition in the temperature interval 700-1600 °C.

The combination of calorimetric and viscosimetric data has enabled a simple expression to be used to predict shear viscosity at the glass transition, that is the temperature which defines the transition from a liquid-like to a solid-like rheological behaviour. The basis for this stems from the equivalence of the relaxation times for both enthalpy and shear stress relaxation in a wide range of silicate melt compositions (Gottsmann et al., 2002). A shift factor that relates cooling rate data with viscosity at the glass transition appears to be slightly dependent on the melt composition.

Finally, the effect of water content on decreasing the viscosity of silicate melts has also been parameterised using a modified TVF expression (Giordano et al., 2000). This leads to an improvement in our knowledge of the non-Arrhenian behaviour of silicate melts over a wide compositional range from basaltic to rhyolitic and from trachytic to peralkaline phonolite compositions in the temperature interval pertaining to volcanic and subvolcanic processes. The viscosities of natural hydrous basaltic liquids are shown to be lower than those of hydrous phonolites, whereas thachytes show viscosity that are higher than those of phonolites and lower than those of rhyolites. This is consistent with the style of eruption associated with these compositions, with trachytes generating eruptions that are dominantly explosive (e.g.

Phlegrean Fields volcano), compared to the highly explosive style of rhyolitic volcanoes, the mixed explosive-effusive style of phonolitic volcanoes (e.g. Vesuvius) and the dominantly effusive style of basalts. Variations in composition between the trachytes translate into differences in liquid viscosity of nearly two orders of magnitude in dry conditions, and less than one order of magnitude in hydrous conditions. These differences increase significantly when the estimated eruptive temperatures of different eruptions at Phlegrean Fields are taken into account.

At temperatures close to those of natural magmas and in the case of low viscosity hydrous liquids the uncertainty of the calculations is large, although it cannot be quantified, due to a lack of measurements under these conditions.

*Ad Erika, Martina ed Elisa:” i vostri occhi e sorrisi  
hanno continuamente  
illuminato la mia strada”*

# Content

<b>Zusammenfassung</b> .....	<b>iv</b>
<b>Abstract</b> .....	<b>ix</b>
<b>1. Introduction</b> .....	<b>1</b>
<b>2. Theoretical and experimental background</b> .....	<b>2</b>
2.1. <i>Relaxation</i> .....	2
2.1.1. Liquids, supercooled liquids, glasses and the glass transition temperature.....	2
2.1.2. Overview of the main theoretical and empirical models describing the viscosity of melts.....	5
2.1.3. Departure from Arrhenian behaviour and fragility.....	9
2.1.4. The Maxwell mechanics of relaxation.....	12
2.1.5. Glass transition characterization applied to fragile fragmentation dynamics.....	14
2.2.1. Structure of silicate melts.....	16
2.2.2. Methods to investigate the structure of silicate liquids.....	17
2.2.3. Viscosity of silicate melts: relationships with structure.....	18
<b>3. Experimental Methods</b> .....	<b>21</b>
3.1. <i>General procedure</i> .....	21
3.2. <i>Experimental measurements</i> .....	21
3.2.1. Concentric cylinder.....	21
3.2.2. Piston cylinder.....	23
3.2.3. Micropenetration technique.....	24
3.2.4. Fourier-transform infrared (FTIR) spectroscopy.....	28
3.2.5. Density determination.....	29
3.2.6. Karl – Fischer – titration (KFT).....	30
3.2.7. Differential Scanning Calorimetry (DSC).....	32
<b>4. Sample selection</b> .....	<b>34</b>
<b>5. Dry silicate melts-Viscosity and Calorimetry</b> .....	<b>36</b>
5.1. <i>Results</i> .....	38
5.2. <i>Modelling the non-Arrhenian rheology of silicate melts: Numerical considerations</i> .....	40
5.2.1. Procedure strategy.....	40
5.2.2. Model-induced covariances.....	42
5.2.3. Analysis of covariance.....	42
5.2.4. Model TVF functions.....	45
5.2.5. Data-induced covariances.....	46
5.2.6. Variance in model parameters.....	48
5.2.7. Covariance in model parameters.....	50
5.2.8. Model TVF functions.....	51
5.2.9. Strong vs. fragile melts.....	52
5.2.10. Discussion.....	54
5.3. <i>Predicting the “kinetic” fragility of natural silicate melts: constraints using Tammann-Vogel–Fulcher equation</i> .....	56

5.3.1. Results.....	56
5.3.2. Discussion.....	60
<i>5.4. Towards a Non-Arrhenian multi-component model for the viscosity of magmatic melts.</i>	<i>62</i>
5.4.1. The viscosity of dry silicate melts – compositional aspects.....	62
5.4.2. Modelling the viscosity of dry silicate liquids - calculation procedure and results.....	66
5.4.3. Discussion.....	69
<i>5.5. Predicting shear viscosity across the glass transition during volcanic processes: a calorimetric calibration.....</i>	<i>71</i>
5.5.1. Sample selection and methods.....	73
5.5.2. Results and discussion.....	75
5.6. <i>Conclusions</i> .....	82
<b>6. Viscosity of hydrous silicate melts from Phlegrean Fields and Vesuvius: a comparison between rhyolitic, phonolitic and basaltic liquids.....</b>	<b>84</b>
6.1. <i>Sample selection and characterization</i> .....	85
6.2. <i>Data modelling</i> .....	86
6.3. <i>Results</i> .....	89
6.4. <i>Discussion</i> .....	96
6.5. <i>Conclusions</i> .....	100
<b>7. Conclusions.....</b>	<b>101</b>
<b>8. Outlook.....</b>	<b>104</b>
<b>9. Appendices.....</b>	<b>105</b>
<i>Appendix I: Computation of confidence limits.....</i>	<i>105</i>
<b>10. References.....</b>	<b>108</b>

# 1. Introduction

Understanding how the magma below an active volcano evolves with time and predicting possible future eruptive scenarios for volcanic systems, is crucial for the hazard assessment and risk mitigation in areas where active volcanoes are present. The viscous response of magmatic liquids to stresses applied to the magma body (for example in the magma conduit) controls the fluid dynamics of magma ascent. Adequate numerical simulation of such scenarios requires detailed knowledge of the viscosity of the magma. Magma viscosity is sensitive to the liquid composition, volatile, crystal and bubble contents.

High temperature, high pressure viscosity measurements in magmatic liquids involve complex scientific and methodological problems. Despite more than 50 years of research geochemists and petrologists have been unable to develop a unified theory to describe the viscosity of complex natural systems.

Current models for describing the viscosity of magmas are still poor and limited to a very restricted compositional range. For example the models of Whittington et al. (2000, 2001) and Dingwell et al. (1998 a, b) are only applicable to alkaline and peralkaline silicate melts. The model accounting for the important non-Arrhenian variation of viscosity of calcalkaline magmas (Hess and Dingwell, 1996) is proven to greatly fail for alkaline magmas (Giordano et al., 2000). Furthermore, under/over-estimations of the viscosity due to the application of the still widely used Shaw empirical model (1972) have been, for instance, observed for basaltic melts, trachytic and phonolitic products (Giordano and Dingwell, 2002; Romano et al., 2002; Giordano et al., 2002) and many other silicate liquids (e.g. Richet, 1984; Persikov, 1991; Richet and Bottinga, 1995; Baker, 1996; Hess and Dingwell, 1996; Toplis et al., 1997).

In this study, a detailed investigation of the rheological properties of silicate melts was performed. This allowed the viscosity-temperature-composition relationships relevant to petrological and volcanological processes to be modelled. The results were then applied to volcanic settings.

## 2. Theoretical and experimental background

### 2.1. Relaxation

#### 2.1.1. Liquids, supercooled liquids, glasses and the glass transition temperature

Liquid behaviour is the equilibrium response of a melt to an applied perturbation, resulting in the determination of an equilibrium liquid property (Dingwell and Webb, 1990). If a silicate liquid is cooled slowly (following an equilibrium path) when it reaches its melting temperature  $T_m$  it starts to crystallise and shows discontinuities in first (enthalpy, volume, entropy) and second order (heat capacity, thermal expansion coefficient) thermodynamics properties (Fig. 2.1 and 2.2). If cooled rapidly the liquid may avoid crystallisation, even well below the melting temperature  $T_m$ . Instead it forms a supercooled liquid (Fig. 2.2). The supercooled liquid is a metastable thermodynamic equilibrium configuration which (as it is the case for the equilibrium liquid) requires a certain time, termed the *structural relaxation time*, to provide an equilibrium response to the applied perturbation.

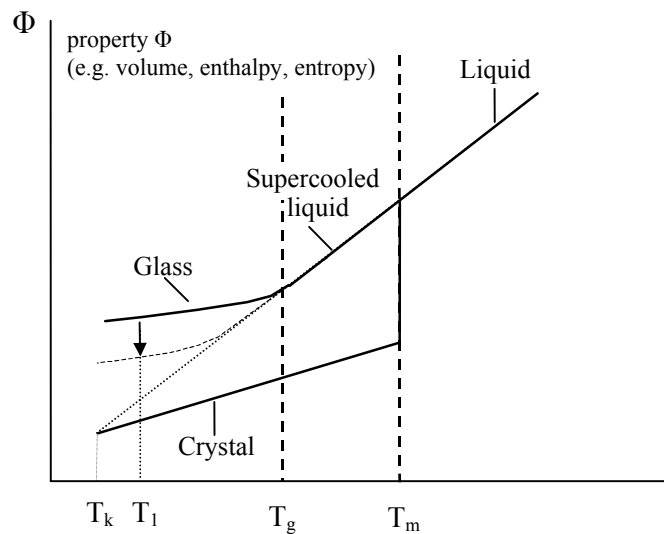


Fig. 2.1.: Schematic diagram showing the path of first order properties with temperature. Cooling a liquid “rapidly” below the melting temperature  $T_m$  may result in the formation of a supercooled (metastable) or even disequilibrium glass conditions. In the picture is also shown the first order phase transition corresponding to the passage from a liquid to crystalline phase. The transition from metastable liquid to glassy state is marked by the glass transition that can be characterized by a glass transition temperature  $T_g$ . The vertical arrow in the picture shows the first order property variation accompanying the structural relaxation if the glass temperature is held at  $T_1$ .  $T_k$  is the Kauzmann temperature (see section 2.1.3.).

It is possible that the system can reach viscosity values which are so high that its relaxation time becomes longer than the timescale required to measure the equilibrium thermodynamic properties. When the *relaxation time* of the supercooled liquid is orders of magnitude longer than the timescale at which perturbation occurs (days to years), the configuration of the system is termed the “glassy state”. The temperature interval that separates the liquid (relaxed) from the glassy state (unrelaxed, solid-like) is known as the “*glass transition interval*” (Fig. 2.2). Across the glass transition interval a sudden variation in second order thermodynamic properties (e.g. heat capacity  $C_p$ , molar expansivity  $\alpha=dV/dt$ ) is observed without discontinuities in first order thermodynamic properties (e.g. enthalpy  $H$ , volume  $V$ ) (Fig. 2.2).

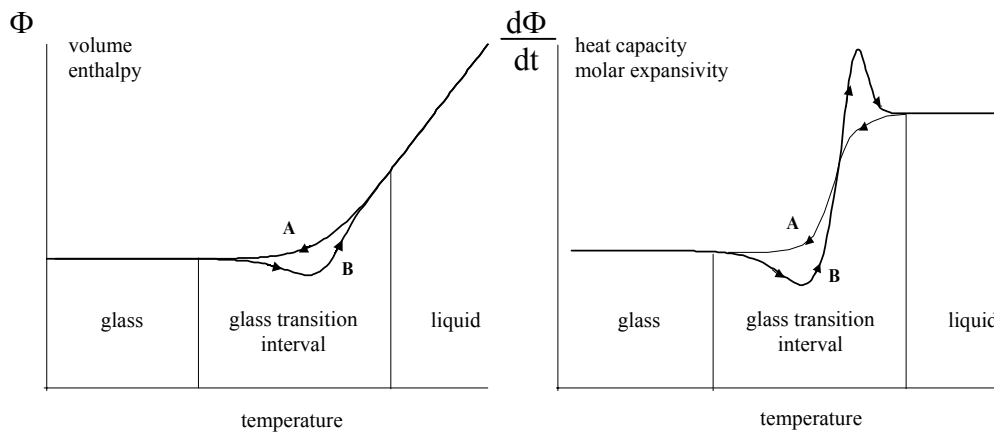


Fig. 2.2.: Paths of the (a) first order (e.g. enthalpy, volume) and (b) second order thermodynamic properties (e.g. specific heat, molar expansivity), followed from a supercooled liquid or a glass during cooling A and heating B.

The glass transition temperature interval depends on various parameters such as the cooling history and the timescales of the observation. The time dependence of the structural relaxation is shown in Fig. 2.3 (Dingwell and Webb, 1992). Since the freezing in of configurational states is a kinetic phenomenon, the glass transition takes place at higher temperatures with faster cooling rates (Fig. 2.4). Thus  $T_g$  is not an unequivocally defined temperature but a *fictive* state (Fig. 2.4). That is to say a *fictive* temperature is the temperature for which the configuration of the glass corresponds to the equilibrium configuration in the liquid state.

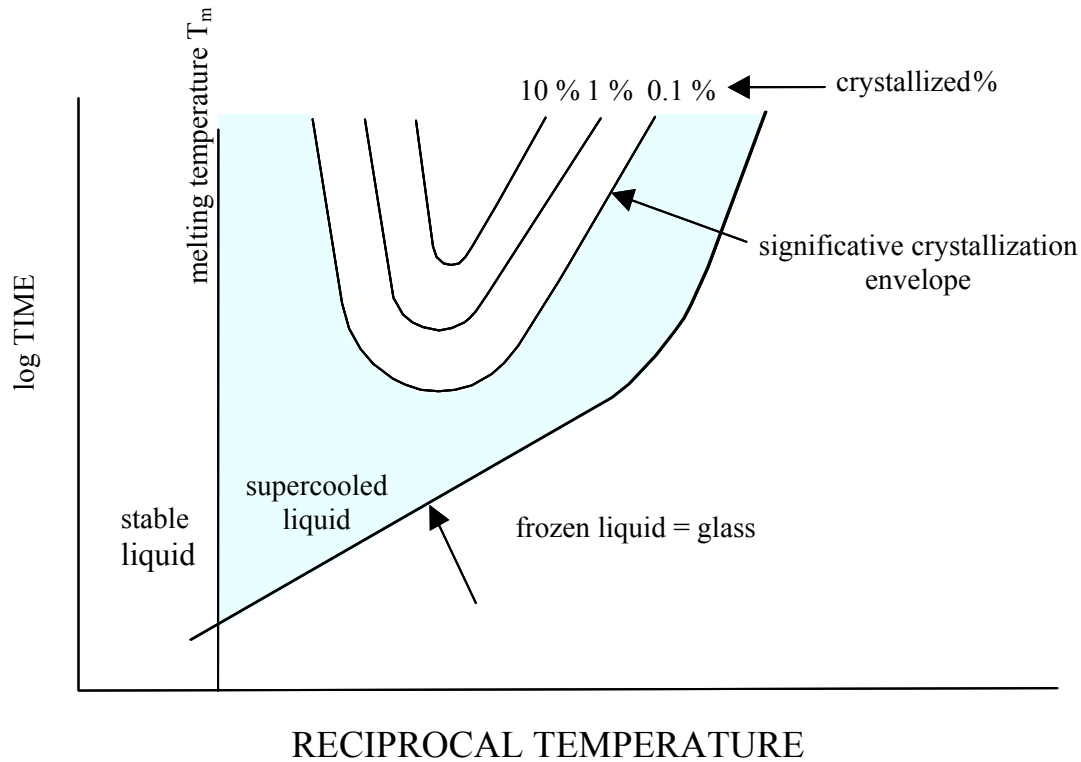


Fig. 2.3.: The fields of stability of stable and supercooled “*relaxed*” liquids and frozen glassy “*unrelaxed*” state with respect to the glass transition and the region where crystallisation kinetics become significant [time–temperature–transition (TTT) envelopes] are represented as a function of relaxation time and inverse temperature. A supercooled liquid is the equilibrium configuration of a liquid under  $T_m$  and a glass is the frozen configuration under  $T_g$ . The supercooled liquid region may span, depending on the chemical composition of silicate melts, a temperature range of several hundreds of Kelvin.

As the glass transition is defined as an interval rather than a single value of temperature, it becomes a further useful step to identify a common feature to define, by convention, the glass transition temperature. For industrial applications the glass transition temperature has been assigned to the temperature at which the viscosity of the system is  $10^{12}$  Pa·s (Scholze and Kreidl, 1986). This viscosity has been chosen because at this value the relaxation times for macroscopic properties are about 15 mins (at usual laboratory cooling rates), which is similar to the time required to measure these properties (Litovitz; 1960). In scanning calorimetry, the temperature corresponding to the extrapolated onset (Scherer, 1984) or the peak (Stevenson et al., 1995; Gottsmann et al., 2002) of the heat capacity curves (Fig. 2.2 b) is used.

A theoretic limit of the glass transition temperature is provided by the Kauzmann temperature  $T_k$ . The  $T_k$  is identified in Fig. 2.1 as the intersection between the entropy of the supercooled liquid and the entropy of the crystal phase. At temperature  $T < T_k$  the configurational entropy  $S_{conf}$ , given by the difference of the entropy of the liquid and the crystal would become paradoxally negative.

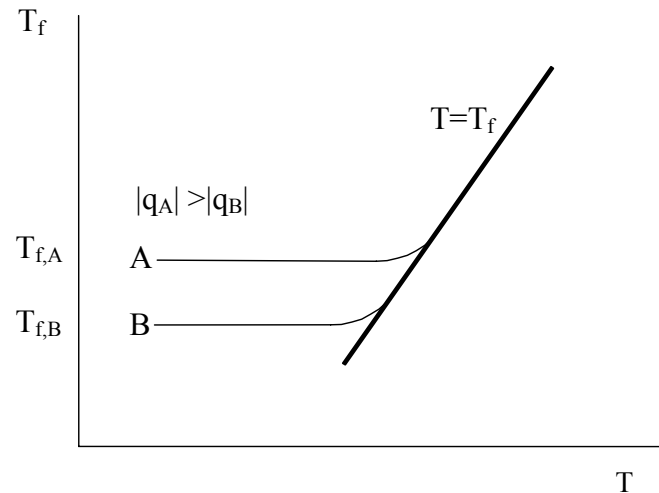


Fig. 2.4.: Glass transition temperatures  $T_{f,A}$  and  $T_{f,B}$  at different cooling rate  $q_A$  and  $q_B$  ( $|q_A| > |q_B|$ ). This shows how the glass transition temperature is a kinetic boundary rather than a fixed temperature. The deviation from equilibrium conditions ( $T = T_f$  in the figure) is dependent on the applied cooling rate. The structural arrangement frozen into the glass phase can be expressed as a limiting fictive temperature  $T_{f,A}$  and  $T_{f,B}$ .

### 2.1.2. Overview of the main theoretical and empirical models describing the viscosity of melts

Today it is widely recognized that melt viscosity and structure are intimately related. It follows that the most promising approaches to quantify the viscosity of silicate melts are those which attempt to relate this property to melt structure [mode-coupling theory (Goetze, 1991), free volume theory (Cohen and Grest, 1979) and configurational entropy theory (Adam and Gibbs, 1965)]. Of these three approaches the Adam-Gibbs theory has been shown to work remarkably well for a wide range of silicate melts (Richet, 1984; Hummel and Arndt, 1985; Tauber and Arndt, 1987; Bottinga et al., 1995). This is because it quantitatively accounts for non-Arrhenian behaviour, which is now recognized to be a characteristic of almost all silicate melts. Nevertheless, many details relating structure and configurational entropy remain unknown.

In this section the Adam-Gibbs theory is presented together with a short summary of old and new theories that frequently have a phenomenological origin. Under appropriate conditions these other theories describe viscosity's dependence on temperature and composition satisfactorily. As a result they constitute a valid practical alternative to the Adam and Gibbs theory.

➤ *Arrhenius law*

The most widely known equation, which describes the viscosity dependence of liquids on temperature, is the Arrhenius law:

$$\log \eta = A_{Arr} + \frac{B_{Arr}}{T} \quad (2.1)$$

where  $A_{Arr}$  is the logarithm of viscosity at infinite temperature,  $B_{Arr}$  is the ratio between the activation energy  $E_a$  and the gas constant  $R$ ;  $T$  is the absolute temperature.

This expression is an approximation of a more complex equation derived from the Eyring *absolute rate theory* (Eyring, 1936; Glastone et al., 1941). The basis of the *absolute rate theory* is the mechanism of single atoms slipping over the potential energy barriers  $E_a = R \cdot B_{Arr}$ . This is better known as the activation energy (Kj/mole) and it is a function of the composition but not of temperature.

Using the Arrhenius law, Shaw (1972) derived a simple empirical model for describing the viscosity of a Newtonian fluid as the sum of the contributions  $\eta_i$  due to the single oxides constituting a silicate melt:

$$\ln \eta(T) = \sum_i x_i \ln \eta_i = \sum_i x_i \left( A_i + \frac{B_i}{T} \right) \quad (2.2)$$

where  $x_i$  indicates the molar fraction of oxide component  $i$ , while  $A_i$  and  $B_i$  are experimental constants of component  $i$ .

Subsequent studies (e.g. Richet, 1984; Persikov, 1991; Richet and Bottinga, 1995; Baker, 1996; Hess and Dingwell, 1996; Toplis et al., 1997) have shown that the Arrhenius relation (Eq. 2.3), and the expressions derived from it (Shaw, 1972; Bottinga and Weill, 1972), are largely insufficient to describe the viscosity of melts over the entire temperature interval that are now accessible using new techniques. In many recent studies this model is demonstrated to fail, especially for the silica poor melts (e.g. Neuville et al., 1993).

➤ *Configurational entropy theory*

Adam and Gibbs (1965) generalised and extended the previous work of Gibbs and Di Marzio (1958) who used the Configurational Entropy theory to explain the relaxation properties of the supercooled glass-forming liquids. Adam and Gibbs (1965) suggested that viscous flow in the liquids occurs through the cooperative rearrangements of groups of

molecules in the liquids, with average probability  $w(T)$  to occur, which is inversely proportional to the structural relaxation time  $\tau$ , and which is given by the following relation:

$$w(T) = \bar{A} \exp\left(-\frac{B_e}{T \cdot S_{conf}}\right) = \tau^{-1} \quad (2.3)$$

where  $\bar{A}$  (“frequency” or “pre-exponential” factor) and  $B_e$  are dependent on composition and have a negligible temperature dependence with respect to the product  $T \cdot S_{conf}$ , and:

$$S_{conf}(T) = K_B \ln \Omega = \text{configurational entropy} \quad (2.4)$$

where  $K_B$  is the Boltzmann constant and  $\Omega$  represents the number of all the configurations of the system.

According to this theory the structural relaxation time is determined from the probability of microscopic volumes to undergo configurational variations. This theory was used as the basis for new formulations (Richet, 1984; Richet et al., 1986) employed in the study of the viscosity of silicate melts.

➤ Richet and his collaborators (Richet, 1984; Richet et al., 1986) demonstrated that the relaxation theory of Adam and Gibbs could be applied to the case of the viscosity of silicate melts through the expression:

$$\ln \eta = A_e + \frac{B_e}{T \cdot S_{conf}} \quad (2.5)$$

where  $A_e$  is a pre-exponential term,  $B_e$  is related to the barrier of potential energy obstructing the structural rearrangement of the liquid, and  $S_{conf}$  represents a measure of the dynamical states allowed to rearrange to new configurations.

$$S_{conf}(T) = S_{conf}(T_g) + \int_{T_g}^T \frac{C_{pConf}(T) dT}{T} \quad (2.6)$$

where

$$C_{pConf}(T) = C_{pl}(T) - C_{pg}(T_g) \quad (2.7)$$

is the configurational heat capacity;  $C_{p_l}(T)$  is the heat capacity of the liquid at temperature  $T$  and  $C_{p_g}(T_g)$  is the heat capacity of the liquid at the glass transition temperature  $T_g$ .

Here the value of  $C_{p_g}(T_g)$  constitutes the vibrational contribution to the heat capacity very close to the Dulong and Petit value of 24.942 J/K·mol (Richet, 1984; Richet et al., 1986).

The term  $C_{p_l}(T)$  is a not well-constrained function of temperature and composition and it is affected by excess contributions due to the non-ideal mixing of many of the oxide components.

A convenient expression for the heat capacity is:

$$C_{p_l}(T) = \sum_i x_i \cdot C_{p_i} + C_p^{excess} \quad (2.8)$$

where  $x_i$  is the molar fraction of the oxide component  $i$  and  $C_p^{excess}$  is the contribution to the non-ideal mixing, possibly a complex function of temperature and composition (Richet, 1984; Stebbins et al., 1984; Richet and Bottinga, 1985; Lange and Navrotsky, 1992, 1993; Richet et al., 1993; Liska et al., 1996).

➤ *Tammann Vogel Fulcher law.*

Another adequate description of the temperature dependence of viscosity is given by the empirical three parameter Tammann Vogel Fulcher (TVF) equation (Vogel, 1921; Tammann and Hesse, 1926; Fulcher, 1925):

$$\log \eta = A_{TVF} + \frac{B_{TVF}}{(T - T_0)} \quad (2.9)$$

where  $A_{TVF}$ ,  $B_{TVF}$  and  $T_0$  are constants that describe the pre-exponential term, the pseudo-activation energy and the TVF-temperature, respectively.

According to a formulation proposed by Angell (1985), Eq. 2.9, can be rewritten as follows:

$$\eta(T) = \eta_0 \exp \left[ \frac{DT_0}{T - T_0} \right] \quad (2.10)$$

where  $\eta_0$  is the pre-exponential term,  $D$ , the inverse of the *fragility*  $F$ , is the “fragility index” and  $T_0$  is the TVF temperature, that is the temperature at which viscosity diverges. In the following session a more detailed characterization of the fragility is presented.

### 2.1.3. Departure from Arrhenian behaviour and fragility

The almost universal departure from the familiar Arrhenius law (the same as Eq. 2. with  $T_0=0$ ) is probably the most important characteristic of glass-forming liquids. Angell (1985) used the  $D$  parameter, the “*fragility index*” (Eq. 2.10) to distinguish two extreme behaviours of liquids that easily form glass (glass-forming); the *strong* and the *fragile*.

High  $D$  values correspond to “*strong*” liquids and their behaviour approaches the Arrhenian case (the straight line in a  $\log \eta$  vs.  $T_g/T$  diagram, Fig. 2.5). Liquids which strongly

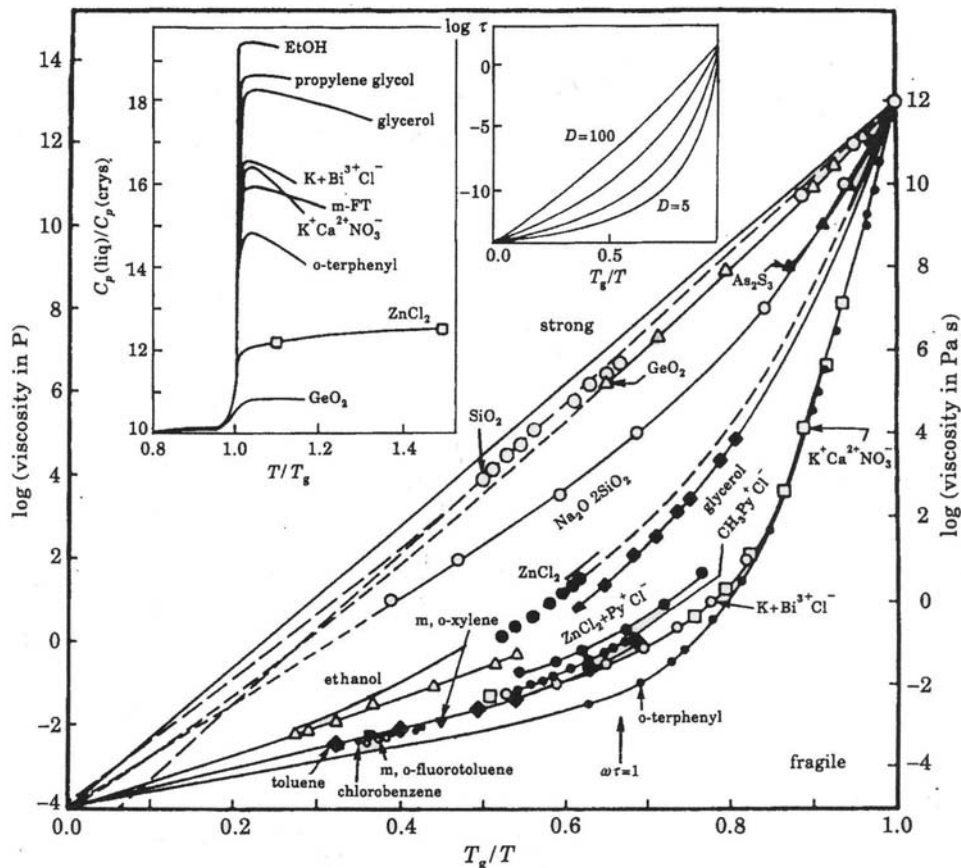


Fig. 2.5.: Arrhenius plots of the viscosity data of many organic compounds scaled by  $T_g$  values showing the “strong/fragile” pattern of liquid behaviour used to classify dry liquids.  $\text{SiO}_2$  is included for comparison. As shown in the insert, the jump in  $C_p$  at  $T_g$  is generally large for fragile liquids and small for strong liquids, although there are a number of exceptions, particularly when hydrogen bonding is present. High values of the fragility index  $D$  correspond to strong liquids (Angell, 1985). Here  $T_g$  is the temperature at which viscosity is  $10^{12}$  Pa·s (see 2.1.1.).

deviate from linearity are called “*fragile*” and show lower  $D$  values. A power law similar to that of the Tammann – Vogel – Fulcher (Eq. 2.9) provides a better description of their rheological behaviour. Compared with many organic polymers and molecular liquids, silicate melts are generally strong liquids, although important departures from Arrhenian behaviour can still occur.

The strong/fragile classification has been used to indicate the sensitivity of the liquid structure to temperature changes. In particular, while “fragile” liquids easily assume a large variety of configurational states when undergoing a thermal perturbation, “strong” liquids show a firm resistance to structural change, even if large temperature variations are applied. From a calorimetric point of view such behaviours correspond to very small jumps in the specific heat ( $\Delta C_p$ ) at  $T_g$  for strong liquids, whereas fragile liquids show large jumps of such quantity.

The ratio  $\frac{T_0}{T_g}$  (kinetic fragility) [where the glass transition temperature  $T_g$  is well constrained as the temperature at which viscosity is  $10^{12}$  Pa·s (Richet and Bottinga, 1995)] may characterize the deviations from Arrhenius law (Martinez & Angell, 2001; Ito et al., 1999; Rössler et al., 1998; Angell, 1997; Stillinger, 1995; Hess et al., 1995). The kinetic fragility is usually the same as  $\frac{T_K}{T_g}$  (thermodynamic fragility) where  $T_K^1$  is the Kauzmann temperature (Kauzmann, 1948). In fact from Eq. 2.10, it follows that:

$$\frac{T_g}{T_0} = 1 + \frac{D}{\left[ 2.303 \cdot \log \left( \frac{\eta_{T_g}}{\eta_{T_\infty}} \right) \right]} \quad (2.11)$$

---

<sup>1</sup> The Kauzmann temperature  $T_K$  is the temperature which, in the Adam-Gibbs theory (Eq. 2.5), corresponds to  $S_{\text{conf}} = 0$ . It represents the relaxation time and viscosity divergence temperature of Eq. 2.3. By analogy it is the same as the  $T_0$  temperature of the Tammann – Vogel – Fulcher equation (Eq. 2.9). According to Eq. 2.4  $T_K$  (and consequently  $T_0$ ) also corresponds to a dynamical state corresponding to unique configuration ( $\Omega = 1$  in Eq. 2.4) of the considered system, that is the whole system itself. From such an observation it seems to derive that the TVF temperature  $T_0$  is, beside an empirical fit parameter necessary to describe the viscosity of silicate melts, an overall feature of those systems that can be described using a TVF law.

A physical interpretation of this quantity is still not provided in literature. Nevertheless, some correlation between its value and variation with structural parameters is discussed in session 5.3.

where  $\frac{\eta_{T_g}}{\eta_{T_\infty}}$  is the ratio between the viscosity at  $T_g$  and that at infinite temperature  $T_\infty$ .

Angell (1995) and Miller (1978) observed that for polymers the ratio  $\log \left( \frac{\eta_{T_g}}{\eta_{T_\infty}} \right)$  is  $\sim 17$ .

Many other expressions have been proposed in order to define the departure of viscosity from Arrhenian temperature dependence and distinguish the fragile and strong glass formers. For example, a model independent quantity, the steepness parameter  $m$ , which constitutes the slope of the viscosity trace at  $T_g$  has been defined by Plazek and Ngai (1991) and Böhmer and Angell (1992), explicitly:

$$m = \left. \frac{d(\log_{10} \eta)}{d(T_g/T)} \right|_{T=T_g}$$

Therefore “steepness parameter” may be calculated by differentiating the TVF equation (2.9):

$$\text{steepness parameter} = m = \left. \frac{d(\log_{10} \eta)}{d(T_g/T)} \right|_{T=T_g} = \frac{B_{TVF}}{T_g(1 - T_0/T_g)^2} \quad (2.12)$$

where  $T_g$  is the temperature at which viscosity is  $10^{12}$  Pa·s (glass transition temperatures determined using calorimetry on samples with cooling rates on the order of  $10$  °C/s occur very close to this viscosity) (Richet and Bottinga, 1995).

Note that the parameter  $D$  or  $T_g/T_0$  may quantify the degree of non-Arrhenian behaviour of  $\eta(T)$  whereas the steepness parameter  $m$  is a measure of the steepness of the  $\eta(T_g/T)$  curve at  $T_g$ , only. It must be taken into account that  $D$  (or  $T_g/T_0$ ) and  $m$  are not necessarily related (Rössler et al., 1998).

Regardless of how the deviation from an Arrhenian behaviour is being defined, the data of Stein and Spera (1993) and others indicate that it increases from  $\text{SiO}_2$  to nephelinite. This is confirmed by molecular dynamic simulations of the melts (Scamehorn and Angell, 1991; Stein and Spera, 1995).

Many other experimental and theoretical hypotheses have been developed from the theories outlined above. The large amount of work and numerous parameters proposed to

describe the rheological properties of organic and inorganic material reflect the fact that the glass transition is still a poorly understood phenomenon and is still subject to much debate.

#### 2.1.4. The Maxwell mechanics of relaxation

When subject to a disturbance of its equilibrium conditions the structure of a silicate melt, or other material, requires a certain time (*structural relaxation time*) to be able to achieve a new equilibrium state. In order to choose the appropriate timescale to perform experiments at conditions as close as possible to equilibrium conditions (therefore not subjected to time-dependent variables) the viscoelastic behaviour of melts must be understood. Depending upon the stress conditions that a melt is subjected to, it will behave in a viscous or elastic manner. Investigation of viscoelasticity allows the natural relaxation process to be understood This is the starting point for all the processes concerning the rheology of silicate melts.

This discussion, based on the Maxwell considerations, will be limited to how the structure of a nonspecific physical system (hence also a silicate melt) equilibrates when subjected to mechanical stress, here generically indicated as  $\sigma$ .

Silicate melts show two different mechanical responses to a step function of the applied stress:

- *Elastic* – the strain response to an applied stress is time independent and reversible
- *Viscous* – the strain response to an applied stress is time dependent and non-reversible.

To easily comprehend the different mechanical responses of a physical system to an applied stress it is convenient to refer to simplified spring or spring and dash-pot schemes.

The *Elastic* deformation is time-independent as the strain reaches its equilibrium level instantaneously upon application or removal of the stress, and the response is reversible because when the stress is removed the strain returns to zero. The slope of the stress-strain ( $\sigma$ - $\varepsilon$ ) curve gives the *elastic* constant for the material. This is called the elastic modulus  $E$ :

$$\frac{\sigma}{\varepsilon} = E \quad (2.13)$$

The strain response due to a *non-elastic* deformation is time-dependent, as it takes a finite time for the strain to reach equilibrium, and non-reversible as it implies that even after the stress is released deformation persists, energy from the perturbation is dissipated. This is a

viscous deformation. An example of such a system could be represented by a viscous dash-pot.

The following expression describes the non-elastic relation between the applied stress  $\sigma(t)$  and the deformation  $\varepsilon$  for Newtonian fluids:

$$\sigma(t) = \eta \frac{d\varepsilon}{dt} \quad (2.14)$$

where  $\eta$  is the Newtonian viscosity of the material. The Newtonian viscosity describes the resistance of a material to flow.

The intermediate region between the elastic and the viscous behaviour is called viscoelastic region and the description of the time-shear deformation curve is defined by a

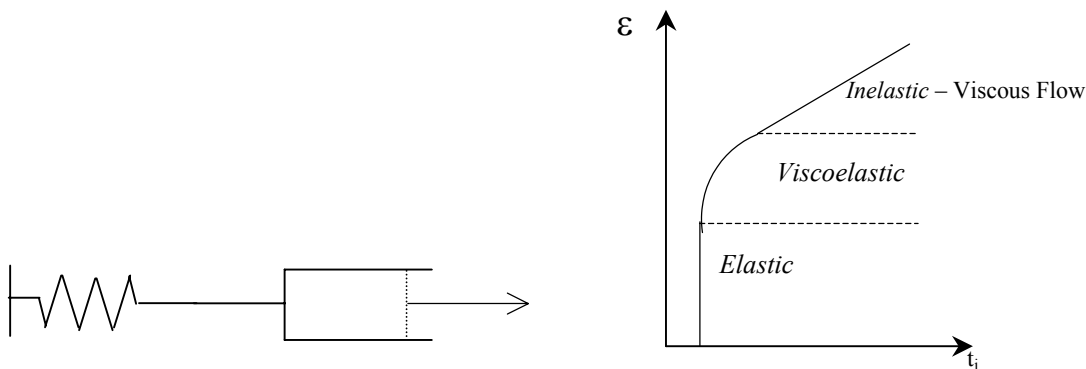


Fig. 2.6.: Schematic representation of the strain ( $\varepsilon$ ) – stress ( $\sigma$ ) – time ( $t_i$ ) relationships for a system undergoing at different times different kind of deformation. Such schematic system can be represented by a Maxwell spring-dash-pot element. Depending on the timescale of the applied stress a system deforms according to different paths.

combination of the equations 2.12 and 2.13 (Fig. 2.6). Solving the equation in the viscous region gives us a convenient approximation of the timescale of deformation over which transition from a purely elastic –“*relaxed*” to a purely viscous – “*unrelaxed*” behaviour occurs, which constitute the structural relaxation time:

$$\tau = \frac{\eta}{E} \quad (2.15)$$

The structure of a silicate melt can be compared with a complex combination of spring and dashpot elements, each one corresponding to a particular deformational mechanism and contributing to the timescale of the system. Every additional phase may constitute a

*relaxation mode* that influences the global structural relaxation time; each *relaxation mode* is derived, for example, from the chemical or textural contribution.

### 2.1.5. Glass transition characterization applied to fragile fragmentation dynamics

Recently, it has been recognised that the transition between liquid-like to a solid-like mechanical response, corresponding to the crossing of the glass transition, can play an important role in volcanic eruptions (e.g. Dingwell and Webb, 1990; Sato et al., 1992; Dingwell, 1996, Papale, 1999). Intersection of this kinetic boundary during an eruptive event may have catastrophic consequences, because the mechanical response of the magma or lava to an applied stress at this brittle/ductile transition governs the eruptive behaviour (e.g. Sato et

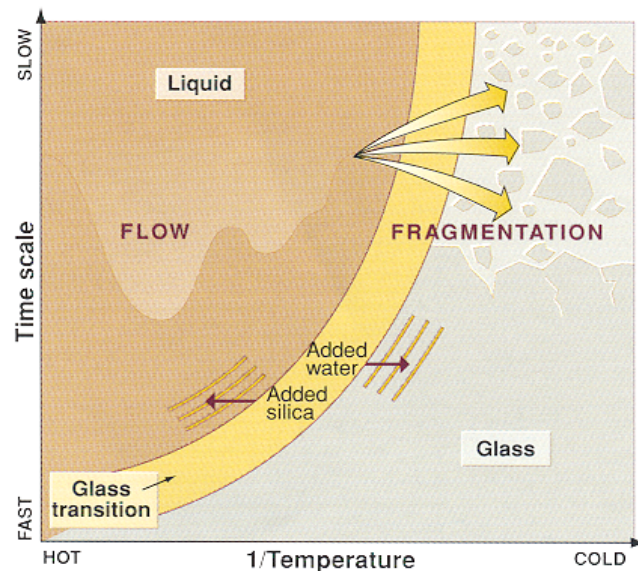


Fig. 2.7. The glass transition in time-reciprocal temperature space. Deformations over a period of time longer than the structural relaxation time generate a relaxed, viscous liquid response. When the time-scale of deformation approaches that of the glass transition  $t$ , the result is elastic storage of strain energy for low strains and shear thinning and brittle failure for high strains. The glass transition may be crossed many times during the formation of volcanic glasses. The first crossing may be the primary fragmentation event in explosive volcanism. Variations in water and silica contents can drastically shift the temperature at which the transition in mechanical behaviour is experienced. Thus, magmatic differentiation and degassing are important processes influencing the melt's mechanical behaviour during volcanic eruptions. (From Dingwell – Science, 1996).

al., 1992). As reported in section 2.2, whether an applied stress is accommodated by viscous deformation or by an elastic response is dependent on the timescale of the perturbation with respect to the timescale of the structural response of the geomaterial, i.e. its structural relaxation time (e.g. Moynihan, 1995; Dingwell, 1995). Since a viscous response may

accommodate orders of magnitude higher strain-rates than a brittle response, sustained stress applied to magmas at the glass transition will lead to Non-Newtonian behaviour (Dingwell, 1996), which will eventually terminate in the brittle failure of the material. The viscosity of the geomaterial at low crystal and/or bubble content is controlled by the viscosity of the liquid phase (§ 2.2). Knowledge of the melt viscosity enables calculation of the relaxation time  $\tau$  of the system via the Maxwell (1867) relationship (e.g. Dingwell and Webb, 1990):

$$\tau = \frac{\eta_N}{G_\infty} \quad (2.16)$$

where  $G_\infty$  is the shear modulus with a value of  $\log_{10} (\text{Pa}) = 10 \pm 0.5$  (Webb and Dingwell, 1990) and  $\eta_N$  is the Newtonian shear viscosity. Due to the thermally activated nature of structural relaxation, Newtonian viscosities at the glass transition vary with cooling history. For cooling rates on the order of several K/min, viscosities of approximately  $10^{12}$  Pa s (Scholze and Kreidl, 1986) give relaxation times on the order of 100 seconds.

Cooling rate data for volcanic glasses across the glass transition have revealed variations of up to seven orders of magnitude from tens of Kelvins per second to less than one Kelvin per day (Wilding et al., 1995, 1996, 2000). A logical consequence of this wide range of cooling rates is that viscosities at the glass transition will vary substantially. Rapid cooling of a melt will lead to higher glass transition temperatures at lower melt viscosities, whereas slow cooling will have the opposite effect, generating lower glass transition temperatures at correspondingly higher melt viscosities. Indeed, such a quantitative link between viscosities at the glass transition and cooling rate data for obsidian rhyolites based on the equivalence of their enthalpy and shear stress relaxation times has been provided by Stevenson et al. (1995). A similar relationship for synthetic melts had been proposed earlier by Scherer (1984).

## 2.2. Structure and viscosity of silicate liquids

### 2.2.1. Structure of silicate melts

$\text{SiO}_4^{4-}$  tetrahedra are the principal building blocks of silicate crystals and melts. The oxygen connecting two of these tetrahedral units is called a “bridging oxygen” (BO)(Fig. 2.7). The “degree of polymerisation” in these material is proportional to the number of BO per cations that have the potential to be in tetrahedral coordination  $T$  (generally in silicate melts:  $\text{Si}^{4+}$ ,  $\text{Al}^{3+}$ ;  $\text{Fe}^{3+}$ ;  $\text{Ti}^{4+}$  and  $\text{P}^{5+}$ ). The “ $T$ ” cations are therefore called, the “network former cations”. More commonly used is the term non-bridging oxygen per tetrahedrally coordinated

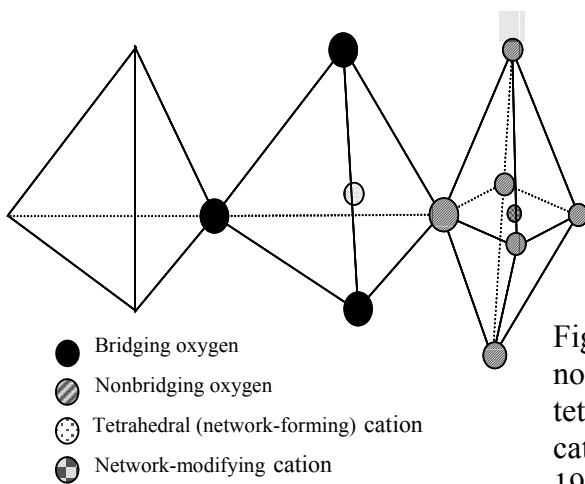


Fig. 2.7.: Sketch of nonbridging oxygen per tetrahedrally coordinated cations ( $NBO/T$ ) (Mysen, 1988).

cation,  $NBO/T$ . A non-bridging oxygen (NBO) is an oxygen that bridges from a tetrahedron to a non-tetrahedral polyhedron (Fig. 2.7). Consequently the cations constituting the non-tetrahedral polyhedron are the “network-modifying cations”.

Addition of other oxides to silica (considered as the base-composition for all silicate melts) results in the formation of non-bridging oxygens.

Most properties of silicate melts relevant to magmatic processes depend on the proportions of non-bridging oxygens. These include, for example, transport properties (e.g. Urbain et al., 1982; Richet, 1984), thermodynamic properties (e.g. Navrotsky et al., 1980, 1985; Stebbins et al., 1983), liquid phase equilibria (e.g. Ryerson and Hess, 1980; Kushiro, 1975) and others. In order to understand how the melt structure governs these properties, it is necessary, first, to describe the structure itself and then, relate this structural information to the properties of the materials. To the following analysis is probably worth noting that despite the fact that most of the common extrusive rocks have  $NBO/T$  values between 0 and 1, the variety of eruptive types is surprisingly wide.

In view of the observation that nearly all naturally occurring silicate liquids contain cations (mainly metal cations, but also Fe, Mn and others) that are required for electrical charge-balance of tetrahedrally-coordinated cations ( $T$ ), it is necessary to characterize the relationships between melt structure and the proportion and type of such cations.

Mysen et al. (1985) suggested that, as the “network modifying cations”, occupy the central positions of non-tetrahedral polyhedra, and are responsible for the formation of NBO, the expression  $NBO/T$  can be rewritten as:

$$\frac{NBO}{T} = \frac{1}{T} \sum_{i=1}^i nM_i^{n+} \quad (2.17)$$

where  $M_i^{n+}$  is the proportion of network modifying cations,  $i$ , with electrical charge  $n+$ . Their sum is obtained after subtraction of the proportion of metal cations necessary for charge-balancing of  $Al^{3+}$  and  $Fe^{3+}$ , whereas  $T$  is the proportion of the cations in tetrahedral coordination. The use of Eq. 2.17 is controversial and non-univocal because it is not easy to define “*a priori*” the cation coordination. The coordination of cations is in fact dependent on composition (Mysen, 1988). Eq. 2.17 constitutes however the best approximation to calculate the degree of polymerisation of silicate melt structures.

### 2.2.2. Methods to investigate the structure of silicate liquids.

As the tetrahedra themselves can be treated as a near rigid units, properties and structural changes in silicate melts are essentially driven by changes in the T – O – T angle and the properties of the non – tetrahedral polyhedra. Therefore how the properties of silicate materials vary with respect to these parameters is central in understanding their structure. For example, the T – O – T angle is, a systematic function of the degree to which the melt network is polymerized. The angle decreases as  $NBO/T$  decreases and the structure becomes more compact and denser.

The main techniques used to analyse the structure of silicate melts are the spectroscopic techniques (e.g.: IR, RAMAN, NMR, Mössbauer, ELNES, XAS). In addition experimental studies of the properties which are more sensitive to the configurational states of a system can provide indirect information on the silicate melt structure. These properties include reaction enthalpy, volume and thermal expansivity (e.g. Mysen, 1988) as well as viscosity. Viscosity of superliquidus and supercooled liquids will be investigated in this work.

### 2.2.3. Viscosity of silicate melts: relationships with structure.

In Earth Sciences it is well known that magma viscosity is principally function of liquid viscosity, temperature, crystal and bubble content.

While the effect of crystals and bubbles can be accounted for using complex macroscopic fluid dynamic descriptions, the viscosity of a liquid is a function of composition, temperature and pressure that still require extensive investigation. Neglecting, at the moment, the influence of pressure as it has very minor effect on the melt viscosity up to about 20 kbar (e.g. Dingwell et al., 1993; Scarfe et al., 1987), it is known that viscosity is sensitive to the structural configuration, that is the distribution of atoms, in the melt (see § 2.1.3. for details). Therefore the relationship between “network modifying” cations and “network forming/stabilizing” cations with viscosity is critical to the understanding the structure of a magmatic liquid and *vice versa*.

The main forming/stabilizing cations and molecules are:  $\text{Si}^{4+}$ ,  $\text{Al}^{3+}$ ,  $\text{Fe}^{3+}$ ,  $\text{Ti}^{4+}$ ,  $\text{P}^{5+}$  and  $\text{CO}_2$  (e.g. Mysen, 1988). The main network modifying cations and molecules are:  $\text{Na}^+$ ,  $\text{K}^+$ ,  $\text{Ca}^{2+}$ ,  $\text{Mg}^{2+}$ ,  $\text{Fe}^{2+}$ ,  $\text{F}^-$ , and  $\text{H}_2\text{O}$  (e.g. Mysen, 1988). However, their role in defining the structure is often controversial. For example, when there is a charge unit excess<sup>2</sup> their roles are frequently inverted.

The observed systematic decrease in activation energy of viscous flow with the addition of Al (Riebling, 1964; Urbain et al., 1982; Rossin et al., 1964; Riebling, 1966) can be interpreted to reflect decreasing the “(Si, Al) – bridging oxygen” bond strength with increasing Al/(Al+Si). There are, however, some significant differences between the viscous behaviour of aluminosilicate melts as a function of the type of charge-balancing cations for  $\text{Al}^{3+}$ . Such a behaviour is the same as shown by adding some units excess<sup>2</sup> to a liquid having NBO/T=0.

Increasing the alkali excess<sup>3</sup> (AE) results in a non-linear decrease in viscosity, which is more extreme at low contents. In detail however, the viscosity of the strongly peralkaline melts increases with the size  $r$  of the added cation (Hess et al., 1995; Hess et al., 1996).

---

<sup>2</sup> Unit excess here refers to the number of mole oxides added to a fully polymerized configuration. Such a contribution may cause a depolymerization of the structure which is most effective when alkaline earth, alkali and water are respectively added (Hess et al., 1995, 1996; Hess and Dingwell, 1996).

<sup>3</sup> Alkali excess (AE) being defined as the mole of alkalis in excess after the charge-balancing of  $\text{Al}^{3+}$  (and  $\text{Fe}^{3+}$ ) assumed to be in tetrahedral coordination. It is calculated by subtracting the molar percentage of  $\text{Al}_2\text{O}_3$  (and  $\text{Fe}_2\text{O}_3$ ) from the sum of the molar percentages of the alkali oxides regarded as network modifying.

Earth alkaline saturated melt instead exhibit the opposite trend although they have a lower effect on viscosity (Dingwell et al., 1996; Hess et al., 1996) (Fig. 2.8).

Iron content as  $\text{Fe}^{3+}$  or  $\text{Fe}^{2+}$  also affects melt viscosity. Because NBO/T (and consequently the degree of polymerisation) depends on  $\text{Fe}^{3+}/\Sigma\text{Fe}$  also the viscosity is influenced by the presence of iron and by its redox state (Cukierman and Uhlmann, 1974; Dingwell and Virgo, 1987; Dingwell, 1991). The situation is even more complicated as the ratio  $\text{Fe}^{3+}/\Sigma\text{Fe}$  decreases systematically as the temperature increases (Virgo and Mysen, 1985). Thus, iron-bearing systems become increasingly more depolymerised as the temperature is increased. Water also seems to provide a restricted contribution to the oxidation of iron in relatively reduced magmatic liquids, whereas in oxidized calk-alkaline magma series, the presence of dissolved water will not largely influence melt ferric-ferrous ratios (Gaillard et al., 2001).

How important the effect of iron and its oxidation state in modifying the viscosity of a silicate melt (Dingwell and Virgo, 1987; Dingwell, 1991) is still unclear and under debate. On the basis of a wide range of spectroscopic investigations, ferrous iron behaves as a network modifier in most silicate melts (Cooney et al., 1987; and Waychunas et al., 1983 give alternative views). Ferric iron, on the other hand, occurs both as a network former (coordination IV) and as a modifier. As a network former, in  $\text{Fe}^{3+}$ -rich melts,  $\text{Fe}^{3+}$  is charge balanced with alkali metals and alkaline earths (Cukierman and Uhlmann, 1974; Dingwell and Virgo, 1987).

Physical, chemical and thermodynamic information for Ti-bearing silicate melts mostly

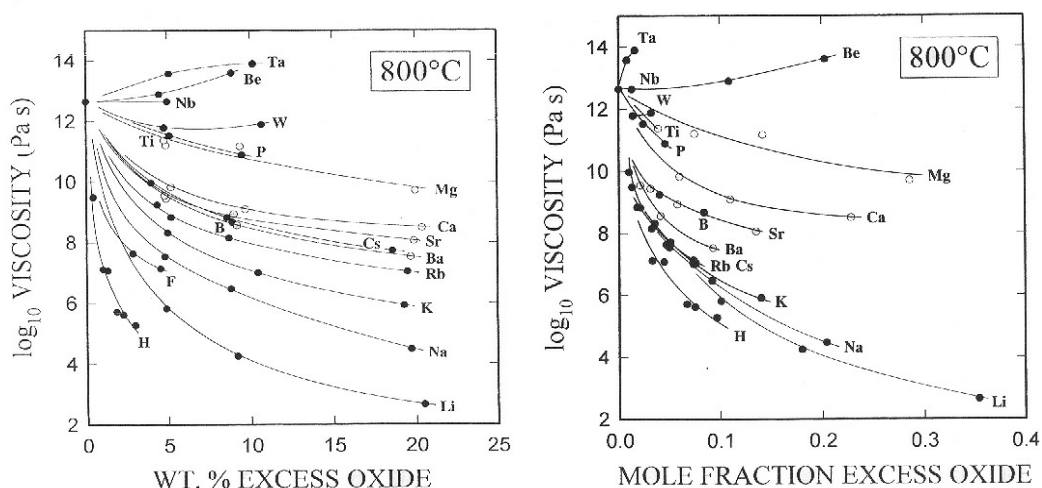


Fig. 2.8 :The effects of various added components on the viscosity of a haplogranitic melt compared at 800 °C and 1 bar (From Dingwell et al., 1996)

agree to attribute a polymerising role of  $\text{Ti}^{4+}$  in silicate melts (Mysen, 1988). The viscosity of

fully polymerised melts depends mainly on the strength of the Al-O-Si and Si-O-Si bonds. Substituting the Si for Ti results in weaker bonds. Therefore as TiO<sub>2</sub> content increases the viscosity of the melts is reduced (Mysen et al., 1980). Ti-rich silica melts and silica-free titanate melts are some exceptions that indicate octahedrally coordinated Ti<sup>4+</sup> (Mysen, 1988).

The most effective network modifier is H<sub>2</sub>O. For example, the viscosity of a rhyolite-like composition at eruptive temperature, decreases by up to 1 and 6 orders due to the addition of an initial 0.1 and 1 wt%, respectively (e.g. Hess and Dingwell, 1996). Such an effect nevertheless strongly diminishes with further addition and tends to level off over 2 wt% (Fig. 2.9).

In chapter 6 a model which calculates the viscosity of several different silicate melts as a function of water content is presented. Such a model provides accurate calculations at experimental conditions and allows interpretations of the eruptive behaviour of several “effusive types”.

Further investigations are necessary to fully understand the structural complexities of the “degree of polymerisation” in silicate melts.

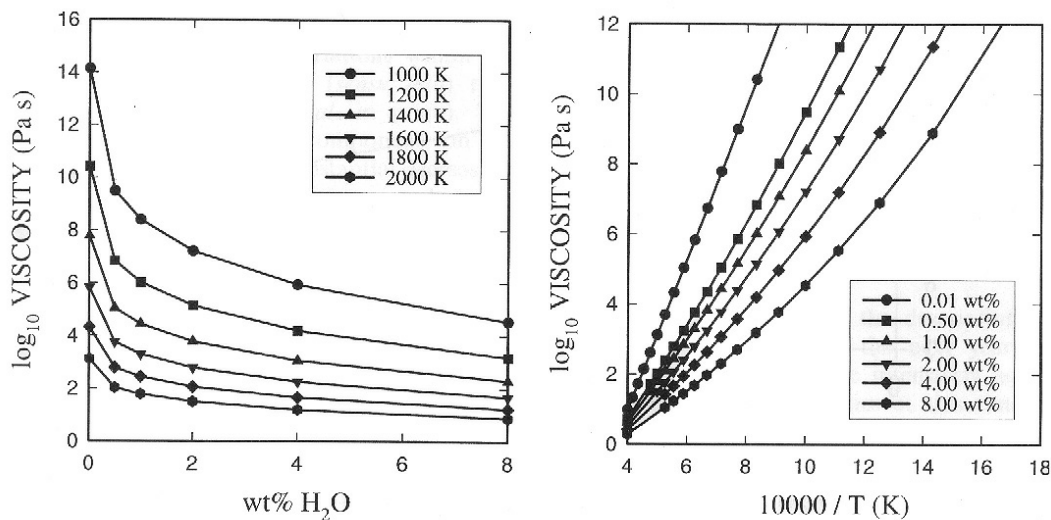


Fig. 2.9.: The temperature and water content dependence of the viscosity of haplogranitic melts [From Hess and Dingwell, 1996].

### 3. Experimental methods

#### 3.1. General procedure

Total rocks or the glass matrices of selected samples were used in this study. To separate crystals and lithics from glass matrices, techniques based on the density and magnetic properties contrasts of the two components were adopted. The samples were then melted and homogenized before low viscosity measurements ( $10^{-0.5} - 10^5$  Pa·s) were performed at temperature from 1050 to 1600 °C and room pressure using a concentric cylinder apparatus. The glass compositions were then measured using a Cameca SX 50 electron microprobe.

These glasses were then used in micropenetration measurements and to synthesize hydrated samples.

Three to five hydrated samples were synthesised from each glass. These syntheses were performed in a piston cylinder apparatus at 10 Kbars.

Viscometry of hydrated samples was possible in the high viscosity range from  $10^{8.5}$  to  $10^{12}$  Pa·s, where crystallization and exsolution kinetics are significantly reduced. Measurements of both dry and hydrated samples were performed over a range of temperatures about 100°C above their glass transition temperature. Fourier-transform-infrared (FTIR) spectroscopy and Karl Fischer titration technique (KFT) were used to measure the concentrations of water in the samples after their high-pressure synthesis and after the viscosimetric measurements had been performed.

Finally, the calorimetric  $T_g$  were determined for each sample using a Differential Scanning Calorimetry (DSC) apparatus (Pegasus 404 C) designed by Netzsch.

#### 3.2. Experimental measurements

##### 3.2.1. Concentric cylinder

The high-temperature shear viscosities were measured at 1 atm in the temperature range between 1100 and 1600 °C using a Brookfield HBTD (full-scale torque =  $5.75 \cdot 10^{-1}$  Nm) stirring device. The material (about 100 grams) was contained in a cylindrical Pt<sub>80</sub>Rh<sub>20</sub> crucible (5.1 cm height, 2.56 cm inner diameter and 0.1 cm wall thickness). The viscometer head drives a spindle at a range of constant angular velocities (0.5 up to 100 rpm) and

digitally records the torque exerted on the spindle by the sample. The spindles are made from the same material as the crucible and vary in length and diameter. They have a cylindrical cross section with 45° conical ends to reduce friction effects.

The furnace used was a Deltech Inc. furnace with six MoSi<sub>2</sub> heating elements. The crucible is loaded into the furnace from the base (Dingwell, 1986; Dingwell and Virgo, 1988 and Dingwell, 1989a) (Fig 3.1 shows details of the furnace).

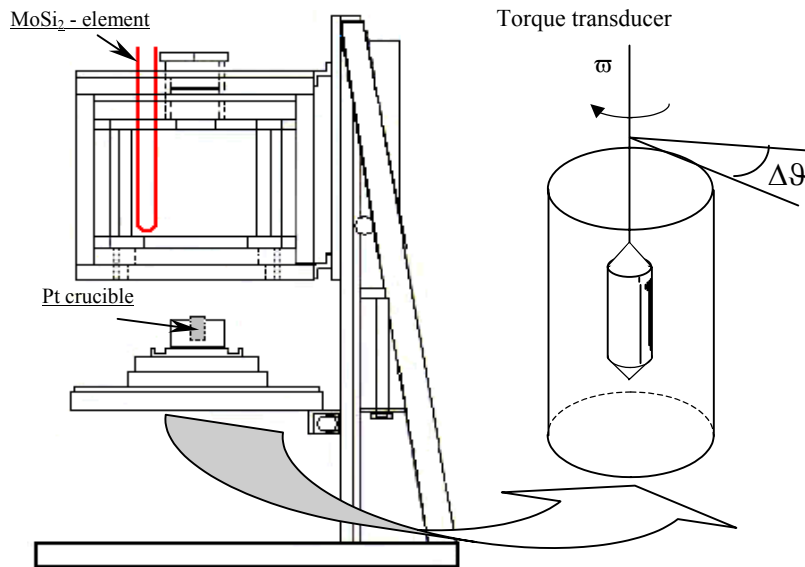


Fig. 3.1.: Schematic diagram of the concentric cylinder apparatus. The heating system Deltech furnace, position and shape of one of the 6 MoSi<sub>2</sub> heating elements is illustrated in the figure. Details of the Pt<sub>80</sub>Rh<sub>20</sub> crucible and the spindle shape are shown on the right. The stirring apparatus is coupled to the spindle through a hinged connection.

The spindle and the head were calibrated with a Soda – Lime – Silica glass NBS No. 710 whose viscosity as a function of temperature is well known.

The concentric cylinder apparatus can determine viscosities between 10<sup>-1</sup> and 10<sup>5</sup> Pa·s with an accuracy of  $\pm 0.05 \cdot \log_{10}$  Pa·s.

Samples were fused and stirred in the Pt<sub>80</sub>Rh<sub>20</sub> crucible for at least 12 hours and up to 4 days until inspection of the stirring spindle indicated that melts were crystal- and bubble-free. At this point the torque value of the material was determined using a torque transducer on the stirring device. Then viscosity was measured in steps of decreasing temperature of 25 to 50 °C/min. Once the required steps have been completed the temperature was increased to the initial value to check if any drift of the torque values have occurred which may be due to volatilisation or instrument drift. For the samples here investigated no such drift was observed indicating that the samples maintained their compositional integrity. In fact, close inspection

of the chemical data for the most peralkaline sample (MB5) (this corresponds to the refused equivalent of sample MB5-3.61 from Gottsmann and Dingwell, 2001), reveals that fusing and dehydration have no effect on major element chemistry as alkali loss due to potential volatilization is minute, if not absent.

Finally, after the high temperature viscometry all the remelted specimens were removed from the furnace and allowed to cool in air within the platinum crucibles. An exception to this was the Basalt from Mt. Etna; this was melted and then rapidly quenched by pouring material on an iron plate, in order to avoid crystallization. Cylinders (6-8 mm in diameter) were cored out of the cooled melts and cut into disks 2-3 mm thick. Both ends of these disks were polished and stored in a dessicator until use in micropenetration experiments.

### 3.2.2 Piston cylinder

Powders from the high temperature viscometry were loaded together with known amounts of doubly distilled water into platinum capsules with an outer diameter of 5.2 mm, a wall thickness of 0.1 mm and a length from 14 to 15 mm. The capsules were then sealed by arc welding. To check for any possible leakage of water, and hence weight loss, they were weighted before and after being in an oven at 110° C for at least an hour. This was also useful to obtain a homogeneous distribution of water in the glasses inside the capsules. Syntheses of hydrous glasses were performed with a piston cylinder apparatus at  $P=10$  Kbars ( $\pm 20$  bars) and  $T$  ranging from 1400 to 1600 °C  $\pm 15$  °C. The samples were held for a sufficient time to guarantee complete homogenisation of H<sub>2</sub>O dissolved in the melts (run duration between 15 to 180 mins). After the run, the samples were quenched isobarically (estimated quench rate from dwell  $T$  to  $T_g$ : 200°C/min; estimated successive quench rate from  $T_g$  to room temperature: 100°C/min.) and then slowly decompressed (decompression time between 1 to 4 hours). To reduce iron loss from the capsule in iron-rich samples, the duration of the experiments was kept to a minimum (15 to 37 mins). An alternative technique used to prevent iron loss was the placing of a graphite capsule within the Pt capsule. Graphite obstacles the high diffusion of iron within the Pt. However, initial attempts to use this method failed as iron-bearing glasses synthesised with this technique were polluted with graphite, fractured and too small to be used in low temperature viscometry. Therefore this technique was abandoned.

The glasses were cut into 1 to 1.5 mm thick disks, doubly polished, dried and kept in a dessicator until their use in micropenetration viscometry.

### 3.2.3. Micropenetration technique

The low temperature viscosities were measured using a micropenetration technique (Hess et al., 1995 and Dingwell et al., 1996). This involves determining the rate at which an hemispherical Ir-indenter moves into the melt surface under a fixed load. These measurements

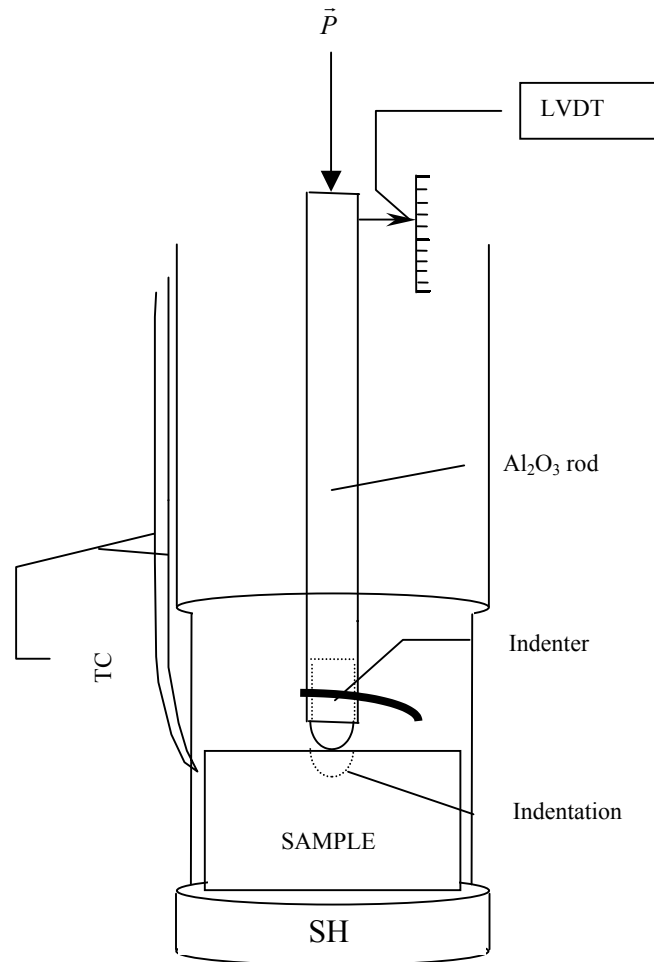


Fig. 3.2.: Schematic structure of the Bähr 802 V dilatometer modified for the micropenetration measurements of viscosity. The force  $P$  is applied to the  $\text{Al}_2\text{O}_3$  rod and directly transmitted to the sample which is penetrated by the Ir-Indenter fixed at the end of the rod. The movement corresponding to the depth of the indentation is recorded by a LVDT inductive device and the viscosity value calculated using Eq. 3.1. The measuring temperature is recorded by a thermocouple (TC in the figure) which is positioned as closest as possible to the top face of the sample. SH is a silica sample-holder.

were performed using a Bähr 802 V vertical push-rod dilatometer. The sample is placed in a silica rod sample holder under an Argon gas flow. The indenter is attached to one end of an alumina rod (Fig. 3.2).

The other end of the alumina rod is attached to a mass. The metal connection between the alumina rod and the weight pan acts as the core of a calibrated linear voltage displacement transducer (LVDT) (F.g. 3.2).. The movement of this metal core as the indenter is pushed into the melt yields the displacement. The absolute shear viscosity is determined via the following equation:

$$\eta = \frac{0.1875 \cdot P \cdot t}{r^{0.5} \alpha^{1.5}} \quad (3.1)$$

(Pocklington, 1940; Tobolsky and Taylor, 1963) where  $P$  is the applied force,  $r$  is the radius of the hemisphere,  $t$  is the penetration time and  $\alpha$  is the indentation distance. This provides an accurate viscosity value if the indentation distance is lower than 150 – 200 microns. The applied force for the measurements performed in the present work was about 1.2 N. The technique allows viscosity to be determined at T up to 1100°C in the range  $10^{8.5}$  to  $10^{12}$  Pa·s without any problems with vesiculation. One advantage of the micropenetration technique is that it only requires small amounts of sample (other techniques used for high viscosity measurements, such as parallel plates and fiber elongation methods instead necessitate larger amount of material).

The hydrated samples have a thickness of 1-1.5 mm, which differs from the about 3 mm optimal thickness of the anhydrous samples (about 3 mm). This difference is corrected using an empirical factor, which is determined by comparing sets of measurements performed on one Standard with a thickness of 1mm and another with a thickness of 3 mm. The bulk correction is subtracted from the viscosity value obtained for the smaller sample.

The samples were heated in the viscometer at a constant rate of 10 K/min to a temperature around 150 K below the temperature at which the measurement was performed. Then the samples were heated at a rate of 1 to 5 K/min to the target temperature, where they were allowed to structurally relax during an isothermal dwell of between 15 (mostly for hydrated samples) and 90 mins (for dry samples). Subsequently the indenter was lowered to penetrate the sample. Each measurement was performed at isothermal conditions using a new sample.

The *indentation - time* traces resulting from the measurements were processed using the software described by Hess (1996). Whether exsolution or other kinetics processes occurred during the experiment can be determined from the geometry of these traces. Measurements

which showed evidence of these processes were not used. An illustration of indentation-time trends is given in Figure 3.3 and 3.4.

Finally, the homogeneity and the stability of the water contents of the samples were checked using FTIR spectroscopy before and after the micropenetration viscometry using the methods described by Dingwell et al. (1996). No loss of water was detected.

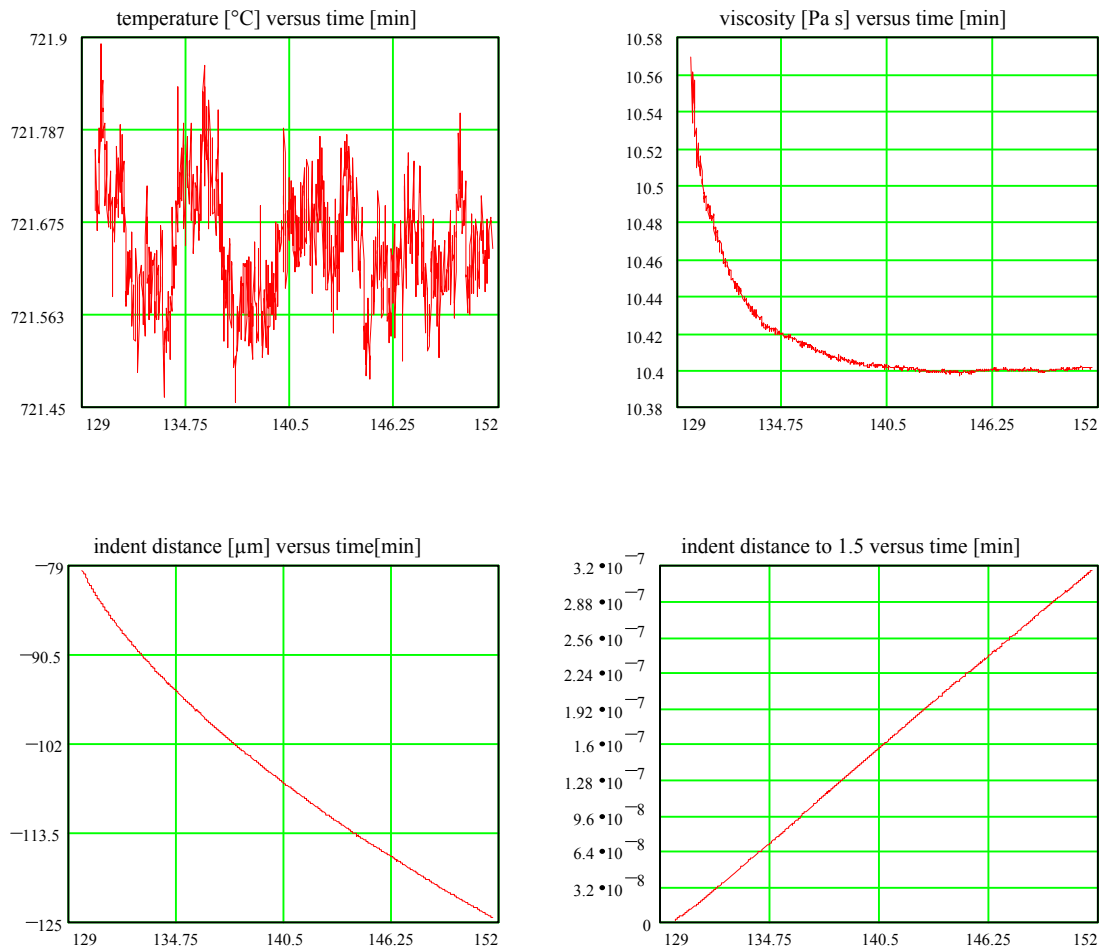


Fig. 3.3.: Operative windows of the temperature, indentation, viscosity vs time traces for one of the measured dry sample. The top left diagram shows the variation of temperature with time during penetration; the top right diagram the viscosity calculated using eqn. 3.1, whereas the bottom diagrams represent the indentation – time traces and its 1.5 exponential form, respectively. Viscosity corresponds to the constant value (10.4 log unit) reached after about 20 mins. Such samples did not show any evidence of crystallization, which would have corresponded to an increase in viscosity. See Fig. 3.4.

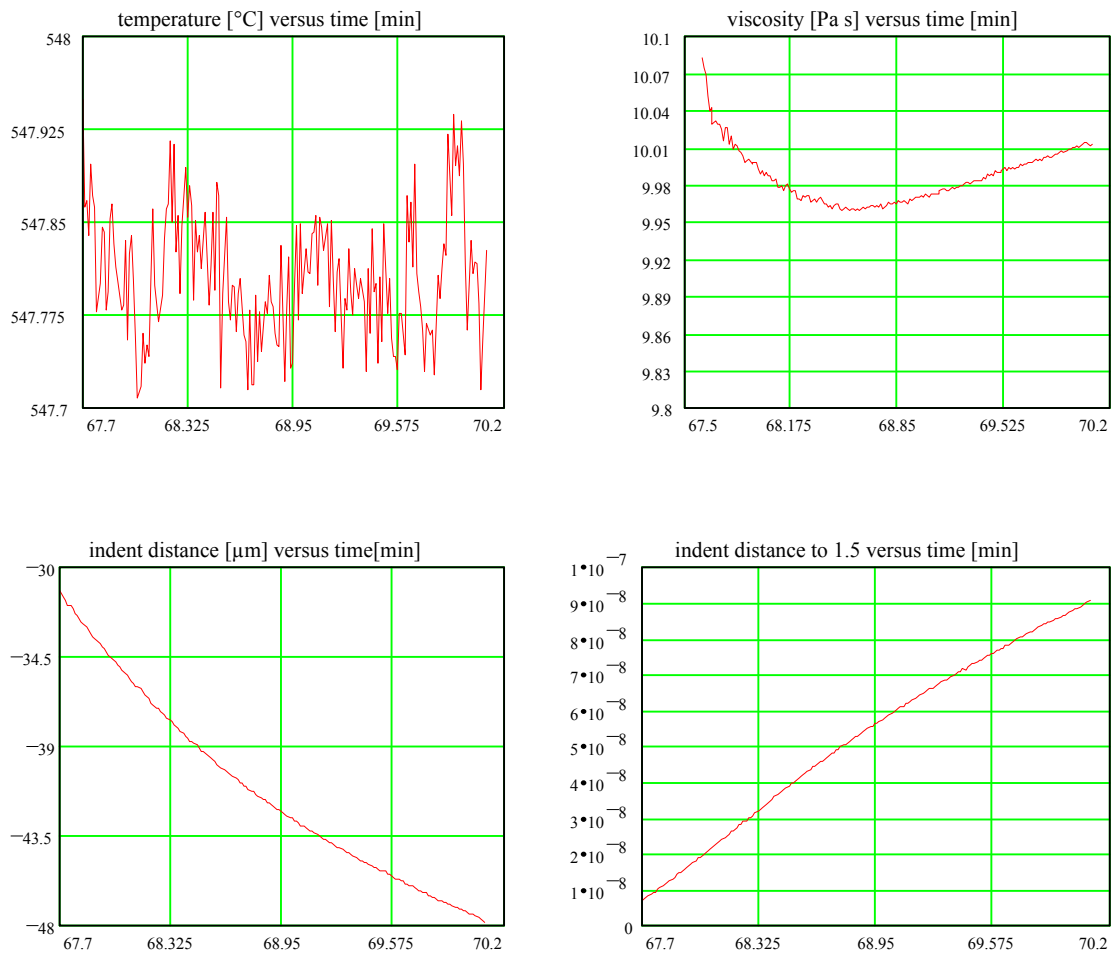


Fig. 3.4.: Temperature, indentation, viscosity vs time traces for one of the hydrated samples. Viscosity did not reach a constant value. Likely because of exsolution of water a viscosity increment is observed. The sample was transparent before the measurement and became translucent during the measurement suggesting that water had exsolved.

### 3.2.4. Fourier-transform infrared (FTIR) spectroscopy

FTIR spectroscopy was used to measure water contents. Measurements were performed on the materials synthesised using the piston cylinder apparatus and then again on the materials after they had been analysed by micropenetration viscometry in order to check that the water contents were homogeneous and stable.

Doubly polished thick disks with thickness varying from 200 to 1100  $\mu\text{m}$  ( $\pm 3$ )  $\mu$  were prepared for analysis by FTIR spectroscopy. These disks were prepared from the synthesised glasses initially using an alumina abrasive and diamond paste with water or ethanol as a lubricant. The thickness of each disks was measured using a Mitutoyo digital micrometer.

A Bruker IFS 120 HR fourier transform spectrophotometer operating with a vacuum system was used to obtain transmission infrared spectra in the near-IR region (2000 – 8000  $\text{cm}^{-1}$ ) using a W source,  $\text{CaF}_2$  beam-splitter and a MCT (Mg Cd Te) detector. The doubly polished disks were positioned over an aperture in a brass disc so that the infrared beam was aimed at areas of interest in the glasses. Typically, 200 to 400 scans were collected for each spectrum. Before the measurement of the sample spectrum a background spectrum was taken in order to determine the spectral response of the system and then this was subtracted from the sample spectrum. The two main bands of interest in the near-IR region are at 4500 and 5200  $\text{cm}^{-1}$ . These are attributed to the combination of stretching and bending of X-OH groups and the combination of stretching and bending of molecular water, respectively (Scholze, 1960; Stolper 1982; Newmann et al., 1986). A peak at about 4000  $\text{cm}^{-1}$  is frequently present in the glasses analysed, which is an unassigned band related to total water (Stolper, 1982; Withers and Behrens, 1999).

All of the samples measured were iron-bearing (total iron between 3 and 10 wt% ca.), and for some samples iron loss to the platinum capsule during the piston cylinder syntheses was observed. In these cases, only spectra measured close to the middle of the sample were used to determine water contents. To investigate iron loss and crystallisation of iron rich crystals infrared analyses were fundamental. It was observed that even if the iron peaks in the FTIR spectrum were not homogeneous within the samples, this did not affect the heights of the water peaks.

The spectra (between 5 and 10 for each sample) were corrected using a third order polynomials baseline fitted through fixed wavelenght in correspondence of the minima points (Sowerby and Keppler, 1999, Ohlhorst et al., 2001). This method is called the flexicurve correction. The precision of the measurements is based on the reproducibility of the measurements of glass fragments repeated over a long period of time and on the errors caused

by the baseline subtraction. Uncertainties on the total water contents is between 0.1 up to 0.2 wt%. (Sowerby and Keppler, 1999; Ohlhorst et al., 2001).

The concentration of OH and H<sub>2</sub>O can be determined from the intensities of the near-IR (NIR) absorption bands using the Beer -Lambert law:

$$c_{mol.H_2O} = \frac{18.02 \cdot A_{mol.H_2O}}{d \cdot \rho \cdot \epsilon_{mol.H_2O}} \quad (3.2.a); \quad c_{OH} = \frac{18.02 \cdot A_{OH}}{d \cdot \rho \cdot \epsilon_{OH}} \quad (3.2.b)$$

where  $c_{mol.H_2O,OH}$  are the concentrations of molecular water and hydroxyl species in weight percent, 18.02 is the molecular weight of water, the absorbance  $A_{mol.H_2O,OH}$  denote the peak heights of the relevant vibration band (non-dimensional),  $d$  is the specimen thickness in cm,  $\epsilon_{mol.H_2O,OH}$  are the linear molar absorptivities (or extinction coefficients) in liter/mole -cm and  $\rho$  is the density of the sample (§ 3.2.5.) in g/liter. The total water content is given by the sum of Eq. 3.2.a and 3.2.b.

The extinction coefficients are dependent on composition (e.g. Ihinger et al., 1994). Literature values of these parameters for different natural compositions are scarce. For the Teide phonolite, extinction coefficients from literature (Carroll and Blank, 1997) were used as obtained on materials with composition very similar to our. For the Etna basalt absorptivity coefficients values from Dixon and Stolper (1995) were used. The water contents of the glasses from the Agnano Monte Spina and Vesuvius 1631 eruptions were evaluated by measuring the heights of the peaks at approximately 3570 cm<sup>-1</sup> attributed to the fundamental OH-stretching vibration. Water contents and relative speciation are reported in Table 2.

Application of the Beer-Lambert law, requires knowledge of the thickness and density of both dry and hydrated samples. The thickness of each glass disk was measured with a digital Mitutoyo micrometer (precision  $\pm 3 \cdot 10^{-4}$  cm). Densities were determined by the method outlined below.

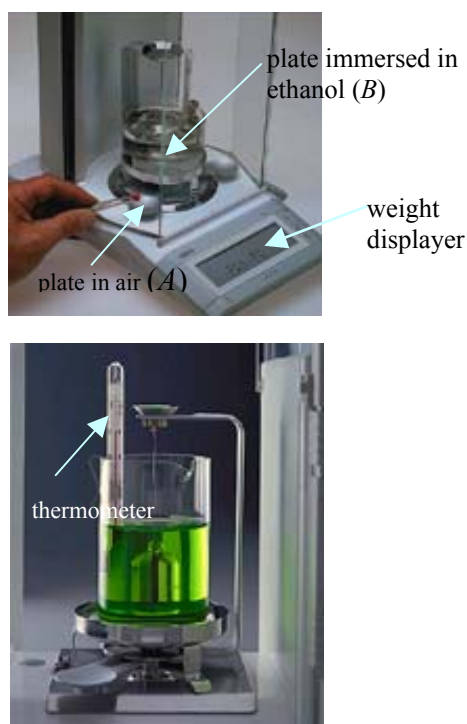
### 3.2.5. Density determination

Densities of the samples were determined before and after the viscosity measurements using a differential Archimedean method. The weight of glasses was measured both in air and in ethanol using an AG 204 Mettler Toledo and a density kit (Fig. 3.5). Density is calculated as follows:

$$\rho_{glass} = \frac{A}{A - B} \cdot \rho_{ethanol,T} \quad (4.3)$$

where  $A$  is the weight in air of the sample,  $B$  is the weight of the sample measured in ethanol and  $\rho_{ethanol}$  is the density of ethanol at the temperature at the time of the measurement  $T$ . The temperature is recorded using a thermometer immersed in the ethanol (Fig 3.5). Before starting the measurement ethanol is allowed to equilibrate at room temperature for about an hour. The density data measured by this method has a precision of  $0.001 \text{ g/cm}^3$ . They are reported in Table 2.

Fig. 3.5.: AG 204 Mettler Toledo balance with the density kit. The density kit is represented in detail in the lower figure. In the upper representation it is possible to see the plates on which the weight in air ( $A$  in Eq. 4.3) and in a liquid ( $B$  in Eq. 4.3) with known density ( $\rho_{ethanol}$ , in this case) are recorded.



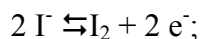
### 3.2.6. Karl – Fischer – titration (KFT)

The absolute water content of the investigated glasses was determined using the Karl – Fischer titration (KFT) technique. It has been established that this is a powerful method for the determination of water contents in minerals and glasses (e.g. Holtz et al., 1992, 1993, 1995; Behrens 1995, Behrens et al., 1996; Ohlhorst et al., 2001).

The advantage of this method is the small amount of material necessary to obtain high quality results (ca. 20 mg).

The method is based on a titration involving the reaction of water, in the presence of iodine:  $I_2 + SO_2 + H_2O \rightleftharpoons 2 HI + SO_3$ . The water content can be directly determined from the

quantity of electrons required for the electrolyses.  $I_2$  is electrolytically generated (coulometric titration) by the following reaction:



one mole of  $I_2$  reacts quantitatively with one mole of water and, therefore, 1 mg of water is equivalent to 10.71 coulombs. The coulometer used was a Mitsubishi® CA 05 using pyridine-free reagents (Aquamicron AS, Aquamicron CS)

In principle, no standards are necessary for the calibration of the instrument, but the correct conditions of the apparatus are verified once a day measuring loss of water from a muscovite powder. However, for the analyses of solid materials, additional steps are involved in the measurement procedure beside the titration itself. Water must be transported to the titration cell. Hence, tests are necessary to guarantee that what is detected is the total amount of water. The transport medium consisted of a dried argon stream.

The heating procedure depends on the anticipated water concentration in the samples. The heating program has to be chosen considering that as much water as possible has to be liberated within the measurement time, possibly avoiding sputtering of the material. A convenient heating rate is in the order of 50 - 100 °C/min.

A schematic representation of the KFT apparatus is given in figure 3.6 (from Behrens et al., 1996).

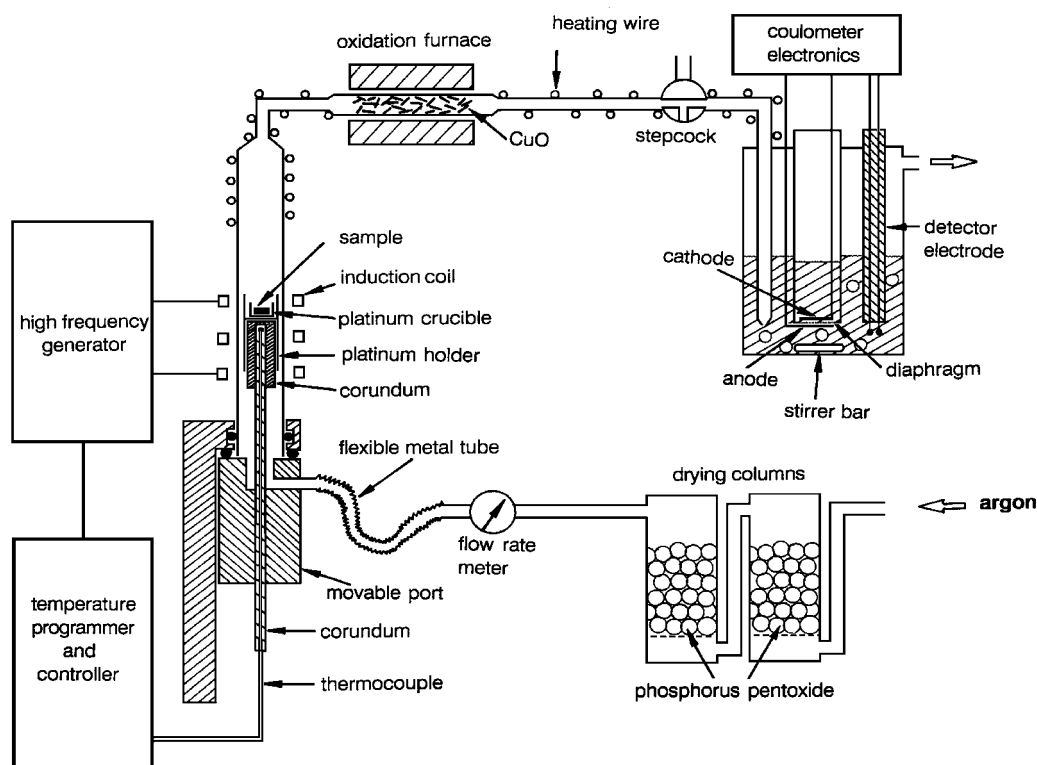


Fig. 3.6.: Scheme of the KFT apparatus from Behrens et al. (1996).

It has been demonstrated for highly polymerised materials (Behrens, 1995) that a residual amount of water of  $0.1 \pm 0.05$  wt% cannot be extracted from the samples. This constitutes therefore the error in the absolute water determination. Nevertheless such error value is minor for depolymerised melts. Consequently, all water contents measured by KFT are corrected on a case to case basis, depending on their composition (Ohlhorst et al., 2001).

Single chips of the samples (10 – 30 mg) is loaded into the sample chamber and wrapped in platinum foil to contain explosive dehydration. In order to extract water, the glasses is heated by using a high-frequency generator (Linn<sup>®</sup>, HTG 1000/1,3) from room temperature to about 1300° C. The temperature is measured with a Pt/Pt<sub>90</sub>Rh<sub>10</sub> thermocouple (type S) close to the sample. Typical the duration run duration is between 7 to 10 minutes. Further details can be found in Behrens et al. (1996). Results of the water contents for the samples measured in this work are given in Table 13.

### 3.2.7. Differential Scanning Calorimetry (DSC)

Calorimetric glass transition temperatures were determined using a differential scanning calorimeter (NETZSCH<sup>®</sup> DSC 404 Pegasus). The peaks in the variation of specific heat capacity at constant pressure ( $C_p$ ) with temperature is used to define the calorimetric glass transition temperature. Prior to analysis of the samples the temperature of the calorimeter was calibrated using the melting temperatures of standard materials (In, Sn, Bi, Zn, Al, Ag and Au). Then a baseline measurement was taken where two empty Pt/Rh crucibles were loaded into the DSC and then the DSC was calibrated against the  $C_p$  of a single sapphire crystal.

Finally the samples were analysed and their  $C_p$  as a function of temperature calculated. Doubly polished glass sample disks were prepared and placed in Pt/Rh crucibles and heated from 40° C across the glass transition into the supercooled liquid at a rate of 5 K/min. In order to allow complete structural relaxation the samples were heated to a temperature about 50 K above the glass transition temperature. Then a set of thermal treatments was applied to the samples during which cooling rates of 20, 16, 10, 8 and 5 K/min were matched by subsequent heating rates (determined to within +/- 2 K). The glass transition temperatures were set in relation to the experimentally applied cooling rates (Fig. 3.7).

DSC is also a useful tool to evaluate whether any phase transition (e.g. crystallization, water nucleation or exsolution) occurs during heating or cooling. In the rheological measurements this assumes a certain importance when working with iron-rich samples which are easy to crystallize and may affect viscosity (e.g. viscosity is influenced by the presence of crystals and by the variation of composition consequent to crystallization. For that reason

DSC was also used to investigate the phase transition that may have occurred in the Etna sample during micropenetration measurements.

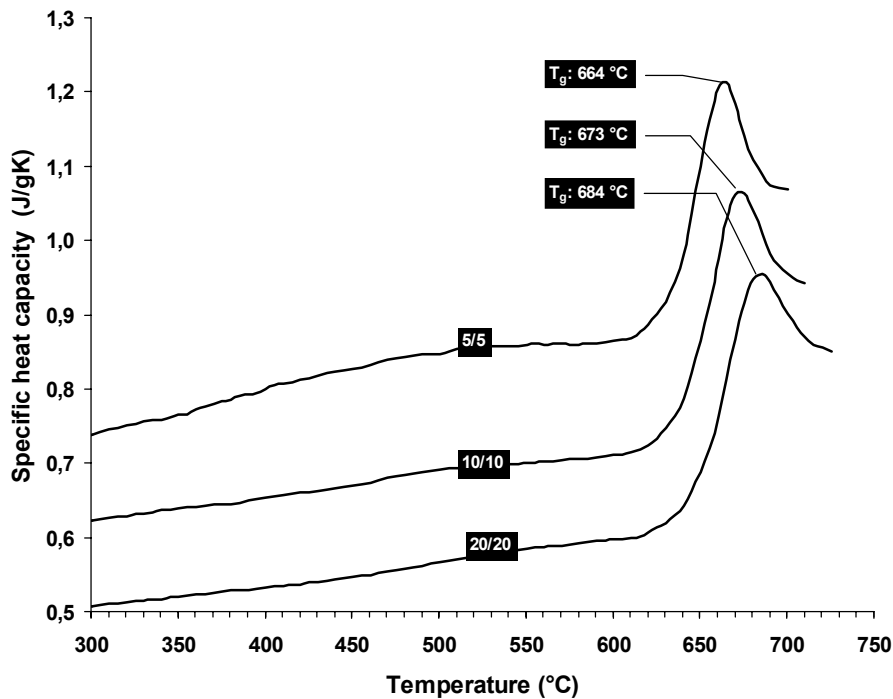


Fig. 3.7.: The specific heat capacity as a function of temperature for one of the investigated basalt sample (R839-5.8). The curves represent  $C_p$ -traces obtained during reheating the sample in the calorimeter to record the respective glass transition temperature as a function of cooling rate. With matching heating and cooling rates of 20, 10, and 5 K/min such derived glass transition temperatures differ about 20 K. The quantification of the shift in glass transition temperatures (taken as the peak of the  $C_p$ -curve) as a function of cooling rate enables to calculate the activation energy for enthalpic relaxation (Table 11). The curves are displaced along the y-axis for clarity.

## 4. Sample selection

A wide range of compositions derived from different types of eruption were selected to develop the viscosity models.

The chemical compositions investigated during this study are shown in a total alkali vs. silica diagram (Fig. 1.1; after Le Bas, 1986) and include basanite, trachybasalt, phonotephrite, tephriphonolite, phonolite, trachyte and dacite melts. With the exception of one sample (EIF), all the samples are natural, collected in the field.

The compositions investigated are:

- i. synthetic Eifel - basanite (EIF; oxide synthesis composition obtained from C. Shaw, University of Bayreuth, Germany);
- ii. trachybasalt (ETN) from an Etna 1992 lava flow (Italy) collected by M. Coltelli;
- iii.& iv. tephriphonolitic and phonotephritic tephra from the eruption of Vesuvius occurred in 1631 (Italy; Rosi et al., 1993) labelled (Ves\_G\_tot) and (Ves\_W\_tot) respectively;
- v. phonolitic glassy matrices of the tephriphonolitic and phonotephritic tephra from the 1631 eruption of Vesuvius labelled (Ves\_G) and (Ves\_W), respectively;
- vi. alkali - trachytic matrices from the fallout deposits of the Agnano Monte Spina eruption (AMS; Campi Flegrei, Italy), labelled AMS\_B1 and AMS\_D1 (Di Vito et al., 1999);
- vii. phonolitic matrix from the fallout deposit of the Astroni 3.8 ka B.P. eruption (ATN; Campi Flegrei, Italy; Di Vito et al., 1999);
- viii. trachytic matrix from the fallout deposit of the 1538 Monte Nuovo eruption (MNV; Campi Flegrei, Italy);
- ix. phonolite from an obsidian flow associated with the eruption of Montaña Blanca 2 ka B.P. (Td\_ph; Tenerife, Spain Gottsmann and Dingwell, 2001);
- x. trachyte from an obsidian enclave within the Povoação ignimbrite (PVC; Azores, Portugal);
- xi. dacite from the 1993 dome eruption of Mt. Unzen (UNZ; Japan);

Other samples from literature were taken into account as a purpose of comparison. In particular, viscosity determination from Whittington et al. (2000) (sample NIQ and W\_Tph); 2001 (sample W\_T and W\_ph)); Dingwell et al., (1996) (HPG8) and Neuville et al. (1993) (N\_An) were considered to this comparison. The compositional details concerning all of the above mentioned silicate melts are reported in Table 1.

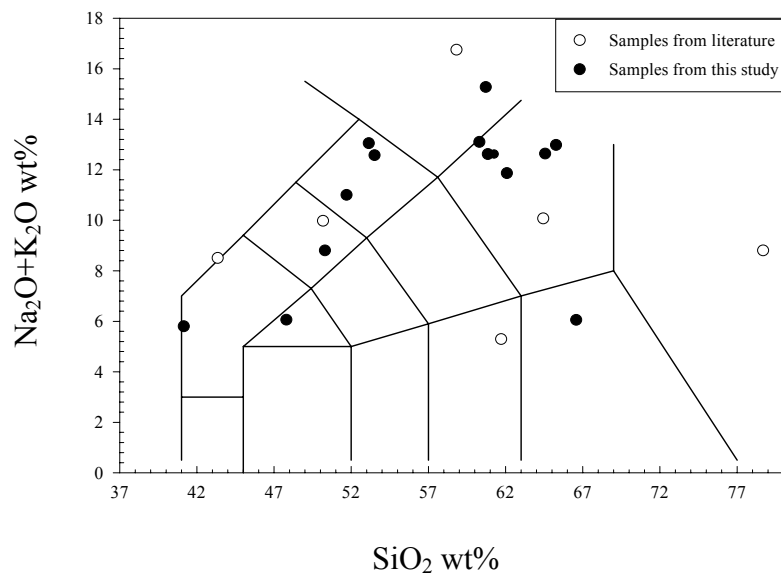


Fig. 4.1: Total alkali vs silica diagram (after Le Bas, 1986) of the investigated compositions. Filled circles are data from this study, open circles represent data from previous works (Whittington et al., 2000, 2001; Dingwell et al., 1996; Neuville et al., 1993).

## 5. Dry silicate melts - viscosity and calorimetry

Future models for predicting the viscosity of silicate melts must find a means of partitioning the effects of composition across a system that shows varying degrees of non-Arrhenian temperature dependence.

Understanding the physics of liquids and supercooled liquids play a crucial role to the description of the viscosity during magmatic processes. To dispose of a theoretical model, or just an empirical description, which fully describes the viscosity of a liquid at all the geologically relevant conditions the problem of defining the physical properties of such materials at “defined conditions” (e.g. across the glass transition, at  $T_0$  (§ 2.1)) must be necessarily approached.

At present the physical description of the role played by glass transition in constraining the flow properties of silicate liquids is mostly referred to the occurrence of the fragmentation of the magma as it crosses such a boundary layer and it is investigated in terms of the differences between the timescales to which flow processes occur and the relaxation times of the magmatic silicate melts (see section 2.1.5). Not much is instead known about the effect on the microscopic structure of silicate liquids with the crossing of glass transition, that is between the relaxation mechanisms and the structure of silicate melts. As well as it is still not understood the physical meaning of other quantities commonly used to describe the viscosity of the magmatic melts. The Tammann-Vogel-Fulcher (TVF) temperature  $T_0$ , for example, is generally considered to represent nothing else than a fit parameter useful to the description of the viscosity of a liquid. Correlations of  $T_0$  with the glass transition temperature  $T_g$  or the Kauzmann temperature  $T_K$  (e.g. Angell, 1988), have been described in literature, without finally providing a clear physical identity of this parameter. The definition of the “fragility index” of a system (§ 2.1), which indicates, via the deviation from an Arrhenian behaviour, the kind of viscous response of a system to the applied forces, is still not univocally defined (Angell, 1984, Ngai et al. 1992).

Properties of multicomponent silicate melt systems and not only simple systems must be analysed to comprehend the complexity of the silicic material and provide physical consistent representations. Nevertheless, it is likely that in the short term, the decisions governing how to expand the non-Arrhenian behaviour in terms of composition will probably derive from empirical study.

In the next sessions an approach to these problems is presented by investigating dry silicate liquids. Newtonian viscosity measurements and calorimetry investigations of natural

multicomponent liquids ranging from strong to extremely fragile have been performed by using the techniques discussed in § 3.2.1, 3.2.3 and 3.2.7 at ambient pressure.

At first (section 5.2) a numerical analysis of the nature and magnitudes of correlations inherent in fitting a non-Arrhenian model (e.g. TVF function) to measurements of melt viscosity is presented. The non-linear character of the non-Arrhenian models ensures strong numerical correlations between model parameters which may mask the effects of composition. How the quality and distribution of experimental data can affect covariances between model parameters is shown.

The extent of non-Arrhenian behaviour of the melt also affects parameter estimation. This effect is explored by using albite and diopside melts as representative of strong (nearly Arrhenian) and fragile (non-Arrhenian) melts, respectively. The magnitudes and nature of these numerical correlations tend to obscure the effects of composition and, therefore, are essential to understand prior to assigning compositional dependencies to fit parameters in non-Arrhenian models.

Later (sections 5.3, 5.4), the relationships between fragility and viscosity of the natural liquids of silicate melts are investigated in terms of their dependence with the composition. Determinations from previous studies (Whittington et al., 2000, 2001; Hess et al., 1995, Neuville et al., 1993) have also been used. Empirical relationships for the fragility and the viscosity of silicate liquids are provided in section 5.3 and 5.4. In particular in section 5.4, an empirical temperature-composition description of the viscosity of dry silicate melts via a 10 parameter equation is presented which allows predicting the viscosity of dry liquids by knowledge of the composition only. Modelling viscosity was possible by considering the relationships between isothermal viscosity calculations and a compositional parameter (SM), here defined, which takes into account the cationic contribution to the depolymerization of silicate liquids.

Finally (section 5.5), a parallel investigation of rheological and calorimetric properties of dry liquids allows the prediction of viscosity at the glass transition during volcanic processes. Such a prediction have been based on the equivalence of the shear stress and enthalpic relaxation time. The results of this study may also be applied to the magma fragmentation process, according to the description of section 2.1.5.

## 5.1. Results

Dry viscosity values are reported in Table 3. Data from this study were compared with those obtained by Whittington et al. (2000, 2001) on analogue compositions (Table 3). Two synthetic compositions, HPG8, a haplogranitic composition (Hess et al., 1995) and a haploandesitic composition (N\_An) (Richet et al., 1993) have been included to the present study. A variety of chemical compositions from this and previous investigation have already been presented in Fig. 4.1, and the compositions in terms of weight% and mole% oxides are reported in Table 1.

Over the restricted range of individual techniques the behaviour of viscosity is Arrhenian. However, the comparison of the high and low temperature viscosity data (Fig. 5.1) indicates that the temperature dependence of viscosity varies from slightly to strongly non-Arrhenian over the viscosity range from  $10^{-1}$  to  $10^{11.6}$ . This further underlines that care must be taken when extrapolating the low/high temperature data to conditions relevant to volcanic processes. At high temperatures samples have similar viscosities, but at low temperature the samples NIQ and Td\_ph are the least viscous and HPG8 the most viscous. This does not necessarily imply a different degree of non-Arrhenian behaviour, as the order could be

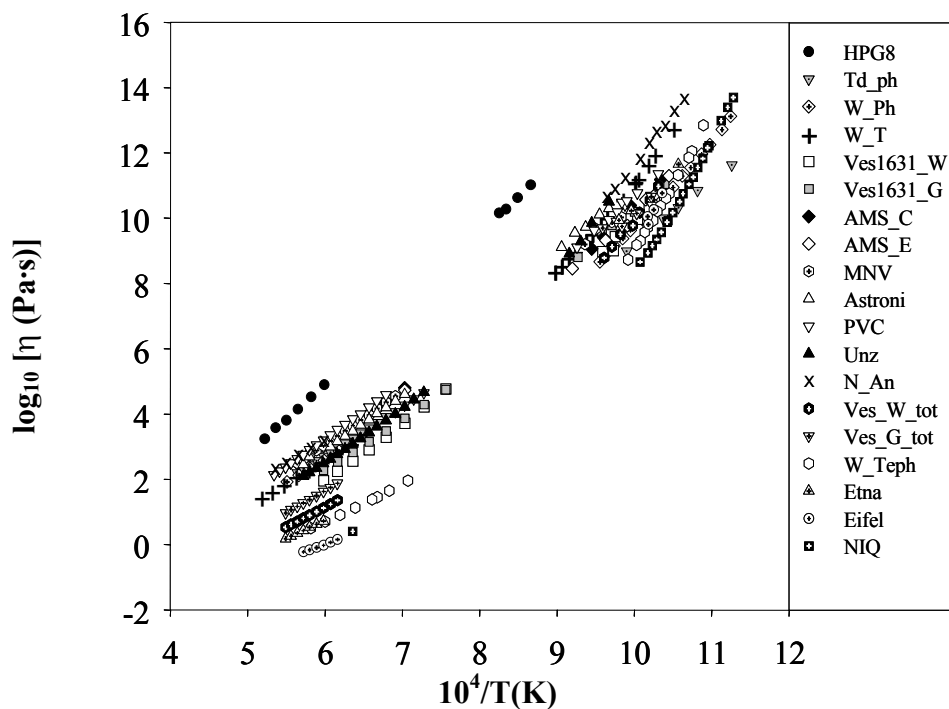


Fig. 5.1.: Dry viscosities (in log unit (Pa·s)) against the reciprocal of temperature. Also shown for comparison are natural and synthetic samples from previous studies [Whittington et al., 2000, 2001; Hess et al., 1995; Richet et al., 1993].

reversed at the highest temperatures. Nevertheless, highly polymerised liquids, such as  $\text{SiO}_2$  or HPG8, reveal different behaviour, as they are more viscous and show a quasi-Arrhenian trend under dry conditions (the variable degree of non-Arrhenian behaviour can be expressed in terms of fragility values as discussed in § 2.1.3.).

The viscosity measured in the dry samples using concentric cylinder and micro-penetration techniques together with measurements from Whittington et al. (2000, 2001), Hess and Dingwell (1996) and Neuville et al. (1993), fitted by the use of the Tammann-Vogel-Fulcher (TVF) equation (Eq. 2.9) (which allows for non-Arrhenian behaviour), provided the adjustable parameters  $A_{TVF}$ ,  $B_{TVF}$  and  $T_0$  (§ 2.1.2). The values of these parameters were calibrated for each composition and are listed in Table 4. Numerical considerations on how to model the non-Arrhenian rheology of dry samples are discussed taking into account the samples investigated in this study, and will be then extended to all the other dry and hydrated samples according to section 5.2.

## 5.2. Modelling the non-Arrhenian rheology of silicate melts: Numerical considerations

### 5.2.1. Procedure strategy

The main challenge of modelling viscosity in natural systems is devising a rational means for distributing the effects of melt composition across the non-Arrhenian model parameters (e.g. Richet, 1984; Richet and Bottinga, 1995; Hess et al., 1996; Toplis et al., 1997; Toplis, 1998; Rössler et al., 1998; Persikov, 1991; Prusevich, 1988). At present, there is no theoretical means of establishing *a priori* the forms of compositional dependence for these model parameters.

The numerical consequences of fitting viscosity-temperature datasets to non-Arrhenian rheological models were explored. This analysis shows that strong correlations and even non-unique estimates of model parameters (e.g.  $A_{TVF}$ ,  $B_{TVF}$ ,  $T_0$  in Eq. 2.9) are inherent to non-Arrhenian models. Furthermore, uncertainties on model parameters and covariances between parameters are strongly affected by the quality and distribution of the experimental data, as well as the degree of non-Arrhenian behaviour.

Estimates of the parameters  $A_{TVF}$ ,  $B_{TVF}$  and  $T_0$  (Eq. 2.9) can be derived for a single melt composition (Fig. 5.2).

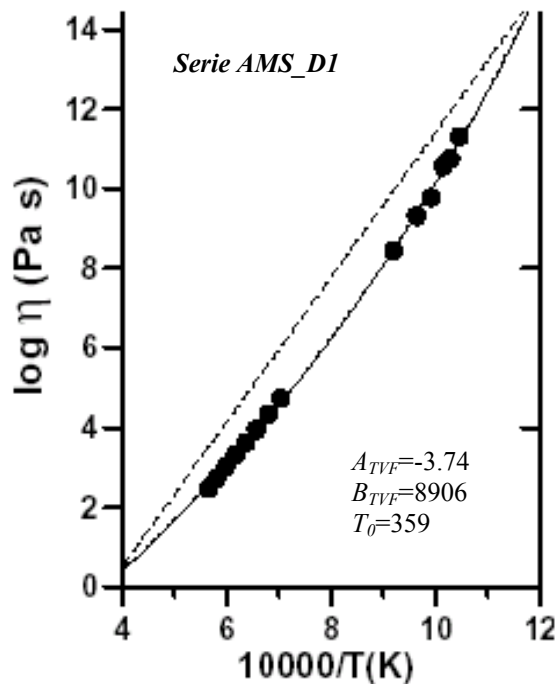


Fig. 5.2.: Viscosities (log units (Pa·s)) vs  $10^4/T(K)$  (Tab. 3) for the AMS\_D1 alkali trachyte, fitted to the TVF (solid line). Dashed line represents hypothetical Arrhenian behaviour

Parameter values derived for a variety of melt compositions can then be mapped against compositional properties to produce functional relationships between the model parameters (e.g.  $A_{TVF}$ ,  $B_{TVF}$  and  $T_0$  in Eq. 2.9) and composition (e.g. Cranmer and Uhlmann, 1981; Richet and Bottinga, 1995; Hess et al., 1996; Toplis et al., 1997; Toplis, 1998). However, detailed studies of several simple chemical systems show that the parameter values have a non-linear dependence on composition (Cranmer and Uhlmann, 1981; Richet, 1984; Hess et al., 1996; Toplis et al., 1997; Toplis, 1998). Additionally, empirical data and a theoretical basis indicate that the parameters  $A_{TVF}$ ,  $B_{TVF}$  and  $T_0$  are not equally dependent on composition (e.g. Richet and Bottinga, 1995; Hess et al., 1996; Rössler et al., 1998; Toplis et al., 1997). Values of  $A_{TVF}$  in the TVF model, for example, represent the high-temperature limiting behaviour of viscosity and tend to have a narrow range of values over a wide range of melt compositions (e.g. Shaw, 1972; Cranmer and Uhlmann, 1981; Hess et al., 1996; Richet and Bottinga, 1995; Toplis et al., 1997). The parameter  $T_0$ , expressed in K, is constrained to be positive in value. As values of  $T_0$  approach zero the melt tends to become increasingly Arrhenian in behaviour. Values of  $B_{TVF}$  are also required to be greater than zero if viscosity is to decrease with increasing temperature. It may be that the parameter  $A_{TVF}$  is less dependent on composition than  $B_{TVF}$  or  $T_0$ ; it may even be a constant for silicate melts.

Below three experimental datasets to explore the nature of covariances that arise from fitting the TVF equation (Eq. 2.9) to viscosity data collected over a range of temperatures were used. The three parameters ( $A_{TVF}$ ,  $B_{TVF}$ ,  $T_0$ ) in the TVF equation are derived by minimizing the  $\chi^2$  function:

$$\chi^2 = \sum_{i=1}^n \left[ \frac{\log \eta_i - A - \frac{B}{T_i - T_0}}{\sigma_i} \right]^2 \quad (5.1)$$

The objective function is weighted to uncertainties ( $\sigma_i$ ) on viscosity arising from experimental measurement. The form of the TVF function is non-linear with respect to the unknown parameters and, therefore, Eq. 5.1 is solved by using conventional iterative methods (e.g. Press et al., 1986). The solution surface to the  $\chi^2$  function (Eq. 5.1) is 3-dimensional (e.g. 3 parameters) and there are other minima to the function that lie outside the range of realistic values of  $A_{TVF}$ ,  $B_{TVF}$  and  $T_0$  (e.g.  $B$  and  $T_0 > 0$ ).

One attribute of using the  $\chi^2$  merit function is that, rather than consider a single solution that coincides with the minimum residuals, a solution region at a specific confidence level (e.g.  $1\sigma$ ; Press et al. 1986) can be mapped. This allows delineation of the full range of parameter values (e.g.  $A_{TVF}$ ,  $B_{TVF}$  and  $T_0$ ) which can be considered as equally valid in the description of the experimental data at the specified confidence level (e.g. Russell and Hauksdóttir, 2001; Russell et al. 2001).

### 5.2.2. Model-induced covariances

The first data set comprises 14 measurements of viscosity (Fig. 5.2) for an alkali-trachyte composition over a temperature range of 973 - 1773 K (AMS\_D1 in Table 3). The experimental data span a wide enough range of temperature to show non-Arrhenian behaviour (Table 3, Fig. 5.2). The gap in the data between 1100 and 1420 K is a region of temperature where the rates of vesiculation or crystallization in the sample exceed the timescales of viscous deformation. The TVF parameters derived from these data are:  $A_{TVF} = -3.74$ ,  $B_{TVF} = 8906$ , and  $T_0 = 359$  (Table 4; Fig. 5.2, solid line).

### 5.2.3. Analysis of covariance

Figure 5.3 is a series of 2-dimensional (2-D) maps showing the characteristic shape of the  $\chi^2$  function (Eq. 5.1). The three maps are mutually perpendicular planes that intersect at the optimal solution and lie within the full 3-dimensional solution space. These particular maps explore the  $\chi^2$  function over a range of parameter values equal to  $\pm 75\%$  of the optimal solution values. Specifically, the values of the  $\chi^2$  function away from the optimal solution by holding one parameter constant (e.g.  $T_0 = 359$  in Fig. 5.3a) and by substituting new values for the other two parameters have been calculated. The contoured versions of these maps simply show the 2-dimensional geometry of the solution surface.

These maps illustrate several interesting features. Firstly, the shapes of the 2-D solution surfaces vary depending upon which parameter is fixed. At a fixed value of  $T_0$ , coinciding with the optimal solution (Fig. 5.3a), the solution surface forms a steep-walled, flat-floored and symmetric trough with a well-defined minimum. Conversely, when  $A_{TVF}$  is fixed (Fig. 5.3 b), the contoured surface shows a symmetric but fanning pattern; the  $\chi^2$  surface dips slightly to lower values of  $B_{TVF}$  and higher values of  $T_0$ . Lastly, when  $B_{TVF}$  is held constant (Fig. 5.3 c), the solution surface is clearly asymmetric but contains a well-defined minimum. Qualitatively, these maps also indicate the degree of correlation that exists between pairs of model parameters at the solution (see below).

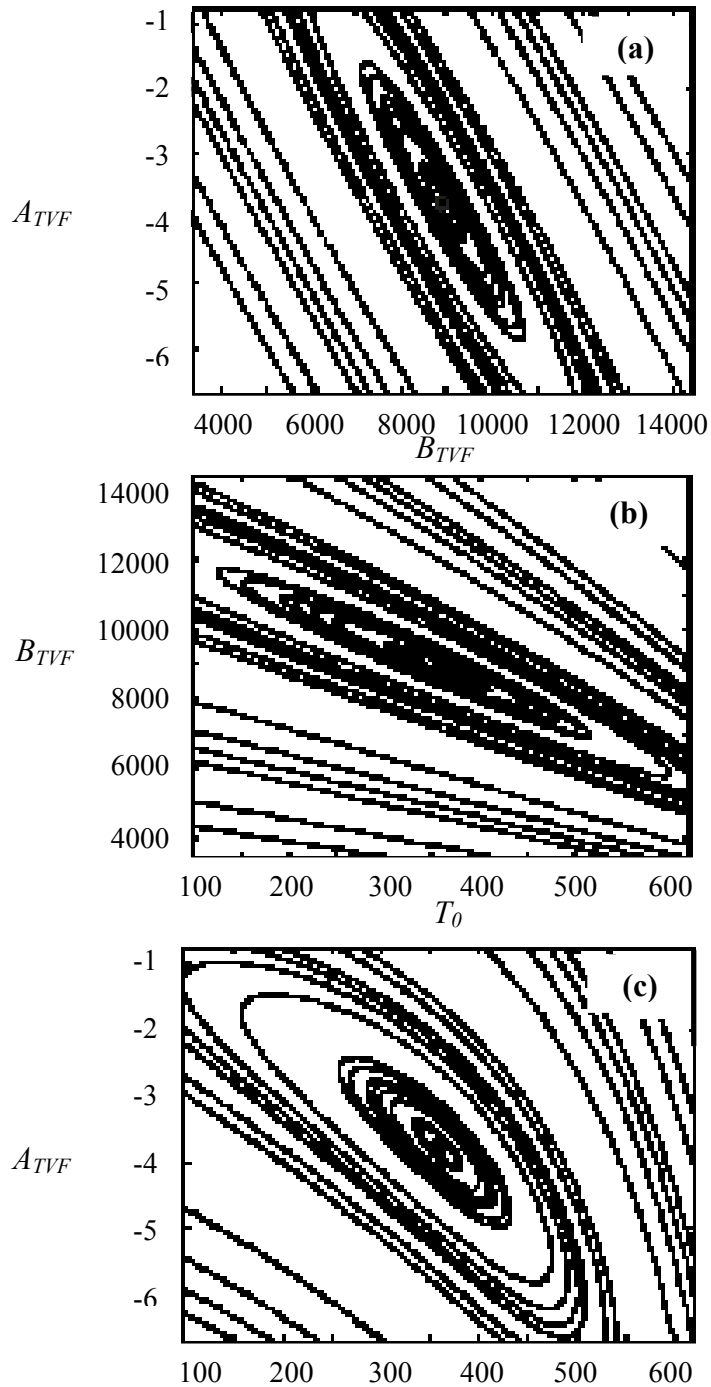


Fig. 5.3.: A contour map showing the shape of the  $\chi^2$  minimization surface (Press et al., 1986) associated with fitting the TVF function to the viscosity data for alkali trachyte melt (Fig. 5.2 and Table 3). The contour maps are created by projecting the  $\chi^2$  solution surface onto 2-D surfaces that contain the actual solution (solid symbol). The maps show the distributions of residuals around the solution caused by variations in pairs of model parameters: a) the  $A_{TVF}$ - $B_{TVF}$ , b) the  $B_{TVF}$ - $T_0$ , and c) the  $A_{TVF}$ - $T_0$ . Values of the contours shown were chosen to highlight the overall shape of the solution surface.

The nature of correlations between model parameters arising from the form of the TVF equation is explored more quantitatively in Fig. 5.4.

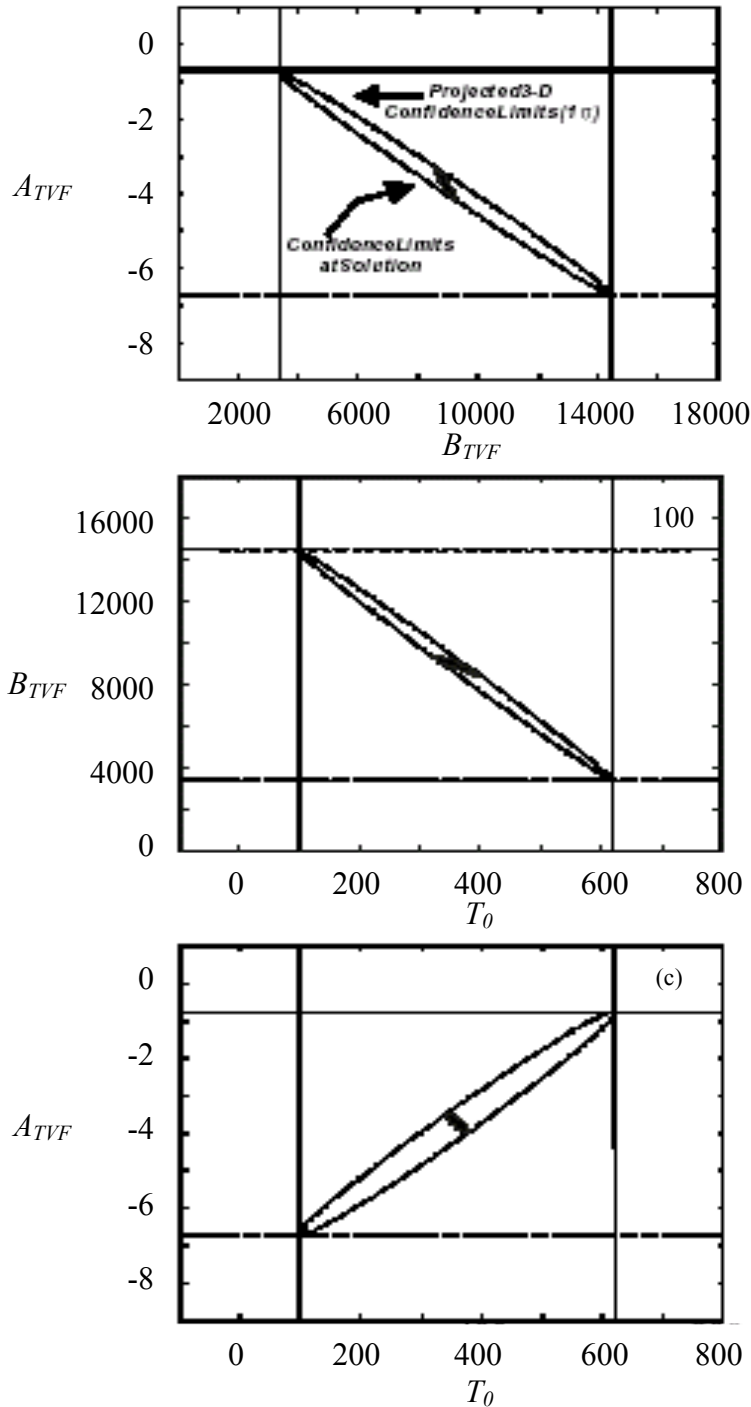


Fig. 5.4.: The solution shown in Fig. 5.3 is illustrated as 2-D ellipses that approximate the 1  $\sigma$  confidence envelopes on the optimal solution. The large ellipses approximate the 1  $\sigma$  limits of the entire solution space projected onto 2-D planes and indicate the full range (dashed lines) of parameter values (e.g.  $A_{TVF}$ ,  $B_{TVF}$ ,  $T_0$ ) that are consistent with the experimental data. Smaller ellipses denote the 1  $\sigma$  confidence limits for two parameters where the third parameter is kept constant (see text and Appendix I).

Specifically, the linear approximations to the 1  $\sigma$  confidence limits of the solution (Press et al., 1986; see Appendix I) have been calculated and mapped. The contoured data in Fig. 5.3 are represented by the solid, smaller ellipses in each of the 2-D projections of Fig. 5.4. These smaller ellipses correspond exactly to a specific contour level ( $\Delta\chi^2 = 16.4$ ; Table 5) and

approximate the  $1 \sigma$  confidence limits for two parameters, if the 3<sup>rd</sup> parameter is fixed at the optimal solution (see Appendix I). For example, the small ellipse in Fig. 4a represents the intersection of the plane  $T_0 = 359$  with a 3-D ellipsoid representing the  $1 \sigma$  confidence limits for the entire solution.

It establishes the range of values of  $A_{TVF}$  and  $B_{TVF}$  permitted if this value of  $T_0$  is maintained.

It shows that the experimental data greatly restrict the values of  $A_{TVF}$  ( $\approx \pm 0.45$ ) and  $B_{TVF}$  ( $\approx \pm 380$ ) if  $T_0$  is fixed (Table 5).

The larger ellipses shown in Fig. 5.4 a, b and c are of greater significance. They are, in essence, the shadow cast by the entire 3-D confidence envelope onto the 2-D planes containing pairs of the three model parameters. They approximate the full confidence envelopes on the optimum solution. Axis-parallel tangents to these “shadow” ellipses (dashed lines) establish the maximum range of parameter values that are consistent with the experimental data at the specified confidence limits. For example, in Fig. 5.4a, the larger ellipse shows the entire range of model values of  $A_{TVF}$  and  $B_{TVF}$  that are consistent with this dataset at the  $1 \sigma$  confidence level (Table 5).

The covariances between model parameters indicated by the small vs. large ellipses are strikingly different. For example, in Fig. 5.4c the small ellipse shows a negative correlation between  $A_{TVF}$  and  $T_0$  compared to the strong positive correlation indicated by the larger ellipse. This is because the smaller ellipses show the correlations that result when one parameter (e.g.  $B_{TVF}$ ) is held constant at the value of the optimal solution. Where one parameter is fixed, the range of acceptable values and correlations between the other model parameters are greatly restricted. Conversely, the larger ellipse shows the overall correlation between two parameters, whilst the third parameter is also allowed to vary. It is critical to realize that each pair of  $A_{TVF}$ - $T_0$  coordinates on the larger ellipse demands a unique and different value of  $B$  (Fig. 5.4a, c). Consequently, although the range of acceptable values of  $A_{TVF}$ : $B_{TVF}$ : $T_0$  is large, the parameter values cannot be combined arbitrarily.

#### 5.2.4. Model TVF functions

The range of values of  $A_{TVF}$ ,  $B_{TVF}$ , and  $T_0$  shown to be consistent with the experimental dataset (Fig. 5.2) may seem larger than reasonable at first glance (Fig. 5.4). The consequences of these results are shown in Fig. 5.5 as a family of model TVF curves (Eq. 2.9) calculated by using combinations of  $A_{TVF}$ ,  $B_{TVF}$  and  $T_0$  that lie on the  $1 \sigma$  confidence ellipsoid (Fig. 5.4, larger ellipses). The dashed lines show the limits of the distribution of TVF curves (Fig. 5.5)

generated by using combinations of model parameters  $A_{TVF}$ ,  $B_{TVF}$  and  $T_0$  from the  $1\sigma$  confidence limits (Fig. 5.4). Compared to the original data array and to the “best-fit” TVF

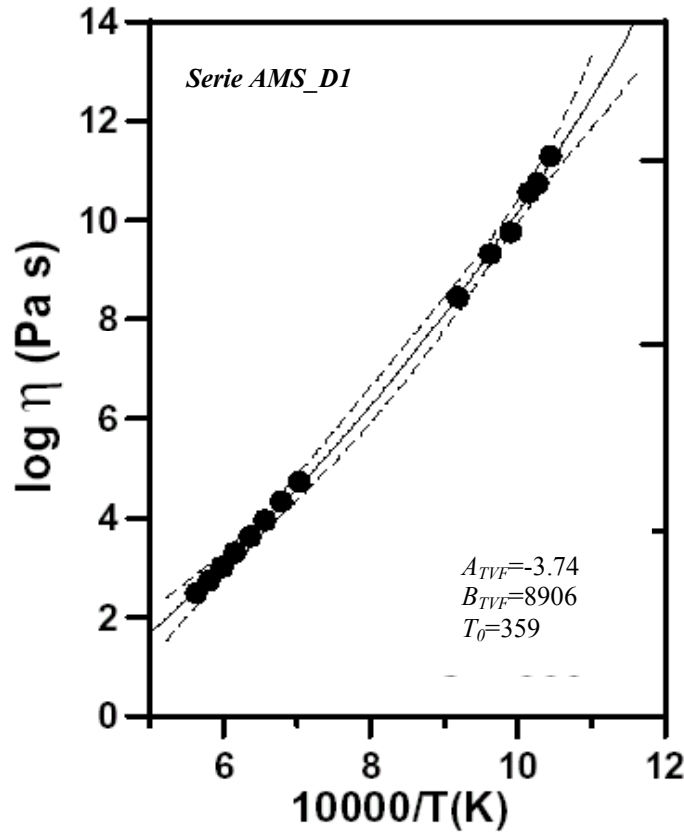


Fig. 5.5.: The optimal TVF function (solid line) and the distribution of TVF functions (dashed lines) permitted by the  $1\sigma$  confidence limits on  $A_{TVF}$ ,  $B_{TVF}$  and  $T_0$  (Fig. 5.4) are compared to the original experimental data of Fig. 5.2.

equation (Fig. 5.5, solid line), the family of TVF functions describe the original viscosity data well. Each one of these TVF functions must be considered an equally valid fit to the experimental data. In other words, the experimental data are permissive of a wide range of values of  $A_{TVF}$  (-0.8 to -6.8),  $B_{TVF}$  (3500 to 14,400) and  $T_0$  (100 to 625). However, the strong correlations between parameters (Table 5, Fig. 5.4) control how these values are combined. The consequence is that, even though a wide range of parameter values are considered, they generate a narrow band of TVF functions that are entirely consistent with the experimental data.

### 5.2.5. Data-induced covariances

The values, uncertainties and covariances of the TVF model parameters are also affected by the quality and distribution of the experimental data. This concept is following demonstrated using published data comprising 20 measurements of viscosity on a  $\text{Na}_2\text{O}$ -

enriched haplogranitic melt (Table 6 after Hess et al., 1995; Dorfman et al., 1996). The main attributes of this dataset are that the measurements span a wide range of viscosity ( $\approx 10 - 10^{11}$  Pa s) and the data are evenly spaced across this range (Fig. 5.6). The data were produced by three different experimental methods, including: concentric cylinder, micropenetration, and centrifuge-assisted falling-sphere viscometry (Table 6, Fig. 5.6). The latter experiments represent a relatively new experimental technique (Dorfman et al., 1996) that has made the measurement of melt viscosity at intermediate temperatures experimentally accessible.

The intent of this work is to show the effects of data distribution on parameter estimation. Thus, the data (Table 6) have been subdivided into three subsets; each dataset contains data produced by two of the three experimental methods. A fourth dataset comprises all of the data. The TVF equation has been fit to each dataset and the results are listed in Table 7. Overall, there little variation in the estimated values of model parameters  $A_{TVF}$  (-2.35 to -2.85),  $B_{TVF}$  (4060 to 4784) and  $T_0$  (429 to 484).

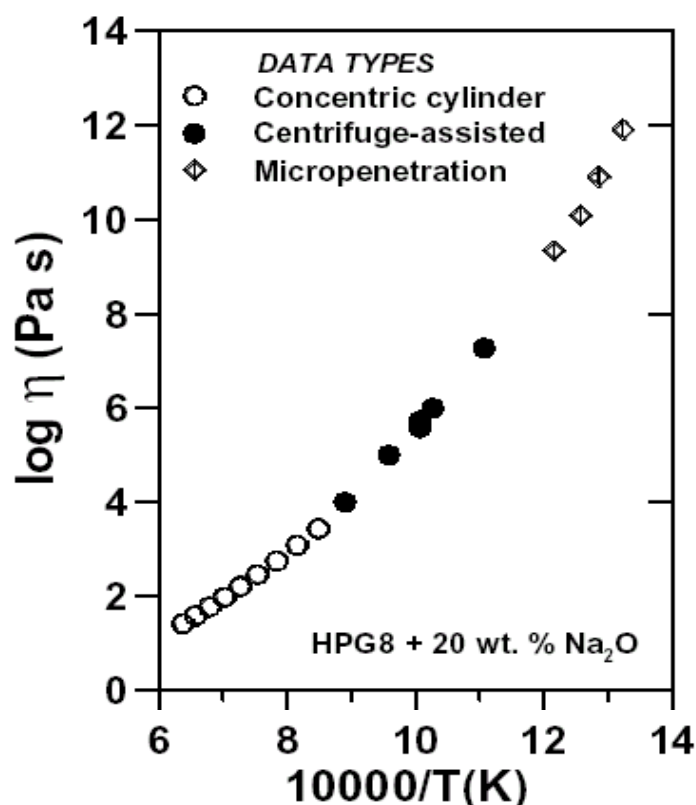


Fig. 5.6. : Viscosity data for a single composition of Na-rich haplogranitic melt (Table 6) are plotted against reciprocal temperature. Data derive from a variety of experimental methods including: concentric cylinder, micropenetration, and centrifuge-assisted falling-sphere viscometry (Hess et al., 1995; Dorfman et al., 1996).

### 5.2.6. Variance in model parameters

The 2-D projections of the  $1\sigma$  confidence envelopes computed for each dataset are shown in Fig. 5.7. Although the parameter values change only slightly between datasets, the nature of the covariances between model parameters varies substantially. Firstly, the sizes of

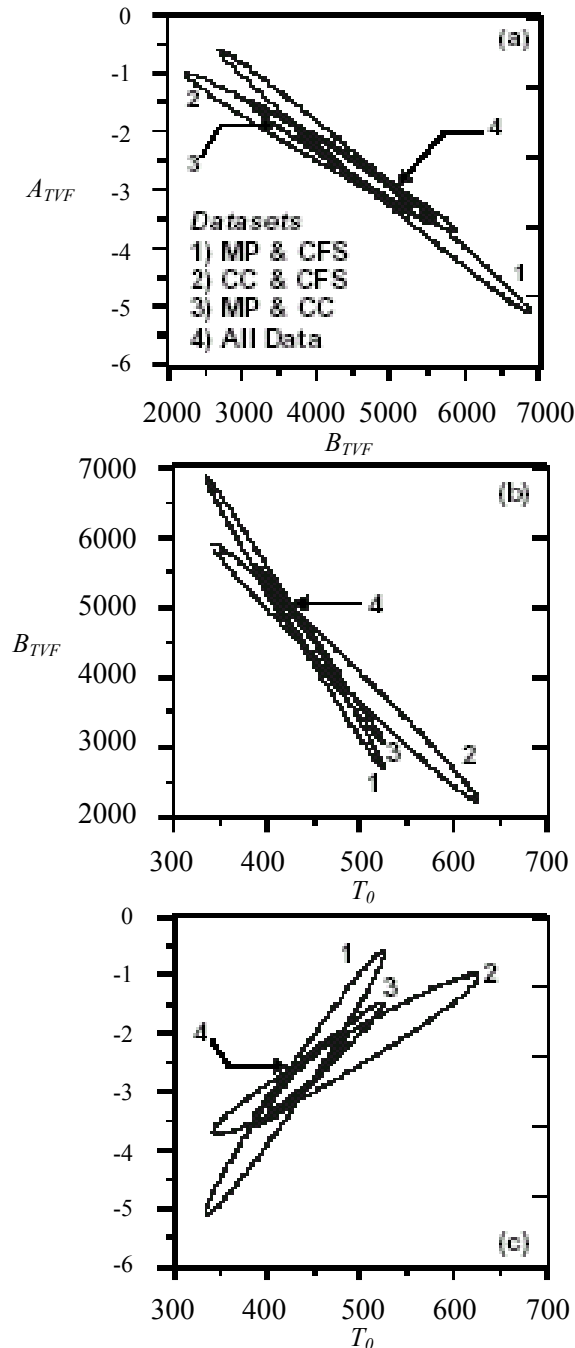


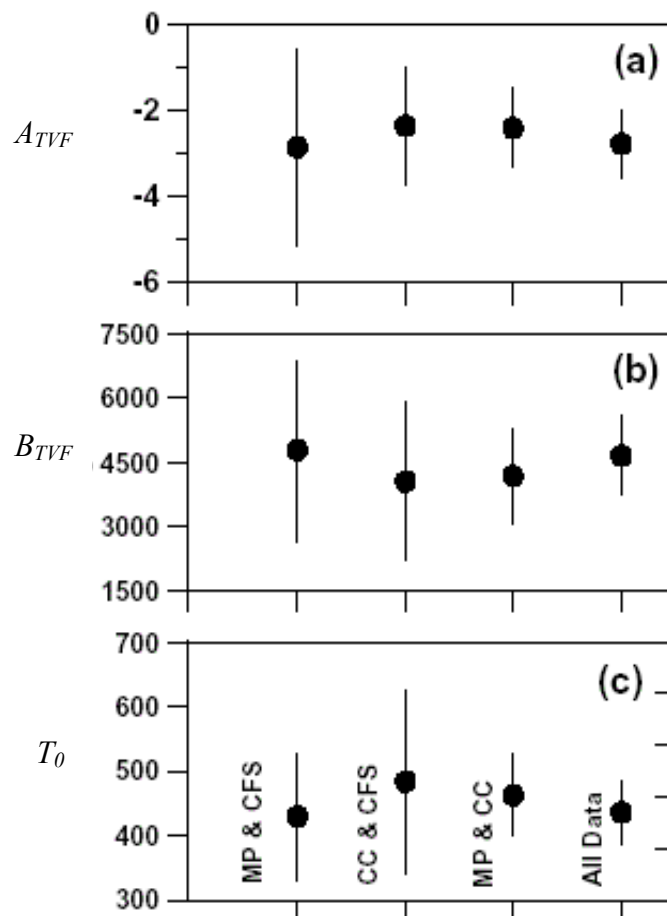
Fig. 5.7.: Subsets of experimental data from Table 6 and Fig. 5.6 have been fitted to the TVF equation and the individual solutions are represented by  $1\sigma$  confidence envelopes projected onto: a) the  $A_{TVF}$ - $B_{TVF}$  plane, b) the  $B_{TVF}$ - $T_0$  plane, and c) the  $A_{TVF}$ - $T_0$  plane. The 2-D projections of the confidence ellipses vary in size and orientation depending of the distribution of experimental data in the individual subsets (see text).

the ellipses vary between datasets. Axis-parallel tangents to these “shadow” ellipses approximate the ranges of  $A_{TVF}$ ,  $B_{TVF}$  and  $T_0$  that are supported by the data at the specified confidence limits (Table 7 and Fig. 5.8). As would be expected, the dataset containing all the available experimental data (No. 4) generates the smallest projected ellipse and, thus, the smallest range of  $A_{TVF}$ ,  $B_{TVF}$  and  $T_0$  values.

Clearly, more data spread evenly over the widest range of temperatures has the greatest opportunity to restrict parameter values. The projected confidence limits for the other datasets show the impact of working with a dataset that lacks high-, or low-, or intermediate-temperature measurements.

In particular, if either the low-T or high-T data are removed, the confidence limits on all three parameters expand greatly (e.g. Figs. 5.7 and 5.8). The loss of high-T data (No. 1; Figs. 5.7, 5.8 and Table 7) increases the uncertainties on model values of  $A_{TVF}$ . Less anticipated is the corresponding increase in the uncertainty on  $B_{TVF}$ . The loss of low-T data (No. 2; Figs. 5.7, 5.8 and Table 7) causes increased uncertainty on  $A_{TVF}$  and  $B_{TVF}$  but less than for case No. 1.

Fig. 5.8.: Optimal values and  $1\sigma$  ranges of parameters (a)  $A_{TVF}$ , (b)  $B_{TVF}$ , and (c)  $T_0$  derived for each subset of data (Table 6, Fig. 5.6 and 5.7). The range of acceptable values varies substantially depending on distribution of experimental data.



However, the  $1\sigma$  confidence limits on the  $T_0$  parameter increase nearly 3-fold (350-600). The loss of the intermediate temperature data (e.g. CFS data in Fig. 5.7; No. 3 in Table 7) causes only a slight increase in permitted range of all parameters (Table 7; Fig. 5.8). In this regard, these data are less critical to constraining the values of the individual parameters.

### 5.2.7. Covariance in model parameters

The orientations of the 2-D projected ellipses shown in Fig. 5.7 are indicative of the covariance between model parameters over the entire solution space. The ellipse orientations

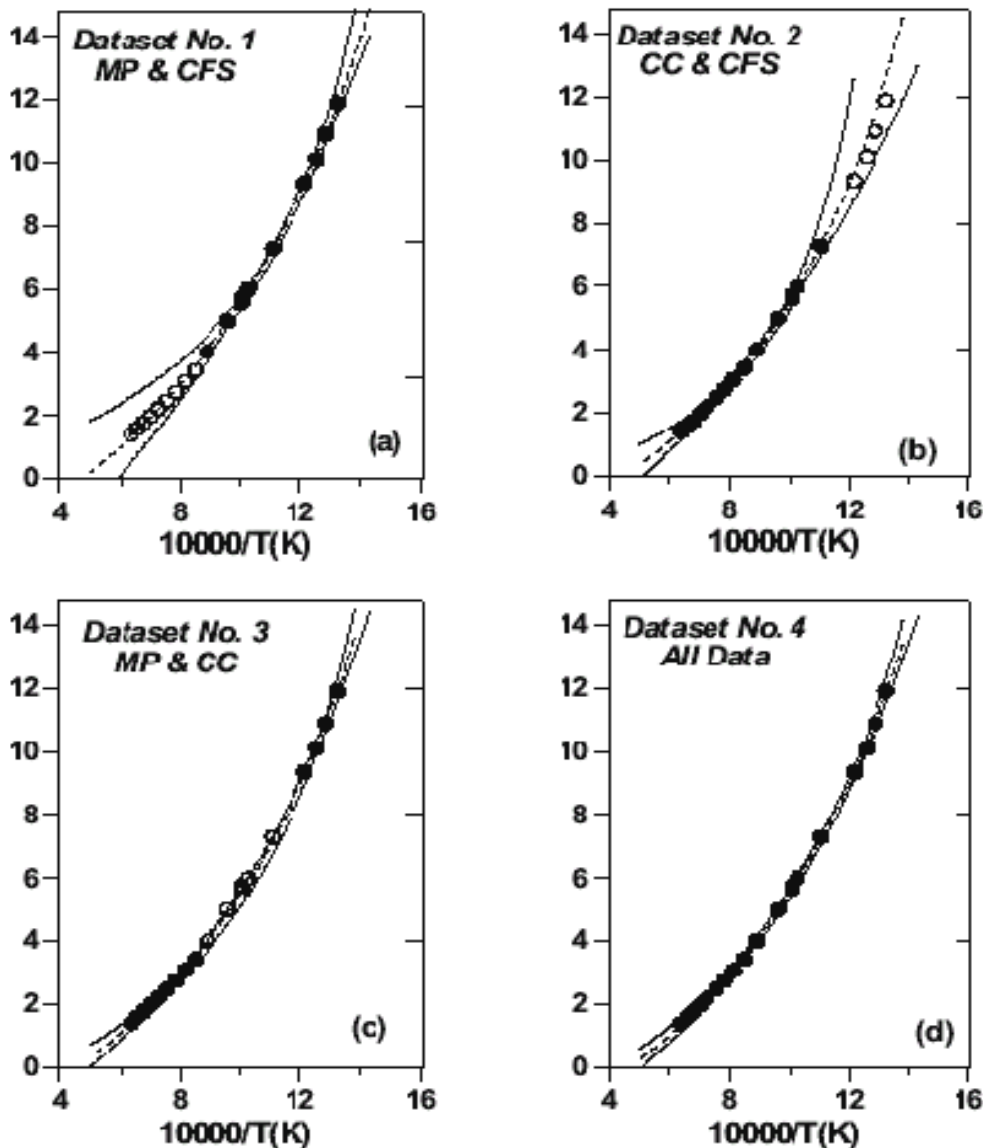


Fig. 5.9.: The optimal TVF function (dashed lines) and the family of TVF functions (solid lines) computed from  $1\sigma$  confidence limits on  $A_{TVF}$ ,  $B_{TVF}$  and  $T_0$  (Fig. 5.7 and Table 7) are compared to subsets of experimental data (solid symbols), including: a) MP and CFS, b) CC and CFS, c) MP and CC, and d) all data. Open circles denote data not used in fitting.

for the four datasets vary, indicating that the covariances between model parameters can be affected by the quality or the distribution of the experimental data.

The 2-D projected confidence envelopes for the solution based on the entire experimental dataset (No. 4; Table 7) show strong correlations between model parameters (heavy line; Fig. 5.7). The strongest correlation is between  $A_{TVF}$  and  $B_{TVF}$  and the weakest is between  $A_{TVF}$  and  $T_0$ . Dropping the intermediate-temperature data (No. 3; Table 7) has virtually no effect on the covariances between model parameters; essentially the ellipses differ slightly in size but maintain a single orientation (Fig. 5.7a, b, c). The exclusion of the low-T (No. 2) or high-T (No. 1) data causes similar but opposite effects on the covariances between model parameters. Dropping the high-T data sets mainly increases the range of acceptable values of  $A_{TVF}$  and  $B_{TVF}$  (Table 7) but appears to slightly weaken the correlations between parameters (relative to case No. 4).

If the low-T data are excluded, the confidence limits on  $B_{TVF}$  and  $T_0$  increase and the covariance between  $B_{TVF}$  and  $T_0$ , and  $A_{TVF}$  and  $T_0$  are slightly stronger.

### 5.2.8. Model TVF functions

The implications of these results (Fig. 5.7 and 5.8) are summarized in Fig. 5.9. As discussed above, families of TVF functions that are consistent with the computed confidence limits on  $A_{TVF}$ ,  $B_{TVF}$  and  $T_0$  (Fig. 5.7) for each dataset, were calculated. The limits to the family of TVF curves are shown as two curves (solid lines) (Fig. 5.9) denoting the  $1\sigma$  confidence limits on the model function. The dashed line is the optimal TVF function obtained for each subset of data. The distribution of model curves reproduces the data well but the capacity to extrapolate beyond the limits of the dataset varies substantially.

The  $1\sigma$  confidence limits calculated for the entire dataset (No. 4; Fig. 5.9d) are very narrow; over the entire temperature distribution of the measurements, the width of confidence limits is less than 1 log unit of viscosity. The complete dataset severely restricts the range of values for  $A_{TVF}$ ,  $B_{TVF}$  and  $T_0$  and, therefore, produces a narrow band of model TVF functions which can be extrapolated beyond the limits of the dataset.

Excluding either the low-T or high-T subsets of data causes a marked increase in the width of confidence limits (Fig. 5.9a, b). The loss of the high-T data requires substantial expansion (1-2 log units) in the confidence limits on the TVF function at high temperatures (Fig. 5.9a). Conversely, for datasets lacking low-T measurements, the confidence limits to the low-T portion of the TVF curve increase to between 1 and 2 log units (Fig. 5.9b). In either case, the capacity for extrapolating the TVF function beyond the limits of the dataset is

substantially reduced. Exclusion of the intermediate temperature data causes only a slight increase (10 - 20 %) in the confidence limits over the middle of the dataset.

### 5.2.9. Strong vs. fragile melts

Models for predicting silicate melt viscosities in natural systems must accommodate melts that exhibit varying degrees of non-Arrhenian temperature dependence. Therefore, final analysis involves fitting of two datasets representative of a strong, near Arrhenian melt and a more fragile, non-Arrhenian melt: albite and diopside, respectively.

The limiting values on these parameters, derived from the confidence ellipsoid (Fig. 5.10 c,d), are quite restrictive (Table 8) and the resulting distribution of TVF functions can be extrapolated beyond the limits of the data (Fig. 5.10; dashed lines).

The experimental data derive from the literature (Table 8) and were selected to provide a similar number of experiments, over a similar range of viscosities, and with approximately equivalent experimental uncertainties.

A similar fitting procedures as described above and the results are summarized in Table 8 and Figure 5.10 have been followed. The optimal TVF parameters for diopside melt based on these 53 data points are:  $A_{TVF} = -4.66$ ,  $B_{TVF} = 4,514$ , and  $T_0 = 718$  (Table 8; Fig. 5.10a, b, solid line).

Fitting the TVF function to the albite melt data produces a substantially different outcome. The optimal parameters ( $A_{TVF} = -6.46$ ,  $B_{TVF} = 14,816$ , and  $T_0 = 288$ ) describe the data well (Fig. 5.10a, b) but the  $1\sigma$  range of model values that are consistent with the dataset is huge (Table 8; Fig. 5.10c, d). Indeed, the range of acceptable parameter values for the albite melt is 5-10 times greater than the range of values estimated for diopside. Part of the solution space enclosed by the  $1\sigma$  confidence limits includes values that are unrealistic (e.g.  $T_0 < 0$ ) and these can be ignored. However, even excluding these solutions the range of values is substantial ( $-2.8 < A_{TVF} < -10.5$ ;  $7,240 < B_{TVF} < 27,500$ ; and  $0 < T_0 < 620$ ). However, the strong covariance between parameters results in a narrow distribution of acceptable TVF functions (Fig. 5.10b, dashed lines). Extrapolation of the TVF model past the data limits for the albite dataset has an inherently greater uncertainty than seen in the diopside dataset.

The differences found in fitting the TVF function to the viscosity data for diopside *versus* albite melts is a direct result of the properties of these two melts. Diopside melt shows pronounced non-Arrhenian properties and, therefore, requires all three adjustable parameters ( $A_{TVF}$ ,  $B_{TVF}$  and  $T_0$ ) to describe its rheology. The albite melt is nearly Arrhenian in behaviour, defines a linear trend in  $\log [\eta] - 10000/T(K)$  space, and is adequately described by only two

adjustable parameters. In applying the TVF function there is an extra degree of freedom, which allows for a greater range of parameter values to be considered. For example, the present solution for the albite dataset (Table 8) includes both the optimal ‘‘Arrhenian’’ solutions (where  $T_0 = 0$ ; Fig. 5.10c,d), as well as, solutions where the combinations of  $A_{TVF}$ ,  $B_{TVF}$  and  $T_0$  values generate a nearly Arrhenian trend. The near-Arrhenian behaviour of albite is only reproduced by the TVF model function over the range of experimental data (Fig. 5.10b). The non-Arrhenian character of the model and the attendant uncertainties increase when the function is extrapolated past the limits of the data.

These results have implications for modelling the compositional dependence of viscosity. Non-Arrhenian melts will tend to place tighter constraints on how composition is

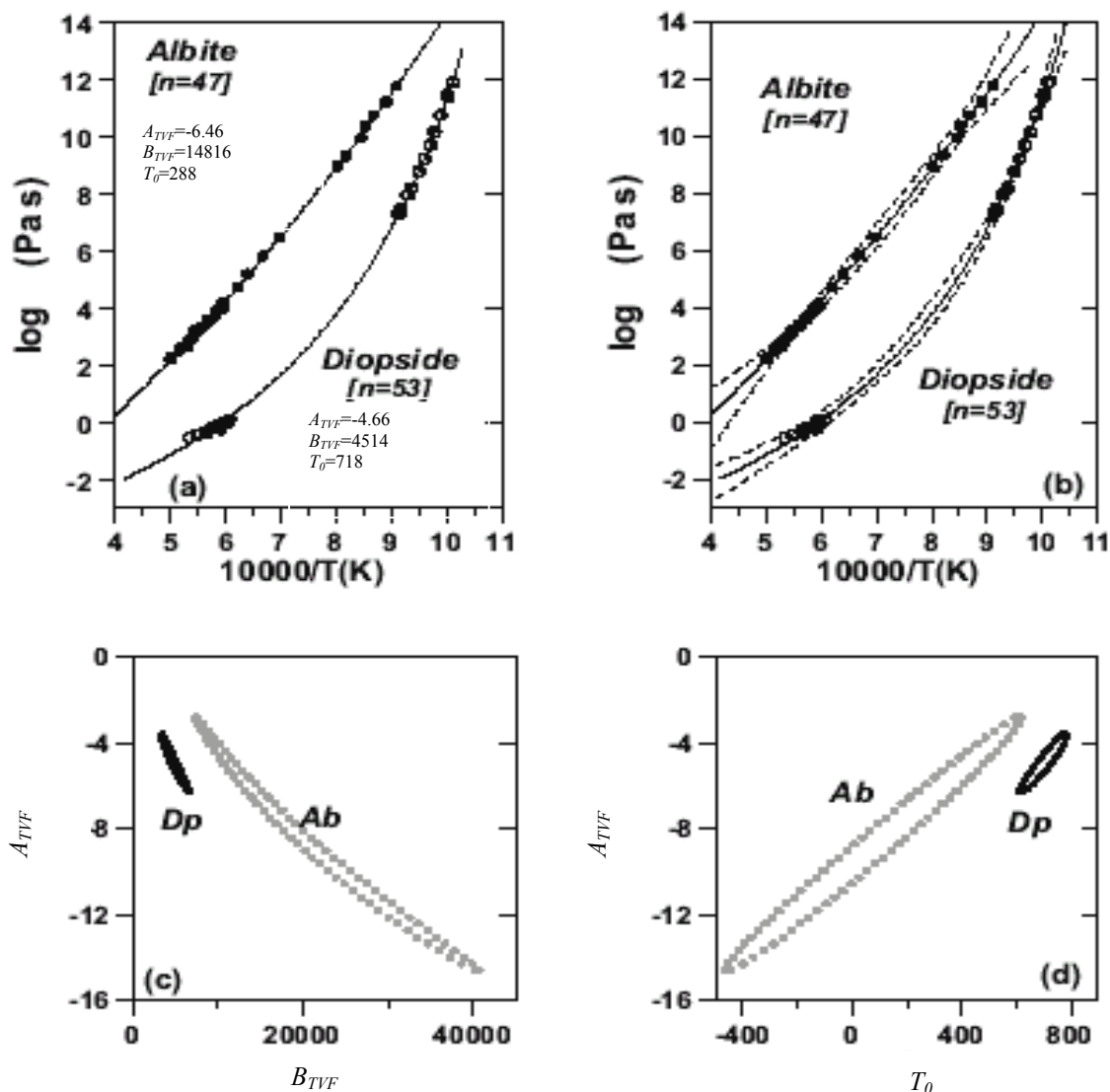


Fig. 5.10.: Summary of TVF models used to describe experimental data on viscosities of albite (Ab) and diopside (Dp) melts (see Table 8). (a) Experimental data plotted as  $\log [\eta]$  (Pa s) vs.  $10000/T(K)$  and compared to optimal TVF functions. (b) The family of acceptable TVF model curves (dashed lines) are compared to the experimental data. (c, d) Approximate  $1 \sigma$  confidence limits projected onto the  $A_{TVF}$ - $B_{TVF}$  and  $A_{TVF}$ - $T_0$  planes. Fitting of the TVF function to the albite data results in a substantially wider range of parameter values than permitted by the diopside dataset. The albite melts show Arrhenian-like behaviour which, relative to the TVF function, implies an extra degree of freedom.

partitioned across the model parameters  $A_{TVF}$ ,  $B_{TVF}$  and  $T_0$ . This is because melts that show near Arrhenian properties can accommodate a wider range of parameter values. It is also possible that the high-temperature limiting behaviour of silicate melts can be treated as a constant, in which case, the parameter  $A$  need not have a compositional dependence. Comparing the model results for diopside and albite, it is clear that any value of  $A_{TVF}$  used to model the viscosity of diopside can also be applied to the albite melts if an appropriate value of  $B_{TVF}$  and  $T_0$  are chosen. The Arrhenian-like melt (albite) has little leverage on the exact value of  $A_{TVF}$ , whereas the non-Arrhenian melt requires a restricted range of values for  $A_{TVF}$ .

### 5.2.10. Discussion

Developing a predictive model for the viscosity of natural silicate melts requires an understanding of how to partition the effects of composition across a non-Arrhenian model. At present, there is no definitive theory that establishes how parameters in non-Arrhenian equation (e.g.  $A_{TVF}$ ,  $B_{TVF}$ ,  $T_0$ ) should vary with composition. Furthermore, these parameters are not expected to be equally dependent on composition and definitely should not have the same functional dependence on composition. In the short-term, the decisions governing how to expand the non-Arrhenian parameters in terms of compositional effects will probably derive from empirical study.

During the search for empirical relationships between the model parameters and composition, it is important to realize that the optimal parameter values (e.g. least squares solution) do not necessarily convey the entire story. The non-linear character of the non-Arrhenian models ensures strong numerical correlations between model parameters that mask the effects of composition. One result of the strong covariances between model parameters is that wide ranges of values ( $A_{TVF}$ ,  $B_{TVF}$  or  $T_0$ ) can be used to describe individual datasets. This is true even where the data are numerous, well-measured, and span a wide range of temperatures and viscosities. Stated another way, there is a substantial range of model values which, when combined in a non-arbitrary way, can accurately reproduce the experimental data.

This concept should be exploited to simplify development of a composition-dependent, non-Arrhenian model for multicomponent silicate melts. For example, it may be possible to impose a single value on the high-T limiting value of  $\log [\eta]$  (e.g.  $A_{TVF}$ ) for some systems. The corollary to this would be the assignment of all compositional effects to the parameters  $B_{TVF}$  and  $T_0$ . Furthermore, it appears that non-Arrhenian datasets have the greatest leverage on compositional dependencies. Strong liquids that exhibit near Arrhenian behaviour place only

minor restrictions on the absolute ranges of values of  $A_{TVF}$ ,  $B_{TVF}$  and  $T_0$ . Therefore, strategies for modelling the effects of composition should be built around high quality datasets collected on non-Arrhenian melts.

### **5.3. Predicting the “kinetic” fragility of natural silicate melts: constraints using Tammann-Vogel–Fulcher equation**

The newtonian viscosities of multicomponent liquids, that range in composition from basanite through phonolite and trachyte, to dacite (see, § 3), have been investigated by using the techniques discussed in § 3.2.1 and 3.2.3 at ambient pressure. For each silicate liquid (compositional details are provided in chapter 4 and Table 1) regression of the experimentally determined viscosities allowed  $A_{TVF}$ ,  $B_{TVF}$  and  $T_0$  to be calibrated according to the TVF equation (Eq. 2.9). The results of this calibration provide the basis for the following analyses and allow qualitative and quantitative correlations to be made between the TVF coefficients that are commonly used to describe the rheological and physico-chemical properties of silicate liquids. The  $B_{TVF}$  and  $T_0$  values, calibrated via Eq. 2.9, are highly correlated. Fragility ( $F$ ) is correlated with the TVF temperature, which allows the fragility of the liquids to be compared at the calibrated  $T_0$  values.

The viscosity data are listed in Table 3 and shown in Fig. 5.1. As well as measurements performed during this study on natural samples, they include data from synthetic materials by Whittington et al. (2000, 2001). Two synthetic compositions, HPG8, a haplo-granitic composition (Hess et al., 1995) and N\_An, a haplo-andesitic composition (Neuville et al., 1993), have been included. The compositions of the investigated samples are shown in Fig. 4.1.

#### **5.3.1. Results**

High and low temperature viscosities versus the reciprocal temperature are presented in Fig. 5.1. The viscosities exhibited by different natural compositions or natural-equivalent compositions differ by 6-7 orders of magnitude at a given temperature. The viscosity values (Tab. 3) vary from slightly to strongly non-Arrhenian over the range of  $10^{-1}$  to  $10^{11.6}$  Pa·s. A comparison between the viscosity calculated using Eq. 2.9 and the measured viscosity is provided in Fig. 5.11 for all the investigated samples. The TVF equation closely reproduces the viscosity of silicate liquids.

The  $T_0$  and  $B_{TVF}$  values for each investigated sample are shown in Fig. 5.12. As  $T_0$  increases  $B_{TVF}$  decreases. Undersaturated liquids such as the basanite from Eifel (EIF), the tephrite (W\_Teph) (Whittington et al., 2000), the basalt from Etna (ETN) and the synthetic tephrite (NIQ) (Whittington et al., 2000) have higher TVF temperatures  $T_0$  and lower pseudo-activation energies  $B_{TVF}$ . On the contrary, SiO<sub>2</sub>-rich samples for example the Povocao trachyte and the HPG8 haplogranite, have higher pseudo-activation energies and much lower  $T_0$ .

There is a linear relationship between “kinetic” fragility ( $F$ , section 2.1.3) and  $T_0$  for all the investigated silicate liquids (Fig. 5.13). This is due to the relatively small variation between glass transition temperatures ( $1000\text{K} \pm 10\%$ ) calculated for each composition (Fig.

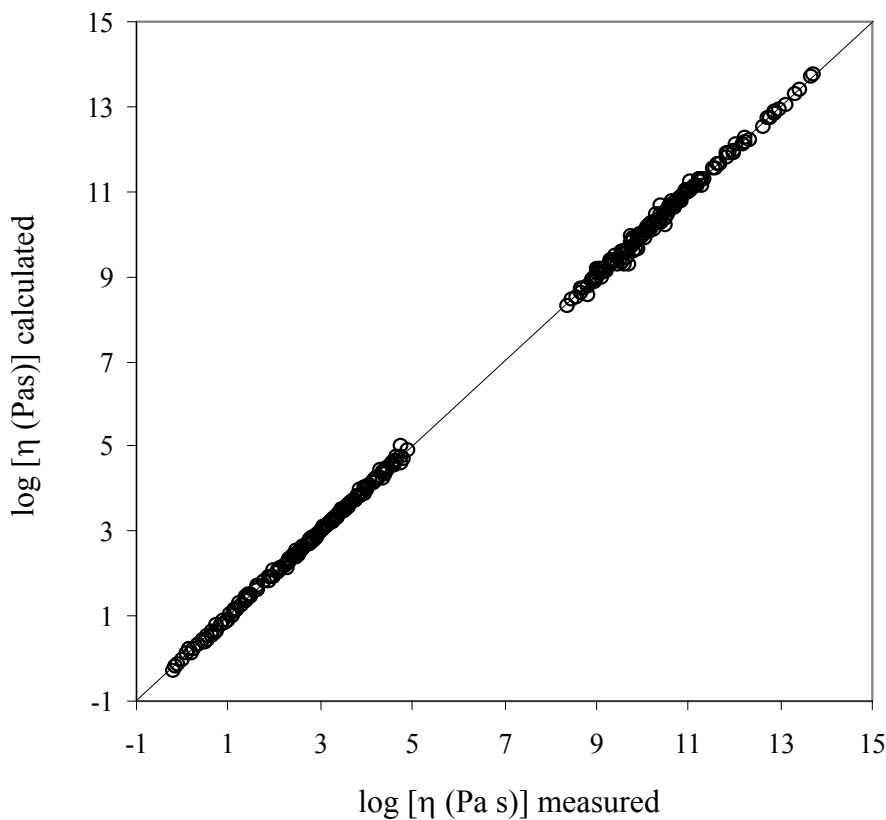


Fig. 5. 11.: Comparison between the measured and the calculated data (Eq. 2.9) for all the investigated liquids.

5.14). The exception are the strongly polymerised samples HPG8 (Hess and Dingwell, 1996) and SiO<sub>2</sub> (occasionally included in the diagram as the extreme term of comparison; Richet, 1984) that have higher  $T_g$ . Also Diopside is included in Fig. 5.14 and 5.15 as extreme case of depolymerization. Contrary to  $T_g$  values,  $T_0$  values vary widely. Kinetic fragilities  $F$  and TVF temperatures  $T_0$  increase as the structure becomes increasingly depolymerised (NBO/T increases) (Figs. 5.13/5.15). Consequently low  $F$  values correspond to high  $B_{TVF}$  and low  $T_0$  values.  $T_0$  values varying from 0 to about 700 K correspond to  $F$  values between 0 and about

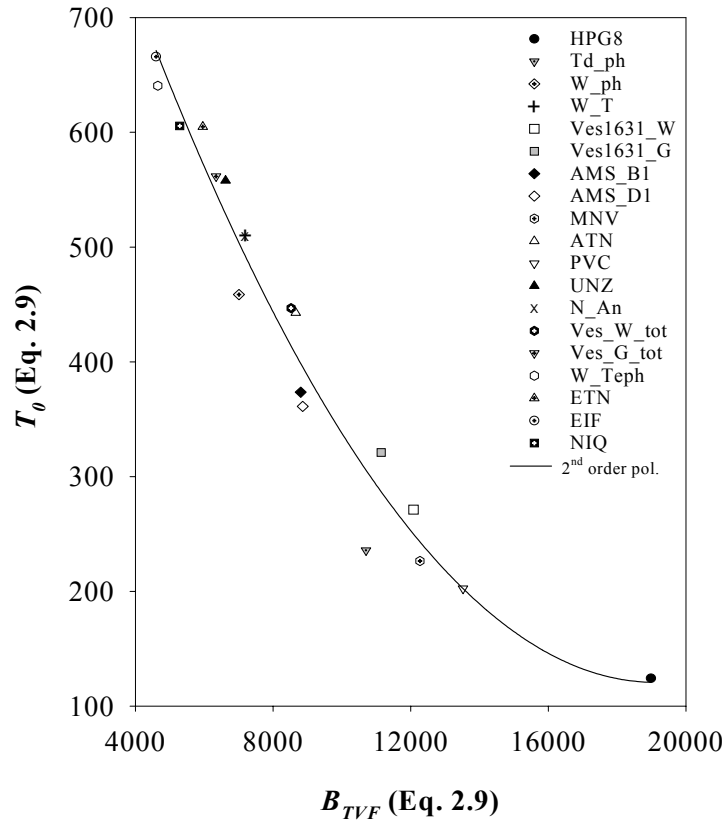


Fig. 5.12.: Calibrated Tammann-Vogel Fulcher temperatures ( $T_0$ ) versus the pseudo-activation energies ( $B_{TVF}$ ) calibrated using equation 2.9. The curve represents the best-fit second-order polynomial which expresses the correlation between  $T_0$  and  $B_{TVF}$  (Eq. 5.2).

0.7. There is a sharp increase in fragility with increasing NBO/T ratios up to ratio of 0.4-0.5. In the most depolymerized liquids with higher NBO/T ratios, (NIQ, ETN, EIF, W\_Teph) (Diopside was also included as most depolymerised sample Table 4) fragility assumes an almost constant value (0.6-0.7). Such high fragility values are similar to those shown by molecular glass-formers, such as, the orthoterphenyl (OTP)(Dixon and Nagel, 1988) which is one of the most fragile organic liquids.

An empirical equation (represented by a solid line in Fig. 5.15) enables the fragility of all the investigated liquids, to be predicted, as a function of the degree of polymerization:

$$F = -0.0044 + 0.6887 * [1 - \exp(-5.4767 * \text{NBO}/T)] \quad (5.2)$$

This equation reproduces  $F$  within a maximum residual error of 0.13 for silicate liquids ranging from very strong to very fragile (see Table 4). Calculations using Eq. 5.2 are more accurate for fragile rather than strong liquids (Table 4).

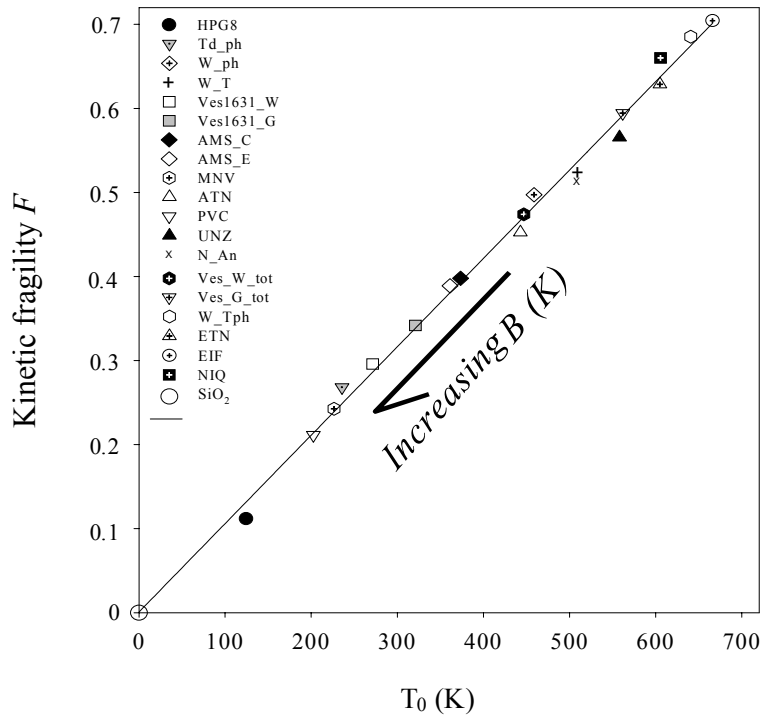


Fig. 5.13.: The relationship between fragility ( $F$ ) and the TVF temperature ( $T_0$ ) for all the investigated samples.  $\text{SiO}_2$  is also included for comparison. Pseudo-activation energies increase with decreasing  $T_0$  (as indicated by the arrow). The line is a best-fit equation through the data.

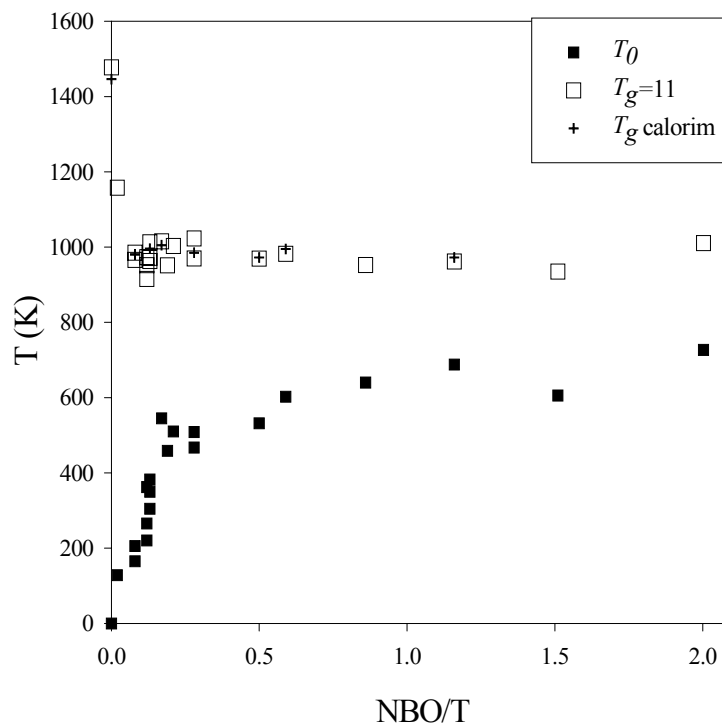


Fig. 5.14: The relationships between the TVF temperature ( $T_0$ ), and NBO/T and glass transition temperatures ( $T_g$ ) and NBO/T.  $T_g$  defined in two ways are compared.  $T_g = T_{11}$  indicates  $T_g$  is defined as the temperature of the system where the viscosity is of  $10^{11}$  Pas. The “calorim  $T_g$ ” refers to the calorimetric definition of  $T_g$  in section 5.5.  $T_0$  increases with the addition of network modifiers. The two most polymerised liquids have high  $T_g$ . Melt with NBO/T ratio  $> 0.4-0.5$  show the variation in  $T_g$ . Viscosimetric and calorimetric  $T_g$  are consistent.

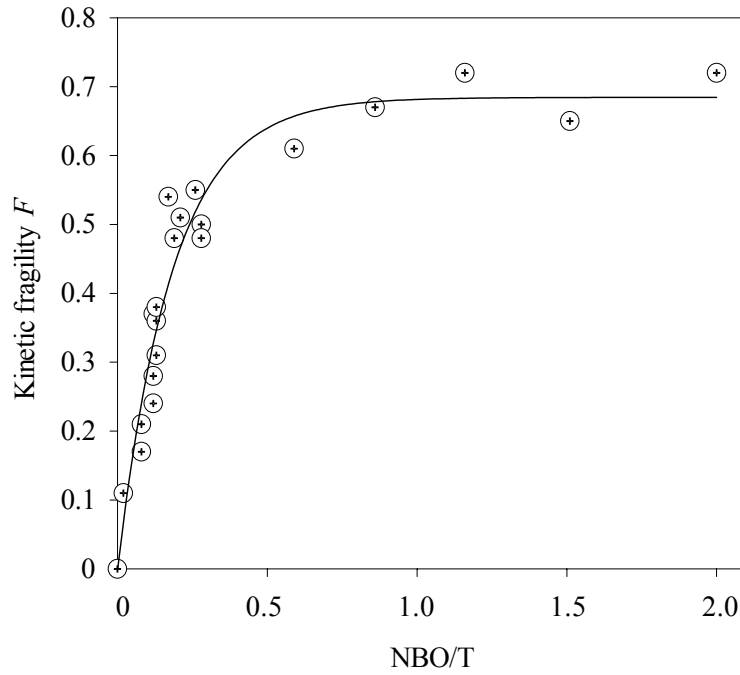


Fig. 5.15.: The relationship between the fragilities ( $F$ ) and the NBO/T ratios of the investigated samples. The curve in the figure is calculated using Eq. 5.2.

### 5.3.2. Discussion

The dependence of  $T_g$ ,  $T_0$  and  $F$  on composition, for all the investigated silicate liquids, are shown in Figs. 5.14 and 5.15.  $T_g$  slightly decreases with decreasing polymerisation (Table 4). The two most polymerised liquids,  $\text{SiO}_2$  and HPG8, show significant deviation from the trend which much higher  $T_g$  values. This underlines the complexity of describing Arrhenian vs. non-Arrhenian rheological behaviour for silicate melts via the TVF equation equations (section 5.2).

An empirical equation, which allows the fragility of silicate melts to be calculated is provided (Eq. 5.2). This equation is the first attempt to find a relationship between the deviation from Arrhenian behaviour of silicate melts (expressed by the fragility, section 2.1.3) and a compositional structure-related parameter, such as the NBO/T ratio.

The addition of network modifying elements (expressed by increasing of the NBO/T ratio) has an interesting effect. Initial addition of such elements to a fully polymerised melt (e.g.  $\text{SiO}_2$ , NBO/T = 0) results in a sharp increase in  $F$  (Fig. 5.15). However, at NBO/T values above 0.4-0.5 further addition of network modifier has little effect on fragility. Because fragility quantifies the deviation from an Arrhenian-like rheological behaviour, this effect has to be interpreted as a variation in the configurational rearrangements and rheological regimes of the silicate liquids due to the addition of structure modifier elements. This is likely related to changes in the size of the molecular clusters (termed cooperative

rearrangements in the Adam and Gibbs theory, 1965), which constitute silicate liquids. Using simple systems Toplis (1998) presented a correlation between the size of the cooperative rearrangements and NBO/T on the basis of some structural considerations. A similar approach could also be attempted for multicomponent melts. However, a much more complex computational strategy will be needed requiring further investigations.

#### **5.4. Towards a Non-Arrhenian multi-component model for the viscosity of magmatic melts**

The Newtonian viscosities in section 5.2 can be used to develop an empirical model to calculate the viscosity of a wide range of silicate melt compositions. The liquid compositions are provided in chapter 4 and section 5.2.

Incorporated within this model is a method to simplify the description of the viscosity of Arrhenian and non-Arrhenian silicate liquids in terms of temperature and composition. A chemical parameter (SM), which is defined as the sum of mole percents of Ca, Mg, Mn, half of the total  $Fe_{tot}$ , Na and K oxides, is used. SM is considered to represent the total structure-modifying function played by cations to provide NBO (chapter 2) within the silicate liquid structure. The empirical parameterisation presented below uses the same data-processing method as was reported in § 5.2, where  $A_{TVF}$ ,  $B_{TVF}$  and  $T_0$  were calibrated for the TVF equation (Table 4).

The role played by the different cations within the structure of silicate melts can not be univocally defined, on the basis of previous studies, at all temperature, pressure and composition conditions. At pressure below a few kbars, alkalis and alkaline earths may be considered as “network modifiers”, while Si and Al, are tetrahedrally coordinated. However, the role of some of the cations (e.g. Fe, Ti, P and Mn) within the structure is still a matter for debate. Previous investigations and interpretations have been made on a case to case basis. They were discussed in chapter 2.

In the following analysis it is sufficient to infer a “network modifier” function (chapter 2) for the alkalis, alkaline earths, Mn and half of the total iron  $Fe_{tot}$ . As a result the chemical parameter (SM), the sum, on a molar basis, of the Na, K, Ca, Mg, Mn oxides and half of the total Fe oxides ( $Fe_{tot}/2$ ), is considered in the following discussion.

Viscosity results for pure  $SiO_2$  (Richet, 1984) are also taken into account to provide further comparison.  $SiO_2$  is an example of a strong-Arrhenian liquid (see definition in § 2.1.3) and constitutes an extreme case in terms of composition and rheological behaviour.

##### **5.4.1. The viscosity of dry silicate melts – compositional aspects.**

Previous numerical investigations (sections 5.2 and 5.3) suggest that some numerical correlation can be derived between the TVF parameters  $A_{TVF}$ ,  $B_{TVF}$  and  $T_0$  and some compositional factor. Numerous attempts were made (e.g. Persikov et al., 1990; Hess, 1996;

Russell et al., 2002) to establish the empirical correlations between these parameters and the composition of the silicate melts investigated. In order to identify an appropriate compositional factor, previous studies were analysed in which a particular role had been attributed to the ratio between the alkali and the alkaline earths (e.g. Bottinga and Weill, 1972), the contribution of excess alkali (§ 2.2.2.), the effect of SiO<sub>2</sub>, Al<sub>2</sub>O<sub>3</sub> or their sum, and the NBO/T ratio (Mysen, 1988).

Detailed studies of several simple chemical systems show the parameter values to have a non-linear dependence on composition (Cranmer & Uhlmann, 1981; Richet, 1984; Hess *et al.*, 1996; Toplis *et al.*, 1997; Toplis, 1998). Additionally, there are empirical data and a theoretical basis indicating that three parameters (e.g. the  $A_{TVF}$ ,  $B_{TVF}$  and  $T_0$  of the TVF equation (2.9)) are not equally dependent on composition (Richet & Bottinga, 1995; Hess *et al.*, 1996; Rossler *et al.*, 1998; Toplis *et al.*, 1997; Giordano *et al.* 2000).

An alternative approach was attempted to directly correlate the viscosity determinations (or their values calculated by the TVF equation 2.9) with composition. This approach implies comparing the isothermal viscosities with the compositional factors (e.g. NBO/T, the agpaitic index<sup>4</sup> (A.I.), the molar ratio alkali/alkaline earth) that had already been used in literature (e.g. Mysen, 1988; Stevenson et al., 1995; Whittington et al., 2001) to attempt to find correlations between the  $A_{TVF}$ ,  $B_{TVF}$  and  $T_0$  parameters.

Closer inspection of the calculated isothermal viscosities allowed a compositional factor to be derived. This factor was believed to represent the effect of the chemical composition on the structural arrangement of the silicate liquids.

The SM as well as the ratio NBO/T parameter was found to be proportional to the isothermal viscosities of all silicate melts investigated (Figs. 5. 16, 5.17). The dependence of SM from the NBO/T is shown in Fig. 5.18.

Figs. 5. 16 and 5.17 indicate that there is an evident correlation between the SM parameter and the NBO/T ratio with the isothermal viscosities and the isokom temperatures (temperatures at fixed viscosity value).

The correlation between the SM and NBO/T parameters with the isothermal viscosities is strongest at high temperature, it becomes less obvious at lower temperatures.

Minor discrepancies from the main trends are likely to be due to compositional effects which are not represented well by the SM parameter.

---

<sup>4</sup> The agpaitic Index (A.I) is the ratio the total alkali oxides and the aluminium oxide, expressed on a molar basis:  $A.I. = (Na_2O+K_2O)/Al_2O_3$ .

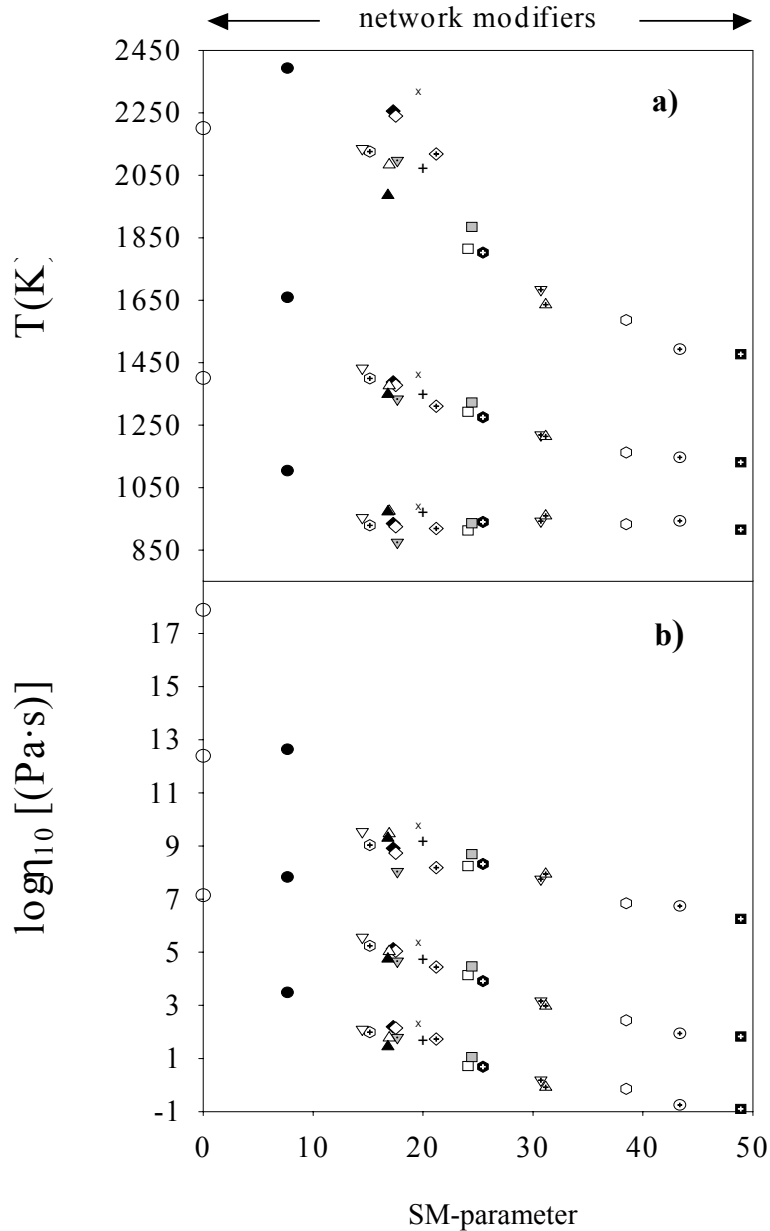


Fig. 5. 16.: (a) Calculated isokom temperatures and (b) the isothermal viscosities versus the SM parameter values expressed in mole percentages of the network modifiers (see text). (a) reports the temperatures at three different viscosity values (isokoms);  $\log\eta=1$  (highest curve), 5 (centre curve) and 12 (lowest curve). (b) shows the viscosity at constant temperatures corresponding to  $T=800^\circ C$  (highest curve),  $1100^\circ C$  and  $1600^\circ C$  (lowest curve). Symbols in the figures are the same as in Figs. 5. 10 to 5. 12. With pure  $SiO_2$  (Richet, 1984) any addition of network modifiers reduces the viscosity and isokom temperature. In (a) the calculated isokom temperature corresponding to  $\log\eta=1$  for pure silica ( $T=3266 K$ ) is not included as it falls beyond the reasonable extrapolation of the experimental data.

In spite of the above uncertainties Fig. 5.16 (a, b) shows that the initial addition of network modifiers to a starting composition, such as  $SiO_2$ , has a greater effect on reducing both viscosity and isokom temperature (Fig. 5.16 a, b) than any successive addition. Furthermore, the viscosity trends followed at different temperatures ( $800$ ,  $1100$  and  $1600^\circ C$ ) are nearly parallel (Fig. 5. 16 b). This suggests that the various cations occupy the same

structural roles at different temperatures. Fig. 5. 18 shows the relationship between NBO/T and SM. It shows a clear correlation between the parameter SM and ratio of non-bridging oxygen to structural tetrahedra (the NBO/T value).

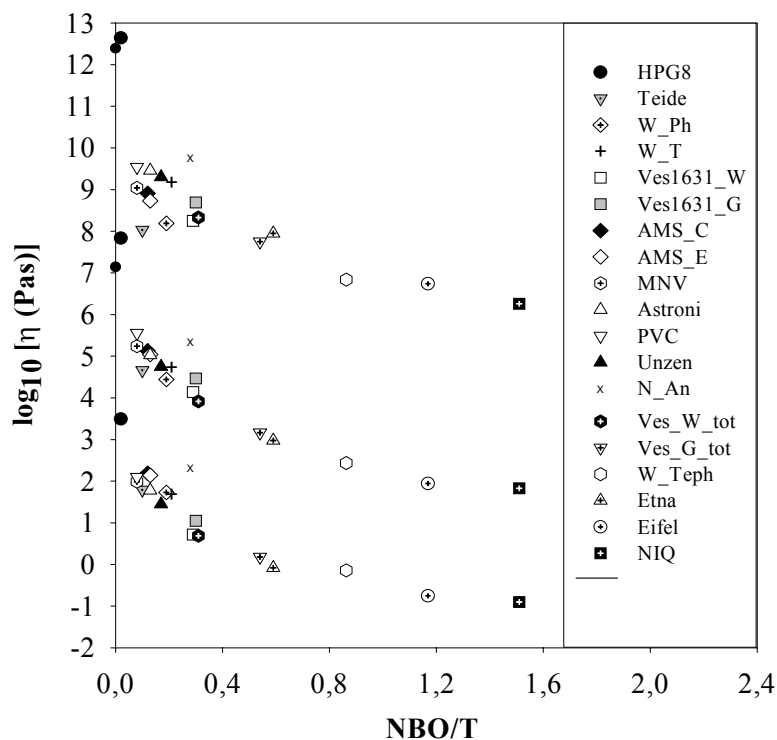


Fig. 5. 17.: Calculated isothermal viscosities versus the NBO/T ratio. Figure shows the viscosity at constant temperatures corresponding to  $T=800^\circ\text{C}$  (highest curve),  $1100^\circ\text{C}$  and  $1600^\circ\text{C}$  (lowest curve). Symbols in the figures are the same as in Figs. 5. 10 to 5. 12.

The correlation shown in Fig. 5.18 for the wide range of natural compositions investigated, indicates that the SM parameter contains an information on the structural arrangement of the silicate liquids, and confirms that the choice of cations defining the numerical value of SM is reasonable.

When defining the SM parameter, only half of the total iron ( $\text{Fe}_{\text{tot}}/2$ ) is regarded as a “network modifier”. Nevertheless this assumption does not significantly influence the relationships between the isothermal viscosities and the NBO/T and SM parameters. The contribution of iron to the SM parameter is not significantly affected by its oxidation state. The effect of phosphorous on the SM parameter is assumed negligible in this study as it is present in such a low concentrations in the samples analysed (Table 1).

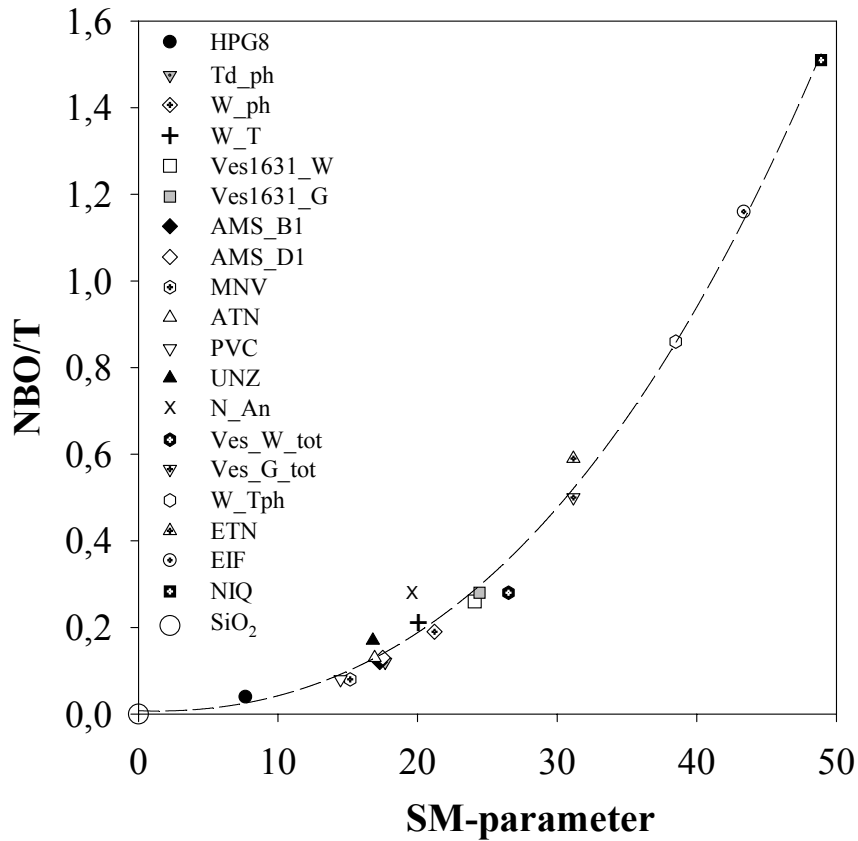


Fig. 5. 18.: The variation of the NBO/T ratio (§ 2.2.1) as a function of the SM parameter. The good correlation shows that the SM parameter is sufficient to describe silicate liquids with an accuracy comparable to that of NBO/T.

#### 5.4.2. Modelling the viscosity of dry silicate liquids - calculation procedure and results

The parameterisation of viscosity is provided by regression of viscosity values (determined by the TVF equation 2.9 calibrated for each different composition, as explained in the previous section 5.3) on the basis of an equation for viscosity at any constant temperature, which includes the SM parameter (Fig. 5. 16 b):

$$\log_{10}\eta=c_1+\frac{c_2*c_3}{c_3+SM} \quad (5.3)$$

where  $c_1$ ,  $c_2$  and  $c_3$  are the adjustable parameters at temperature  $T_i$ . SM is the independent variable previously defined in terms of mole percent of oxides (NBO/T was not used to provide a final model as it did not provide as good accurate recalculation as the SM parameter). TVF equation values instead of experimental data are used as their differences are very minor (Fig. 5.11) and because Eq. 2.9 results in a easier comparison also at conditions interpolated to the experimental data.

Ten different isothermal viscosity curves at steps of 100 °C from 700 to 1600 °C were fitted to obtain the  $c_1$ ,  $c_2$  and  $c_3$  parameters for Eq. 5.3. Interpolation at temperatures less than 700 °C was not performed because there were not a significant number of data-points at this temperature to permit a calibration. In fact only 5 of 20 datasets (Td\_ph, W\_ph, N\_An, W\_Tph and NIQ) have a significant amount of data at temperatures below 700 °C.

Thirty composition-dependent adjustable parameters were calibrated (3 for each isothermal viscosity curve) on the basis of the viscosity calculated using Eq. 2.9. Viscosities recalculated using these composition-dependent parameters (the  $c_1$ ,  $c_2$  and  $c_3$ ) at a given temperature are in good agreement with those calculated via the Tammann-Vogel-Fulcher parameterisation of Eq. 2.9 (which is in good accord with the measured viscosities). Table 9 shows such a comparison (through the residuals), while values for the adjustable parameters at each temperature are given in table 10. Analysis of the residuals shows discrepancies between the viscosities calculated using Eq. 5. 3 and those calculated using Eq. 2.9, which increase at lower temperatures (Table 9).

The dependence of the  $c_1$ ,  $c_2$  and  $c_3$  parameters on temperature was investigated in order to build up a viscosity model which predicts the viscosity of multi-component melts as a function of composition and temperature.

The parameters calculated by Eq. 5.3 show a clear, well defined trend with temperature (Fig. 5.19). Such trends are expressed by the following equations:

$$c_1 = (-17.80106 + 0.01808103 \cdot T) / (1 - 2.2869 \cdot 10^{-3} \cdot T) \quad (5.4)$$

$$c_2 = [0.02532 + 2.5124 \cdot \exp(-6.3679 \cdot 10^{-3} \cdot T) + 40.4562 \cdot 10^{-6} \cdot T]^{-1} \quad (5.5)$$

$$c_3 = (1 - 1.6569 \cdot 10^{-3} \cdot T) / (0.017954 - 63,90597 \cdot 10^{-6} \cdot T) \quad (5.6)$$

where T is the temperature (°C). The curves in Fig. 5.19 and the values in Table 10 show that the parameters calculated via Eqs. 5. 4/5.6 are in very good agreement ( $R^2 \sim 0.999$ ) with those obtained using Eq. 5.3 (symbols in the figures), which are at first just considered composition-dependent. This leads to a 10 parameter correlation for the viscosity of compositionally different silicate liquids. In other words it is possible to predict the viscosity of a silicate liquid on the basis of its composition, by using the 10-parameter correlation derived in this section.

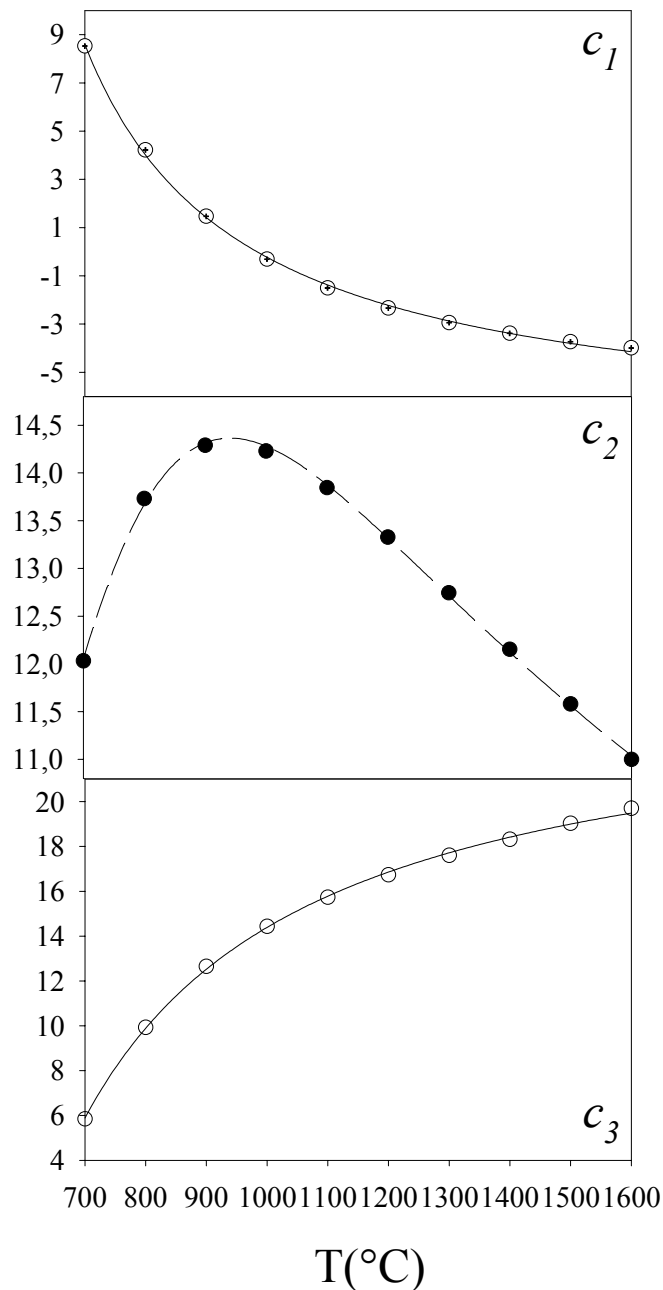


Fig. 5. 19.: It shows that the coefficients used to parameterise the viscosity as a function of composition (Eq. 5. 7) depend strongly on temperature, here expressed in  $^{\circ}\text{C}$ .

Fig. 5. 20 compares the viscosity calculated using Eq. 2.9 (which accurately represent the experimentally measured viscosities) with those calculated using Eqs. 5.4/5.6. Eqs. 5.3/5.6 predicts the measured viscosities well. However there are exceptions (e.g. the Teide phonolite, the peralkaline samples from Whittington et al. (2000, 2001) and the haploandesite from Neuville et al. (1993).

This is probably due to the fact that there are few samples in which the viscosity has been measured in the low temperature range. This results in a less accurate calibration that for the more abundant data at high temperature. Further experiments to investigate the viscosity

of the peralkaline and low alkaline samples in the low temperature range are required to further improve empirical and physical models to complete the description of the rheology of silicate liquids.

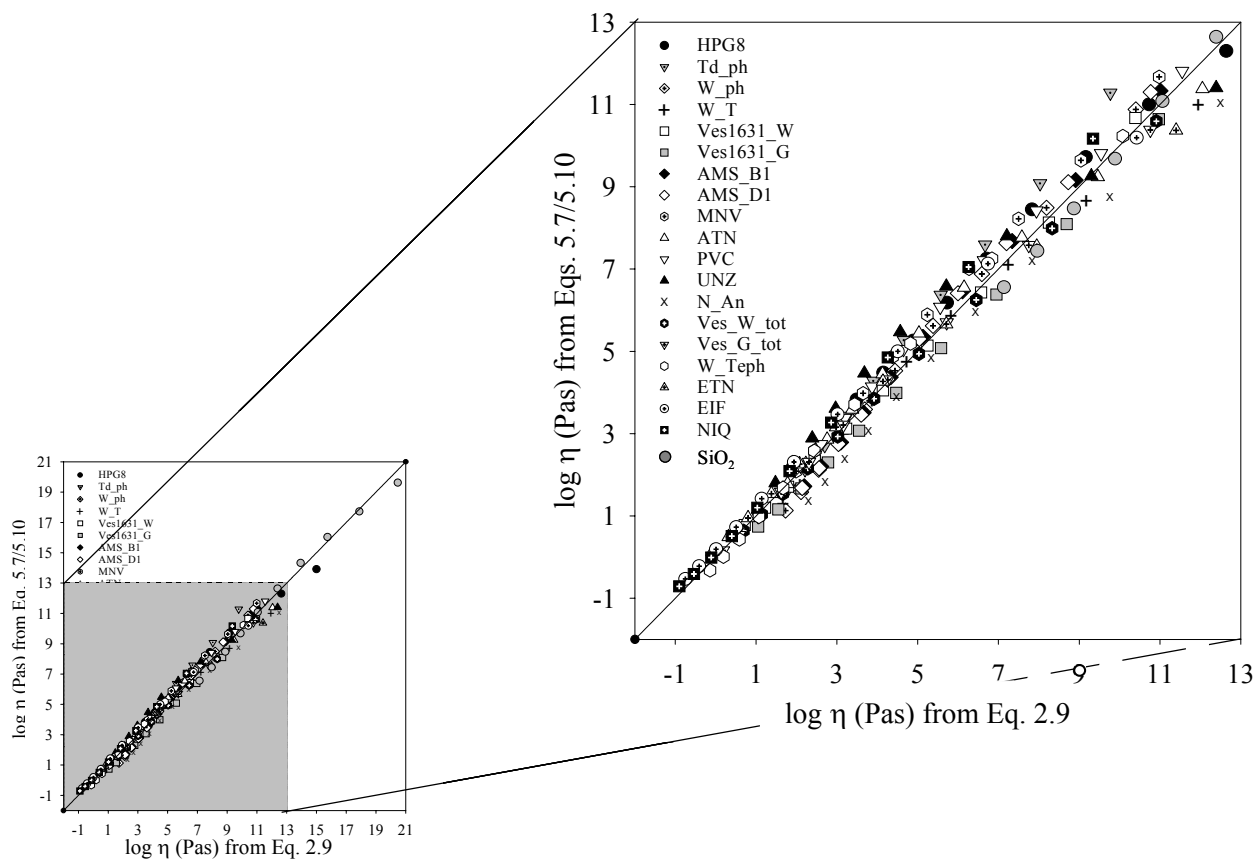


Fig. 5.20.: Comparison between the viscosities calculated using Eq. 2.9 (which reproduce the experimental determinations within  $R^2$  values of 0.999, see Fig. 5.11) and the viscosities modelled using Eqs. 5.7/5.10. The small picture reports all the values calculated in the interval 700 – 1600°C for all the investigated samples. The large picture instead gives details of the calculation within the experimental range. The viscosities in the range  $10^5$  –  $10^{8.5}$  Pa s are interpolated to the experimental conditions.

### 5.4.3. Discussion

The most striking feature arising from this parameterisation is that for all the liquids investigated there is a common basis in the definition of the compositional parameter (SM), which does not take into account which network modifier is added to a base-composition. This raises several questions regarding the roles played by the different cations in a melt structure, and in particular seems to emphasise the cooperative role of any variety of network modifiers within the structure of multi-component systems.

Therefore it may not be ideal to use the rheological behaviour of systems to predict the behaviour of multi-component systems. A careful evaluation of what is relevant to understand natural processes must be analysed at the scale of the available simple and multi-component systems previously investigated. Such an analysis must be considered a priority. It will require a detailed selection of viscosities determined in previous studies. However, several viscosity measurements from previous investigations are recognized to be inaccurate and cannot be taken into account. In particular, it would suggested not to include the experimental viscosities measured in hydrated liquids because they involve a complex interaction among the elements in the silicate structure, experimental complications may influence the quality of the results and only low temperature data are available to date.

### **5.5. Predicting shear viscosity across the glass transition during volcanic processes: a calorimetric calibration**

Recently, it has been recognised that the liquid-glass transition plays an important role during volcanic eruptions (e.g. Dingwell and Webb, 1990; Dingwell, 1996) and intersection of this kinetic boundary, the liquid-to-glass or so-called “glass” transition can result in catastrophic consequences during explosive volcanic processes. This is because the mechanical response of the magma or lava to an applied stress at this brittle/ductile transition governs the eruptive behaviour (e.g. Sato et al., 1992; Papale, 1999) and has hence direct consequences for the assessment of hazards extant during a volcanic crisis. Whether an applied stress is accommodated by viscous deformation or by an elastic response is dependent on the timescale of the perturbation with respect to the timescale of the structural response of the geomaterial, i.e. its structural relaxation time (e.g. Moynihan, 1995; Dingwell, 1995) (section 2.1). A viscous response can accommodate orders of magnitude higher strain-rates than a brittle response. At larger applied stress magmas behave as Non-Newtonian fluids (Webb and Dingwell, 1990). Above a critical stress a ductile-brittle transition takes place, eventually culminating in the brittle failure or fragmentation (discussion is provided in section 2.1.5).

Structural relaxation is a dynamic phenomenon. When the cooling rate is sufficiently low, the melt has time to equilibrate its structural configuration at the molecular scale to each temperature. On the contrary, when the cooling rate is higher, the configuration of the melt at each temperature does not correspond to the equilibrium configuration at that temperature, since there is no time available for the melt to equilibrate. Therefore, the structural configuration at each temperature below the onset of the glass transition will also depend on the cooling rate. Since glass transition is related to the molecular configuration, it follows that glass transition temperature and associated viscosity will also depend on the cooling rate. For cooling rates in the order of several K/min, viscosities at glass transition take an approximate value of  $10^{11}$  -  $10^{12}$  Pa s (Scholze and Kreidl, 1986) and relaxation times are of order of 100 s.

The viscosity of magmas below a critical crystal and/or bubble content is controlled by the viscosity of the melt phase. Knowledge of the melt viscosity enables to calculate the relaxation time  $\tau$  of the system via the Maxwell relationship (section 2.1.4, Eq. 2.16).

Cooling rate data inferred for natural volcanic glasses which underwent glass transition have revealed variations of up to seven orders of magnitude across  $T_g$  from tens of Kelvin per second to less than one Kelvin per day (Wilding et al., 1995, 1996, 2000). A consequence is

that viscosities at the temperatures where the glass transition occurred were substantially different even for similar compositions. Rapid cooling of a melt will lead to higher glass transition temperatures at lower melt viscosities, whereas slow cooling will have the opposite effect, generating lower glass transition temperatures at correspondingly higher melt viscosities. Indeed, such a quantitative link between viscosities at the glass transition and cooling rate data for obsidian rhyolites based on the equivalence of their enthalpy and shear stress relaxation times has been provided (Stevenson et al., 1995). A similar equivalence for synthetic melts had been proposed earlier by Scherer (1984).

Combining calorimetric with shear viscosity data for degassed melts, it is possible to investigate whether the above-mentioned equivalence of relaxation times is valid for a wide range of silicate melt compositions relevant for volcanic eruptions. The comparison results in a quantitative method for the prediction of viscosity at the glass transition for melt compositions ranging from ultrabasic to felsic.

Here the viscosity of volcanic melts at the glass transition has been determined for 11 compositions ranging from basanite to rhyolite. Determination of the temperature dependence of viscosity, together with the cooling rate dependence of the glass transition, permits the calibration of the value of the viscosity at the glass transition for a given cooling rate. Temperature-dependent Newtonian viscosities have been measured using micropenetration methods (section 4.2.3), while their temperature-dependence is obtained using an Arrhenian equation like Eq. 2.1. Glass transition temperatures have been obtained using Differential Scanning Calorimetry (section 4.2.7). For each investigated melt composition, the activation energies obtained from calorimetry and viscometry are identical. This confirms that a simple shift factor can be used for each sample in order to obtain the viscosity at the glass transition for a given cooling rate in nature.

The results of this study indicate that there is a subtle but significant compositional dependence of the shift factor<sup>5</sup> of a factor of 10, from 10.8 to 9.8 in log terms. The composition-dependence of the shift factor is cast here in terms of a compositional parameter, the mol% of excess oxides (defined in section 2.2.2). Using such a parameterisation, a non-linear dependence of the shift factor upon composition that matches all 11 observed values within measurement errors is obtained. The resulting model permits the prediction of viscosity at the glass transition, for different cooling rates, with a maximum error of 0.1 log units.

---

<sup>5</sup> As it will be following explained (Eq. 5.9) and discussed (section 5.5.2) the *shift factor* is that amount which correlates shear viscosity and cooling rate data to predict the viscosity at the glass transition temperature  $T_g$ .

### 5.5.1. Sample selection and methods

The chemical compositions investigated during this study are graphically displayed in a total alkali vs. silica diagram (Fig. 5.21; after Le Bas et al., 1986) and involve basanite (EIF), trachybasalt (ETN), basalt (R839-5.8); phonotephrite (Ves\_Wt), tephriphonolite (Ves\_Gt), phonolite (Td\_ph), trachytes (MNV, ATN, PVC), dacite (UNZ) and rhyolite (P3RR, from Rocche Rosse flow, Lipari-Italy) melts.

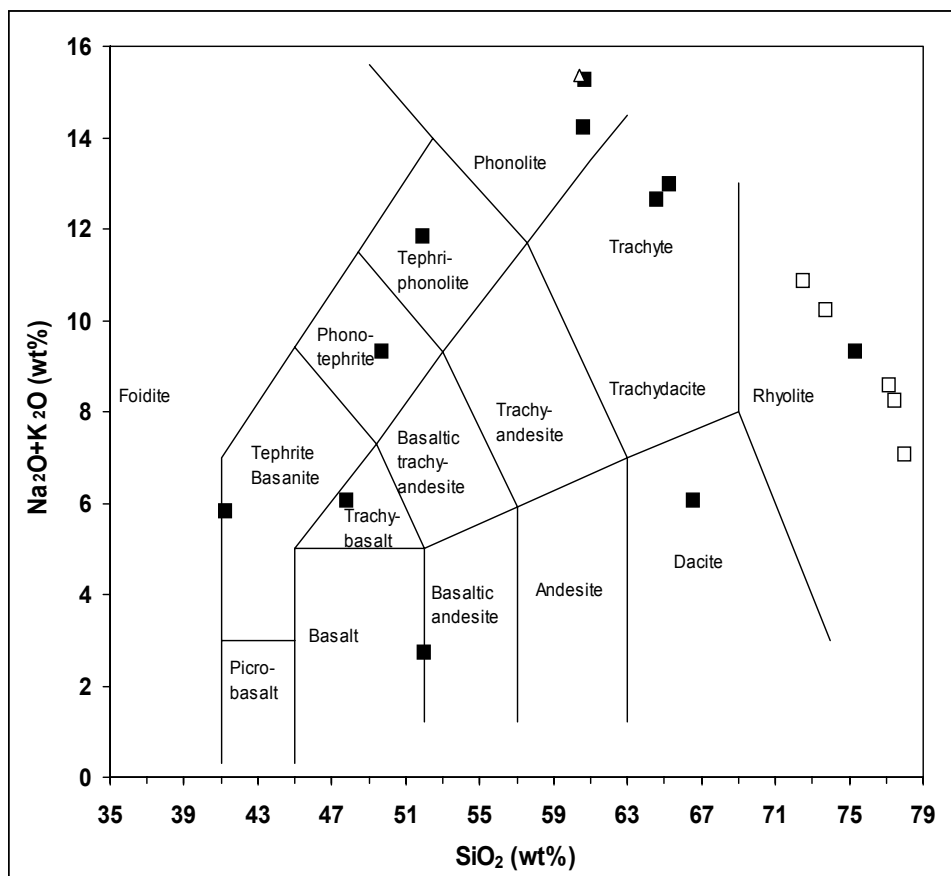


Fig. 5.21.: Total alkali vs. silica diagram (after Le Bas et al., 1986) of the investigated compositions. Filled squares are data from this study, open squares and open triangle represent data from Stevenson et al. (1995) and Gottsmann and Dingwell (2001a), respectively.

A DSC calorimeter and a micropenetration apparatus were used to provide the viscosities and the glass transition temperatures used in the following discussion according to the procedures illustrated in sections 4.2.3 and 4.2.7, respectively. The results are shown in Fig. 5.22 and 5.23 and Table 11.

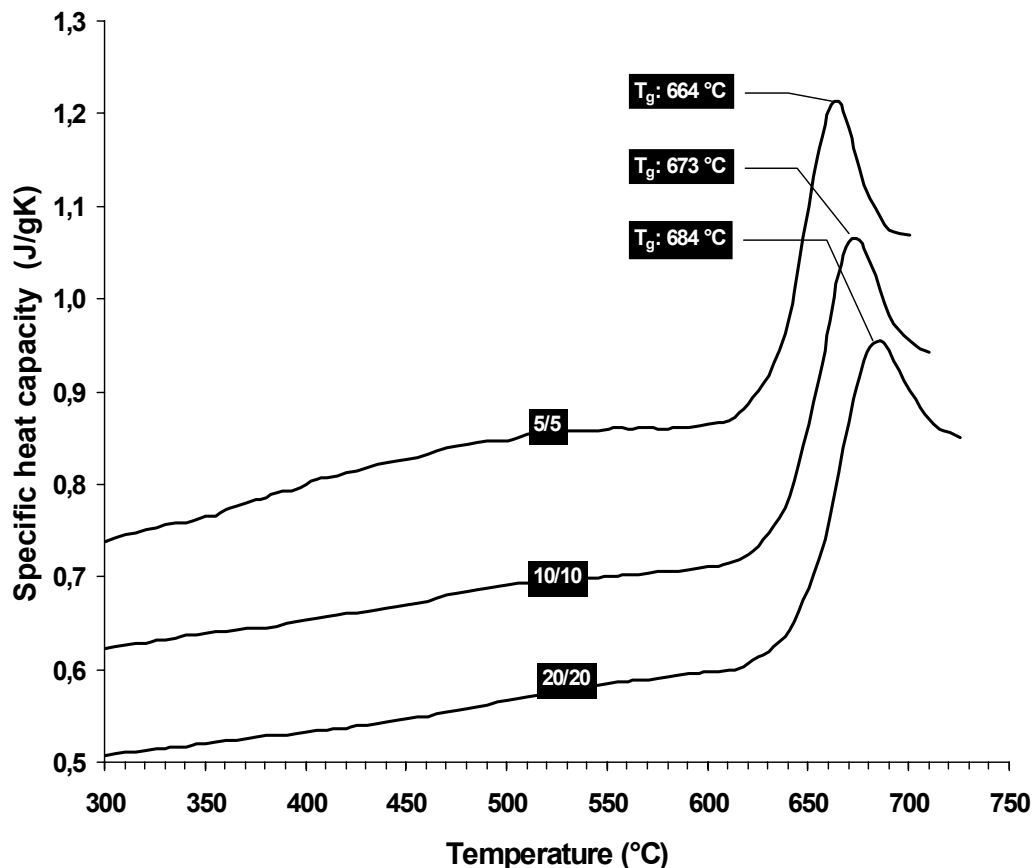


Fig. 5.22.: The specific heat capacity as a function of temperature for one of the investigated basalt sample (R839-5.8). The curves represent  $C_p$ -traces obtained during reheating the sample in the calorimeter to record the respective glass transition temperature as a function of cooling rate. With matching heating and cooling rates of 20, 10, and 5 K/min the glass transition temperatures differ of about 20 K. The quantification of the shift in glass transition temperatures (taken as the peak of the  $C_p$ -curve) as a function of cooling rate enables to calculate (Eq. 5.8) the activation energy for enthalpic relaxation (Table 12). The curves do not represent absolute values, but relative heat capacity.

In order to have crystal- and bubble-free glasses for viscometry and calorimetry, most samples investigated during this study were melted and homogenized using a concentric cylinder and then quenched. Their compositions hence correspond to virtually anhydrous melts with water contents below 200 ppm, with the exception of samples P3RR and R839-5.8. P3RR is a degassed obsidian sample from an obsidian flow with a water content of 0.16 wt% (Table 12). The microlite content is less than 1 vol% Gottsmann and Dingwell, 2001b). The hyaloclastite fragment R839-5.8 has a water content of 0.08 wt% (C. Seaman, pers. comm.) and a minor microlite content.

## 5.5.2. Results and discussion

### Viscometry

Table 11 lists the results of the viscosity measurements. The viscosity-inverse temperature data over the limited temperature range pertaining to each composition, are fitted via an Arrhenian expression (Fig. 5.23).

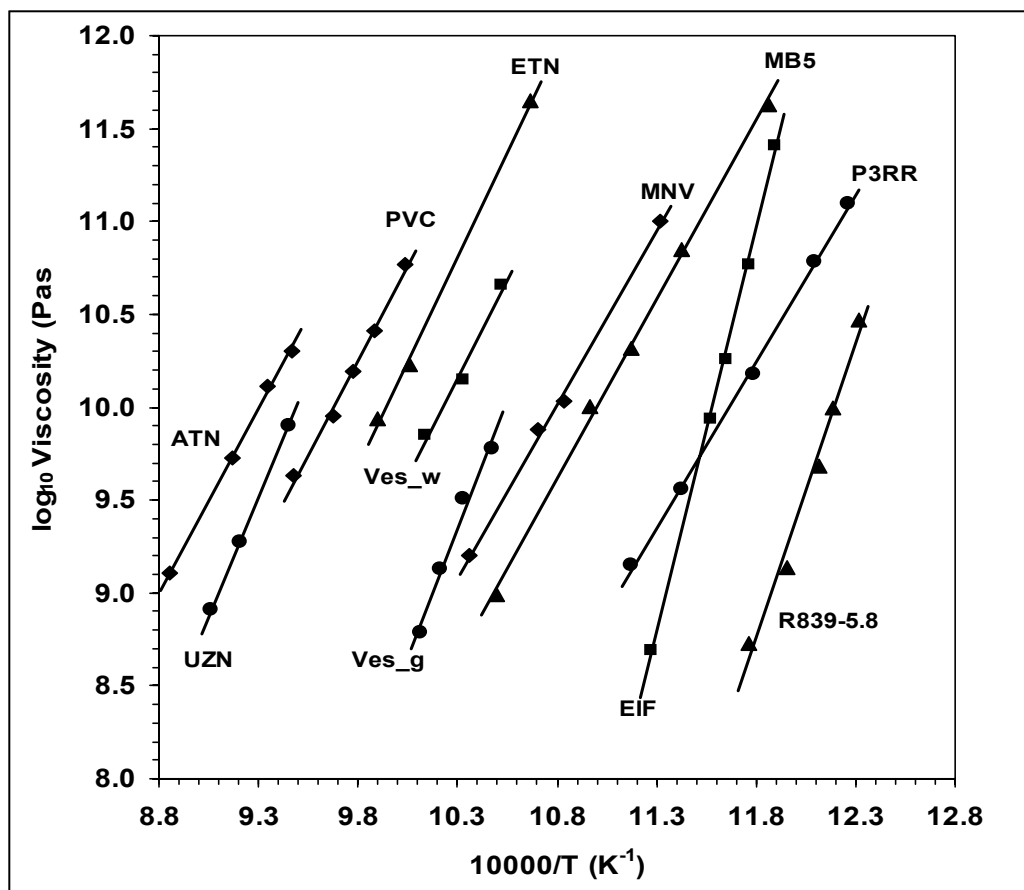


Fig. 5.23.: The viscosities obtained for the investigated samples using micropenetration viscometry. The data (Table 12) are fitted by an Arrhenian expression (Eq. 5.7). Resulting parameters are given in Table 12.

It is worth recalling that the entire viscosity – temperature relationship from liquidus temperatures to temperatures close to the glass transition for many of the investigated melts is Non-Arrhenian.

Employing an Arrhenian fit like the one at Eq. 2.2:

$$\log_{10} \eta = \log_{10} A_{\eta} + \frac{E_{\eta}}{2.303RT} \quad (5.7)$$

results in the determination of the activation energy for viscous flow (shear stress relaxation)  $E_\eta$  and a pre-exponential factor  $A_\eta$ .  $R$  is the universal gas constant (J/mol K) and  $T$  is absolute temperature.

Activation energies for viscous flow vary between 349 kJ/mol for rhyolite and 845 kJ/mol for basanite. Intermediate compositions have intermediate activation energy values, decreasing with the increasing polymerisation degree. This difference reflects the increasingly non-Arrhenian behaviour of viscosity versus temperature of ultrabasic melts as opposed to felsic compositions over their entire magmatic temperature range.

### Differential scanning calorimetry

The glass transition temperatures ( $T_g$ ) derived from the heat capacity data obtained during the thermal procedures described above may be set in relation to the applied cooling

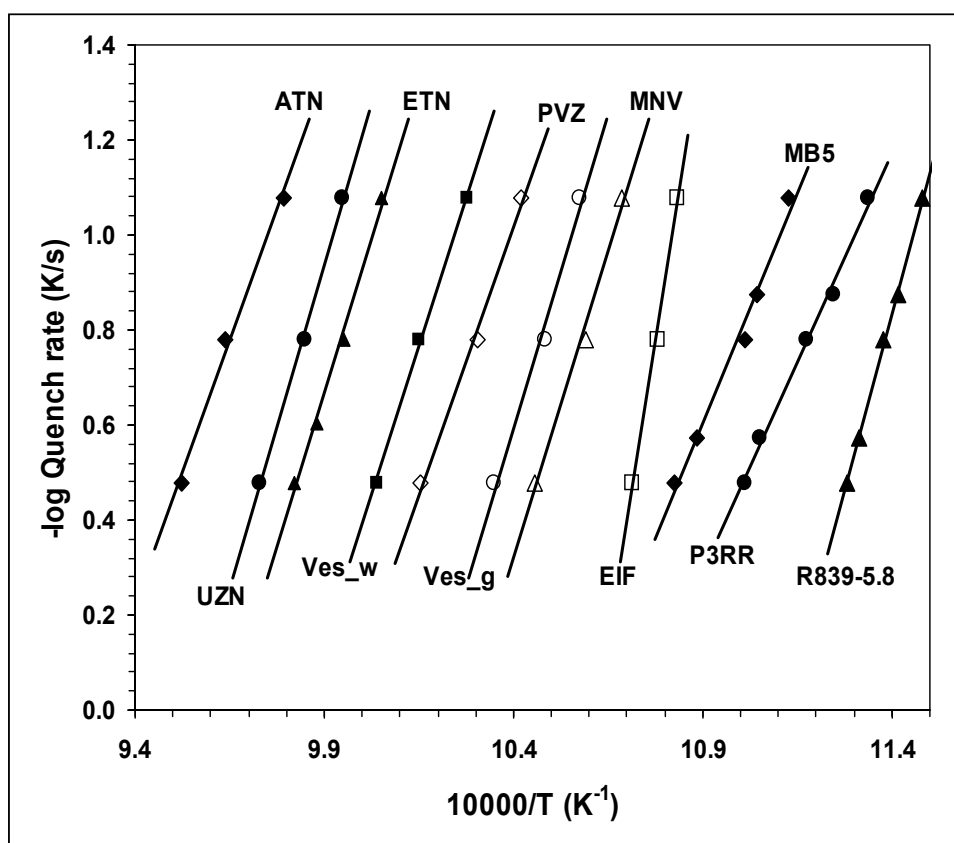


Fig. 5.24.: The quench rates as a function of  $10000/T_g$  (where  $T_g$  are the glass transition temperatures) obtained for the investigated compositions. Data were recorded using a differential scanning calorimeter. The quench rate vs.  $1/T_g$  data (cf. Table 11) are fitted by an Arrhenian expression given in Eq. 5.8. The resulting parameters are shown in Table 12.

rates ( $q$ ). An Arrhenian fit to the  $q$  vs.  $1/T_g$  data in the form of

$$\log_{10}|q| = \log_{10} A_{DSC} + \frac{E_{DSC}}{2.303RT_g} \quad (5.8)$$

gives the activation energy for enthalpic relaxation  $E_{DSC}$  and the pre-exponential factor  $A_{DSC}$ .  $R$  is the universal gas constant and  $T_g$  is the glass transition temperature in Kelvin. The fits to  $q$  vs.  $1/T_g$  data are graphically displayed in Figure 5.24. The derived activation energies show an equivalent range with respect to the activation energies found for viscous flow of rhyolite and basanite between 338 and 915 kJ/mol, respectively. The obtained activation energies for enthalpic relaxation and pre-exponential factor  $A_{DSC}$  are reported in Table 12.

#### The equivalence of enthalpy and shear stress relaxation times

Activation energies for both shear stress and enthalpy relaxation are within error equivalent for all investigated compositions (Table 12). Based on the equivalence of the activation energies, the equivalence of enthalpy and shear stress relaxation times is proposed for a wide range of degassed silicate melts relevant during volcanic eruptions. For a number of synthetic melts and for rhyolitic obsidians a similar equivalence was suggested earlier by Scherer (1984), Stevenson et al. (1995) and Narayanswamy (1988), respectively. The data presented by Stevenson et al. (1995) are directly comparable to the data and are therefore included in Table 12 as both studies involve i) dry or degassed silicate melt compositions and ii) a consistent definition and determination of the glass transition temperature. The equivalence of both enthalpic and shear stress relaxation times implies the applicability of a simple expression (Eq. 5.9) to combine shear viscosity and cooling rate data to predict the viscosity at the glass transition using the same shift factor  $K$  for all the compositions (Stevenson et al., 1995; Scherer, 1984).

$$\log_{10}\eta(at T_g) = K - \log_{10}|q| \quad (5.9)$$

To a first approximation, this relation is independent of the chemical composition (Table 12). However, it is possible to further refine it in terms of a compositional dependence.

Equation 5.9 allows the determination of the individual shift factors  $K$  for the compositions investigated. Values of  $K$  are reported in Table 12 together with those obtained by Stevenson et al. (1995). The constant  $K$  found by Scherer (1984) satisfying Eq. 5.9 was 11.4. The average shift factor for rhyolitic melts determined by Stevenson et al. (1995) was  $10.65 \pm 0.28$ . The average shift factor for the investigated compositions is  $9.99 \pm 0.16$ . The

reason for the mismatch of the shift factors determined by Stevenson et al. (1995) with the shift factor proposed by Scherer (1984) lies in their different definition of the glass transition temperature<sup>6</sup>. Correcting Scherer (1984) data to match the definition of  $T_g$  employed during this study and the study by Stevenson et al. (1995) results in consistent data. A detailed description and analysis of the correction procedure is given in Stevenson et al. (1995) and hence needs no further attention. Close inspection of these shift factor data permits the identification of a compositional dependence (Table 12). The value of  $K$  varies from 9.64 for

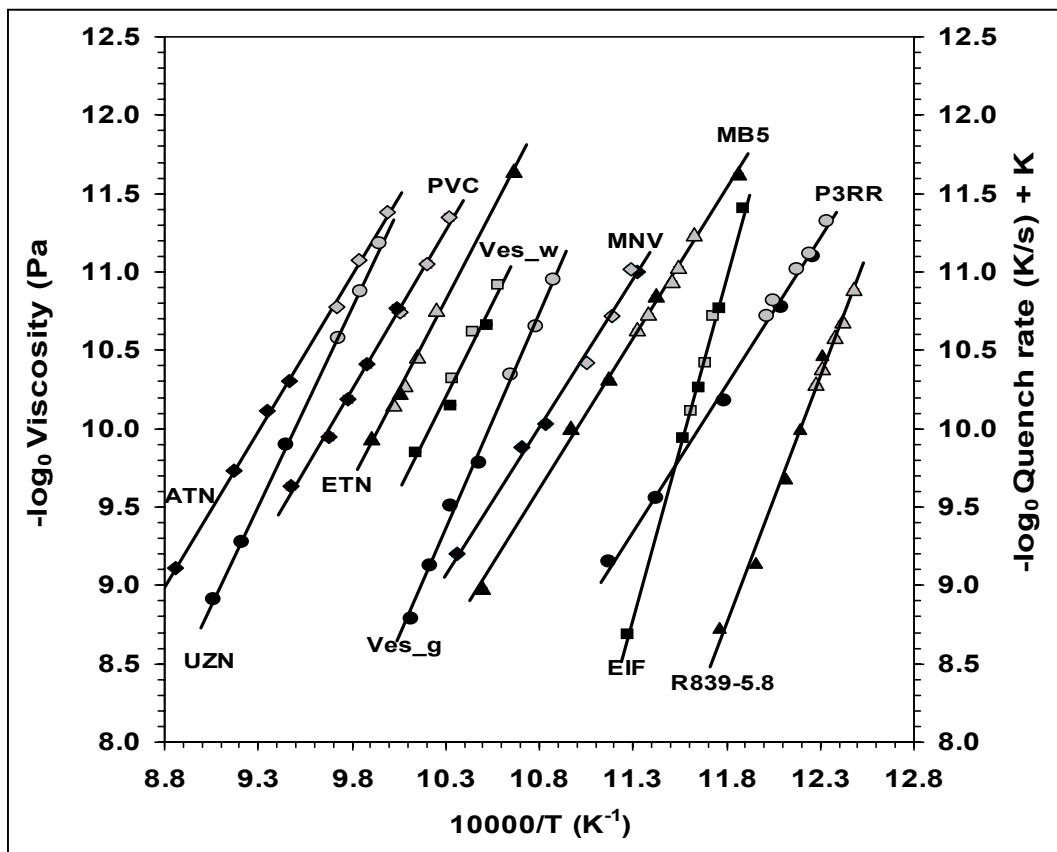


Fig. 5.25.: The equivalence of the activation energies of enthalpy and shear stress relaxation in silicate melts. Both quench quench rate vs.  $1/T_g$  data and viscosity data are related via a shift factor  $K$  to predict the viscosity at the glass transition. The individual shift factors are given in Table 12. Black symbols represent viscosity vs. inverse temperature data, grey symbols represent cooling rate vs. inverse  $T_g$  data to which the shift factors have been added. The individually combined data sets are fitted by a linear expression to illustrate the equivalence of the relaxation times behind both thermodynamic properties.

<sup>6</sup> The definition of glass transition temperature in material science is generally consistent with the onset of the heat capacity curves and differs from the definition adopted here where the glass transition temperature is more defined as the temperature at which the enthalpic relaxation occurs in correspondence of the peak of the heat capacity curves. The definition adopted in this and Stevenson et al. (1995) study is nevertheless less controversial as it is less subjected to personal interpretation.

the most basic melt composition to 10.24 (Fig. 5.25, Table 12) for calc-alkaline rhyolite P3RR. Stevenson et al. (1995) proposed in their study a dependence of  $K$  for rhyolites as a function of the Agpaitic Index.

Figure 5.26 displays the shift factors determined for natural silicate melts (including those by Stevenson et al., 1995) as a function of excess oxides. Calculating excess oxides as opposed to the Agpaitic Index allows better constraining the effect of the chemical composition on the structural arrangement of the melts. Moreover, the effect of small water contents of the individual samples on the melt structure is taken into account. As mentioned above, it is the structural relaxation time that defines the glass transition, which in turn has important implications for volcanic processes. Excess oxides are calculated by subtracting the molar percentages of  $\text{Al}_2\text{O}_3$ ,  $\text{TiO}_2$  and  $0.5\text{FeO}$  (regarded as structural network formers) from the sum of the molar percentages of oxides regarded as network modifying ( $0.5\text{FeO}$ ,  $\text{MnO}$ ,

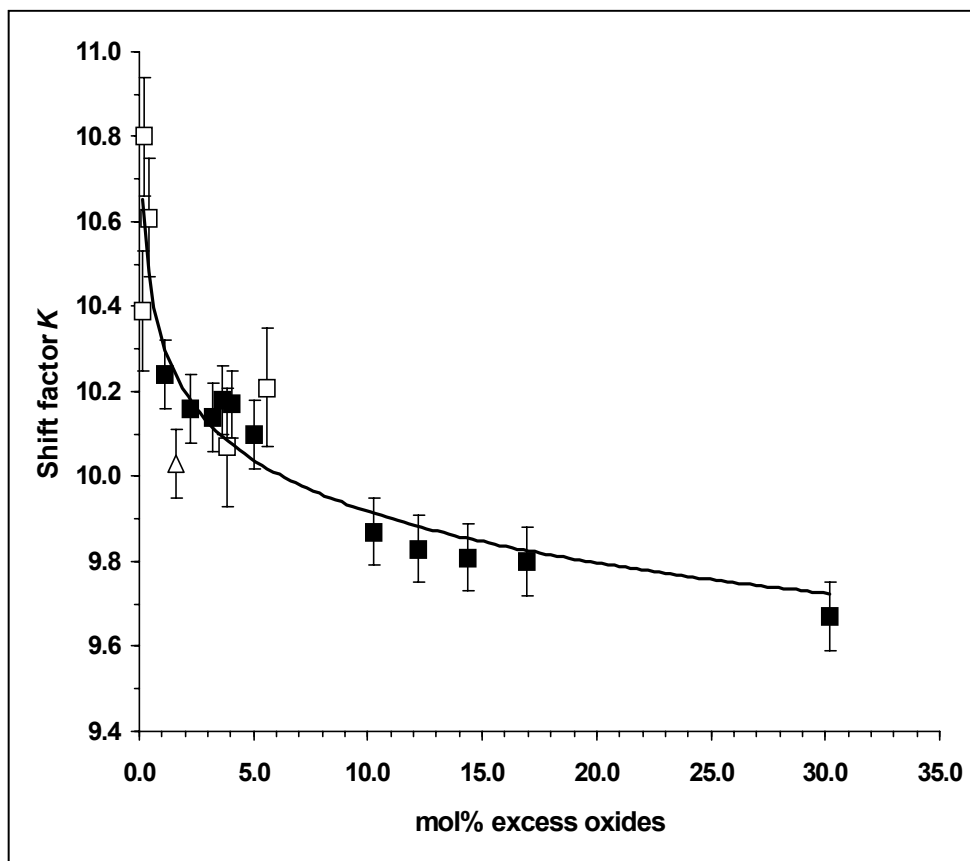


Fig. 5.26.: The shift factors as a function of the molar percentage of excess oxides in the investigated compositions. Filled squares are data from this study, open squares represent data calculated from Stevenson et al. (1995). The open triangle indicates the composition published in Gottsmann and Dingwell (2001). There appears to be a log natural dependence of the shift factors as a function of excess oxides in the melt composition (see Eq. 5.10). Knowledge of the shift factor allows predicting the viscosity at the glass transition for a wide range of degassed or anhydrous silicate melts relevant for volcanic eruptions via Eq. 5.9.

MgO, CaO, Na<sub>2</sub>O, K<sub>2</sub>O, P<sub>2</sub>O<sub>5</sub>, H<sub>2</sub>O) (e.g. Dingwell et al., 1993; Toplis and Dingwell, 1996; Mysen, 1988).

From Fig. 5.26 there appears to be a log natural dependence of the shift factors on excess oxides in the melt structure. Knowledge of the molar amount of excess oxides allows hence the determination of the shift factor via the relationship:

$$K = 10.321 - 0.175 \times \ln x \quad (R^2 = 0.824) \quad (5.10)$$

where  $x$  is the molar percentage of excess oxides. The curve in Fig. 5.26 represents the trend obtained by Eq. 5.10.

### Implications for the rheology of magma in volcanic processes

Knowledge of the viscosity at the glass transition is relevant for modelling volcanic processes. Depending on the time scale of a perturbation a viscoelastic silicate melt can envisage the glass transition at very different viscosities that may range over more than ten orders of magnitude (e.g. Webb, 1992). The rheological properties of the matrix melt in a multiphase system (melt + bubbles + crystals) will contribute to determine whether eventually the system will be driven out of structural equilibrium and will consequently cross the glass transition upon an applied stress. For situations where cooling rate data are available the results of this work permit estimation of the viscosity at which the magma crosses the glass transition and turns from a viscous (ductile) to a rather brittle behaviour.

If natural glass is present in volcanic rocks then the cooling process may be quantified partially by directly analysing the structural state of the glass. The glassy phase contains a structural memory, which can reveal the kinetics of cooling across the glass transition (e.g. De Bolt et al., 1976). Such a geospeedometer has been applied recently to several volcanic facies (Wilding et al., 1995, 1996, 2000; De Bolt et al., 1976; Gottsmann and Dingwell, 2000, 2001 a, b, 2002).

That work has shown that vitrification during volcanism can be the consequence of cooling at rates that vary by up to seven orders of magnitude. For example cooling rates across the glass transition are reported for evolved compositions from 10 K/s for tack-welded phonolitic spatter (Wilding et al., 1996) to less than  $10^{-5}$  K/s for pantellerite obsidian flows (Wilding et al., 1996; Gottsmann and Dingwell, 2001 b). Applying the corresponding shift factors allows proposing that viscosities associated with their vitrification may have differed as much as six orders of magnitude from  $10^{9.0}$  Pa s to  $\log_{10} 10^{15.3}$  Pa s (calculated from Eq.

5.9). For basic composition such as basaltic hyaloclastite fragments, available cooling rate data across the glass transition (Wilding et al., 2000; Gottsmann and Dingwell, 2000) between 2 K/s and 0.0025 K/s would indicate that the associated viscosities were in the range of  $10^{9.4}$  to  $10^{12.3}$  Pa s.

The structural relaxation times (calculated via Eq. 2.16) associated with the viscosities at the glass transition vary over six orders of magnitude for the observed cooling rates. This implies that for the fastest cooling events it would have taken the structure only 0.1 s to re-equilibrate in order to avoid the ductile-brittle transition, yet, obviously the thermal perturbation of the system was on an even faster timescale. For the slowly cooled pantellerite flows in contrast, structural reconfiguration may have taken more than one day to be achieved. A detailed discussion about the significance of very slow cooling rates and the quantification of the structural response of supercooled liquids during annealing is given in Gottsmann and Dingwell (2002).

The glass transition is associated with a drastic change of the derivative thermodynamic properties such as expansivity and heat capacity. It is also the rheological limit of viscous deformation of lava with formation of a rigid crust. The modelling of volcanic processes must therefore involve the accurate determination of this transition (Dingwell, 1995).

Most lavas are liquid-based suspensions containing crystals and bubbles. The rheological description of such systems remains experimentally challenging (see Dingwell, 1998 for a review). A partial resolution of this challenge is provided by the shift factors presented here (as demonstrated by Stevenson et al., 1995). The quantification of the melt viscosity should enable to better constrain the influence of both bubbles and crystals on the bulk viscosity of silicate melt compositions.

## 5.6. Conclusions

Developing a predictive model for the viscosity of natural silicate melts requires an understanding of how to partition the effects of composition across a non-Arrhenian model. At present, there is no definitive theory that establishes how the parameters in a non-Arrhenian equation [e.g.  $A_{TVF}$ ,  $B_{TVF}$ ,  $T_0$  (TVF, Eq. 2.9);  $A_e$ ,  $B_e$ ,  $S_{\text{conf}}$  (Configurational Entropy, Eq. 2.5)] should vary with composition. These parameters are not expected to be equally dependent on composition. In the short-term, the decisions governing how to expand the non-Arrhenian parameters in terms of the compositional effects will probably derive from empirical studying the same way as those developed in this work.

During the search for empirical relationships between the model parameters and composition, it is important to realize that the optimal parameter values (e.g. least squares solution) do not necessarily convey the entire story. The non-linear character of the non-Arrhenian models ensures strong numerical correlations between model parameters that mask the effects of composition. One result of the strong covariances between model parameters is that wide range of values for  $A_{TVF}$ ,  $B_{TVF}$  or  $T_0$  can be used to describe individual datasets. This is the case even where the data are numerous, well-measured, and span a wide range of temperatures and viscosities. In other words, there is a substantial range of model values, which, when combined in a non-arbitrary way, can accurately reproduce the experimental data. Strong liquids that exhibit near Arrhenian behaviour place only minor restrictions on the absolute range of values for  $A_{TVF}$ ,  $B_{TVF}$  and  $T_0$ .

Determination of the rheological properties of most fragile liquids, for example, basanite, basalt, phono-tephrite, tephri-phonolite, and phonolite helped to find quantitative correlations between important parameters, such as the pseudo-activation energy  $B_{TVF}$  and the TVF temperature  $T_0$ . A large number of new viscosity data for natural and synthetic multi-component silicate liquids allowed relationships between the model parameters and some compositional (SM) and compositional-structural (NBO/T) to be observed.

In particular, the SM parameter has shown a non-linear effect in reducing the viscosity of silicate melts, which is independent of the nature of the network modifier elements at high and low temperature.

These observations raise several questions regarding the roles played by the different cations and suggest that the combined role of all the network modifiers within the structure of multi-component systems hides the larger effects observed in simple systems, probably

because, within multi-component systems, the different cations are allowed to interpret non-univocal roles.

The relationships observed allowed a simple composition-dependent, non-Arrhenian model for multicomponent silicate melts to be developed. The model, which only requires the input of composition data, was tested using viscosity determinations measured by others research groups (Whittington et al. 2000, 2001; Neuville et al., 1993) using various different experimental techniques. The results indicate that this model may be able to predict the viscosity of dry silicate melts that range from basanite to phonolite and rhyolite and from dacite to trachyte in composition. The model was calibrated using liquids with a wide range of rheologies (from highly fragile (basanite) to highly strong (pure SiO<sub>2</sub>)) and viscosities (with differences on the order of 6 to 7 orders of magnitude). This is the first reliable model to predict viscosity using such a wide range of compositions and viscosities. It will enable the qualitative and quantitative description of all those petrological, magmatic and volcanic processes which involve mass transport (e.g. diffusion and crystallization processes, forward simulations of magmatic eruptions).

The combination of calorimetric and viscometric data has enabled a simple expression to predict shear viscosity at the glass transition. The basis for this stems from the equivalence of the relaxation times for both enthalpy and shear stress relaxation in a wide range of silicate melt compositions. A shift factor that relates cooling rate data with viscosity at the glass transition appears to be slightly but still dependent on the melt composition. Due to the equivalence of relaxation times of the rheological thermodynamic properties viscosity, enthalpy and volume (as proposed earlier by Webb, 1992; Webb et al., 1992) knowledge of the glass transition is generally applicable to the assignment of liquid versus glassy values of magma properties for the simulation and modelling of volcanic eruptions. It is however worth noting that the available shift factors should only be employed to predict viscosities at the glass transition for degassed silicate melts. It remains an experimental challenge to find similar relationship between viscosity and cooling rate (Zhang et al., 1997) for hydrous silicate melts.

## **6. Viscosity of hydrous silicate melts from Phlegrean Fields and Vesuvius: a comparison between rhyolitic, phonolitic and basaltic liquids.**

Newtonian viscosities of dry and hydrous natural liquids have been measured for samples representative of products from various eruptions. Samples have been collected from the Agnano Monte Spina (AMS), Campanian Ignimbrite (IGC) and Monte Nuovo (MNV) eruptions at Phlegrean Fields, Italy; the 1631 AD eruption of Vesuvius, Italy; the Montaña Blanca eruption of Teide on Tenerife, and the 1992 lava flow from Mt. Etna, Italy. Dissolved water contents ranged from dry to 3.86 wt%. The viscosities were measured using concentric cylinder and micropenetration apparatus, depending on the specific viscosity range (§ 4.2.1-4.2.3). Hydrous syntheses of the samples were performed using a piston cylinder apparatus (§ 4.2.2). Water contents were checked before and after the viscometry using FTIR spectroscopy and KFT, as indicated in sections from 4.2.4 to 4.2.6.

These measurements are the first viscosity determinations on natural hydrous trachytic, phonolitic, tephri-phonolitic and basaltic liquids. Liquid viscosities have been parameterised using a modified Tammann-Vogel-Fulcher (TVF) equation that allows viscosity to be calculated as a function of temperature and water content. These calculations are highly accurate for all temperatures under dry conditions, and for low temperatures, approaching the glass transition, under hydrous conditions. Calculated viscosities are compared with values obtained from literature for phonolitic, rhyolitic and basaltic composition. This shows that the trachytes have intermediate viscosities between rhyolites and phonolites, consistent with the dominant eruptive style associated with the different magma compositions (mainly explosive for rhyolite and trachytes, either explosive or effusive for phonolites and mainly effusive for basalts).

Compositional diversities among the analysed trachytes correspond to differences in liquid viscosities of 1-2 orders of magnitude, with higher viscosities approaching that of rhyolite at the same water content conditions. All hydrous natural trachytes and phonolites become indistinguishable when isokom temperatures are plotted against a compositional parameter given by the molar ratio on an element basis  $(\text{Si}+\text{Al})/(\text{Na}+\text{K}+\text{H})$ . In contrast, rhyolitic and basaltic liquids display distinct trends, with more fragile basaltic liquid crossing the curves of all the other compositions.

### **6.1. Sample selection and characterization.**

Samples from the deposits of historical and pre-historical eruptions of the Phlegrean Fields and Vesuvius were analysed that are relevant in order to understand the evolution of the eruptive style in these areas. In particular, while the Campanian Ignimbrite (IGC, 36,000 BP – Rosi et al., 1999) is the largest event so far recorded at Phlegrean Field and the Monte Nuovo (MNV, AD 1538 – Civetta et al., 1991) is the last eruptive event to have occurred at Phlegrean Fields, following a quiescence period of about 3000 years (Civetta et al. (1991)), the Agnano Monte Spina (AMS, ca. 4100 BP - de Vita et al., 1999) and the AD 1631 (eruption of Vesuvius) are currently used as a reference for the most dangerous possible eruptive scenarios at the Phlegrean Fields and Vesuvius respectively. Accordingly, the reconstructed dynamics of these eruptions and the associated pyroclast dispersal patterns are used in the preparation of hazard maps and Civil Defence plans for the surrounding areas (Rosi and Santacroce, 1984; Scandone et al., 1991; Rosi et al., 1993).

The dry materials investigated here were obtained by fusion of the glassy matrix from pumice samples collected within stratigraphic units corresponding to the peak discharge of the Plinian phase of the Campanian Ignimbrite (IGC), Agnano Monte Spina (AMS) and Monte Nuovo (MNV) eruptions of the Phlegrean Fields and the 1631AD eruption of Vesuvius. These units were level V3 (Voscone outcrop, Rosi et al., 1999) for IGC, level B1 and D1 (de Vita et al., 1999) for AMS, basal fallout for MNV and level C and E (Rosi et al., 1993) for the 1631 AD Vesuvius eruption, were sampled. The selected Phlegrean Fields eruptive events cover a large part of the magnitude, intensity, and compositional spectrum characterizing Phlegrean Fields eruptions. Compositional details are shown in section 3. 1 and Table 1.

A comparison between the viscosities of the natural phonolitic, trachytic, and basaltic samples here investigated and other synthetic phonolitic, trachytic (Whittington et al., 2001) and rhyolitic (Hess and Dingwell, 1996) liquids was used to verify the correspondence between the viscosities determined for natural and synthetic materials and to study the differences in the rheological behaviour of the compositional extremes.

## 6.2. Data modelling.

For all the investigated materials the viscosity interval explored becomes increasingly restricted as water is added to the initial base composition. While over the restricted range of each technique the behaviour of the liquid is apparently Arrhenian, a variable degree of non-Arrhenian behaviour emerges over the entire temperature range examined.

In order to fit all of the dry and hydrous viscosity data a non-Arrhenian model must be employed. The Adam-Gibbs theory, also known as configurational entropy theory (e.g. Richet and Bottinga, 1995; Toplis et al., 1997), provides a theoretical background to interpolate the viscosity data. The model equation (Eq. 2.5) from this theory is reported in section 2.1.2.

The Adam-Gibbs theory represents the optimal way to synthesize the viscosity data into a model, since the sound theoretical basis on which Eqs. (2.5) and (2.6) rely allows confident extrapolation of viscosity beyond the range of the experimental conditions. Unfortunately, the effects of dissolved water on  $A_e$ ,  $B_e$ , the configurational entropy at glass transition temperature  $S_{conf}(T_g)$ , and  $C_{p_{conf}}(T)$ , are poorly known. This implies that the use of Eq. 2.5 to model the viscosity of dry and hydrous liquids requires arbitrary functions to allow for each of these parameters dependence on water. This results in a semi-empirical form of the viscosity equation and sound theoretical basis is lost. Therefore there is no strong reason to prefer the configurational entropy theory (Eqs. 2.5-2.6) to the TVF empirical relationships. The capability of equation 2.9 to reproduce dry and hydrous viscosity data has already been shown in Fig. 5.11 for dry samples.

As shown in Fig. 6.1 the viscosities investigated in this study are reproduced well by a modified form of the TVF equation (Eq. 2.9):

$$A_{TVF} = a_1 + a_2 \ln w_{H_2O} \quad (6.1)$$

$$B_{TVF} = b_1 + b_2 w_{H_2O} \quad (6.2)$$

$$T_0 = c_1 + c_2 \ln w_{H_2O} \quad (6.3)$$

where  $\eta$  is viscosity,  $a_1$ ,  $a_2$ ,  $b_1$ ,  $b_2$ ,  $c_1$  and  $c_2$  are fit parameters, and  $w_{H_2O}$  is the concentration of water. When fitting the data via Eqs. 6.1/6.3,  $w_{H_2O}$  is assumed to be  $\geq 0.02$  wt%. Such a constraint corresponds with several experimental determinations, for example, those from Ohlhorst et al. (2001) and Hess et al. (2001). These authors, on the basis of their results on polymerised as well as depolymerised melts, conclude that a water content on the order of 200 ppm is present even in the most degassed glasses.

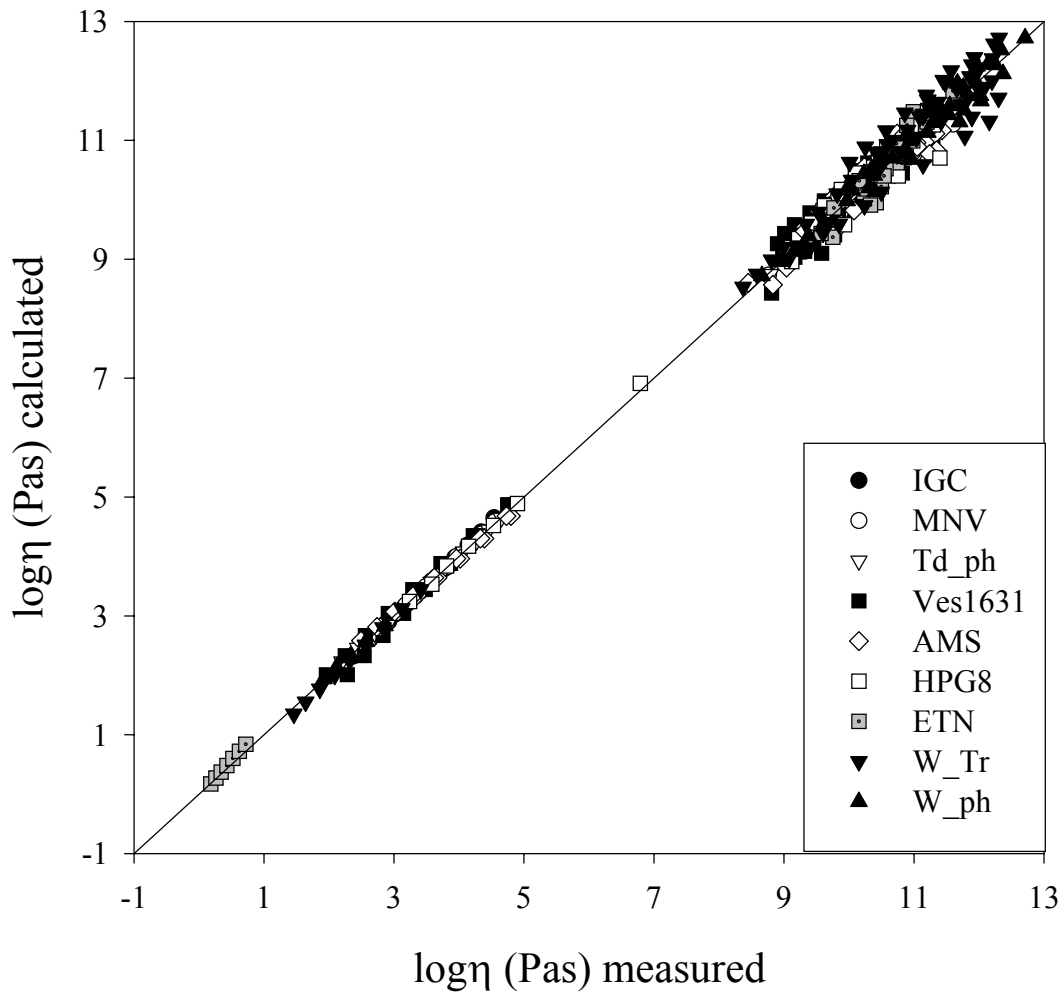


Fig. 6.1.: Comparison between the measured and the calculated (Eqs. 2.9; 6.1/6.3) data for the investigated liquids.

Particular care must be taken to fit the viscosity data. In section 5.2 evidence is provided that showed that fitting viscosity-temperature data to non-Arrhenian rheological models can result in strongly correlated or even non-unique and sometimes unphysical, model parameters ( $A_{TVF}$ ,  $B_{TVF}$ ,  $T_0$ ) for a TVF equation (Eqs. 2.9; 6.1/6.3). Possible sources of error for typical magmatic or magmatic-equivalent fragile to strong silicate melts were quantified and discussed. In particular, measurements must not be limited to a single technique and more than one datum must be provided by the high and low temperature techniques. Particular care must be taken when working with strong liquids. In fact, the range of acceptable values for parameters  $A_{TVF}$ ,  $B_{TVF}$  and  $T_0$  for strong liquids is 5-10 times greater than the range of values estimated for fragile melts (chapter 5). This problem is partially solved if the interval of measurement and the number of experimental data is large. Attention should also be focused on obtaining physically consistent values of the parameters. In fact,  $B_{TVF}$  and  $T_0$  cannot be negative, and  $A_{TVF}$  is likely to be negative in silicate melts (e.g. Angell, 1995). Finally, the

validity of the calibrated equation must be verified in the space of the variables, and in their range of interest, in order to prevent unphysical results such as a viscosity increase with addition of water or temperature increase. Extrapolation of data beyond the experimental range should be avoided or limited, and carefully discussed.

However, it remains uncertain to what the viscosities calculated via Eqs. 6.1/6.3 can be used to predict viscosities at conditions relevant for the magmatic and volcanic processes. For hydrous liquids this is in a region corresponding to temperatures between about 1000 and 1300 K. The production of viscosity data in such conditions is hampered by water exsolution and crystallization kinetics that occur on a timescale similar to that of measurements. Recent investigations (Dorfmann et al., 1996) are attempting to obtain viscosity data at high pressure, therefore reducing or eliminating the water exsolution-related problems (but possibly requiring the use of  $P$ -dependent terms in the viscosity modelling). Therefore the liquid viscosities calculated at eruptive temperatures with Eqs. 6.1/6.3 need therefore to be confirmed by future measurements.

### 6.3. Results.

Figures 6.2 and 6.3 show the dry and hydrous viscosities measured in samples from Phlegrean Fields and Vesuvius, respectively. The viscosity values are reported in Tables 3 and 13.

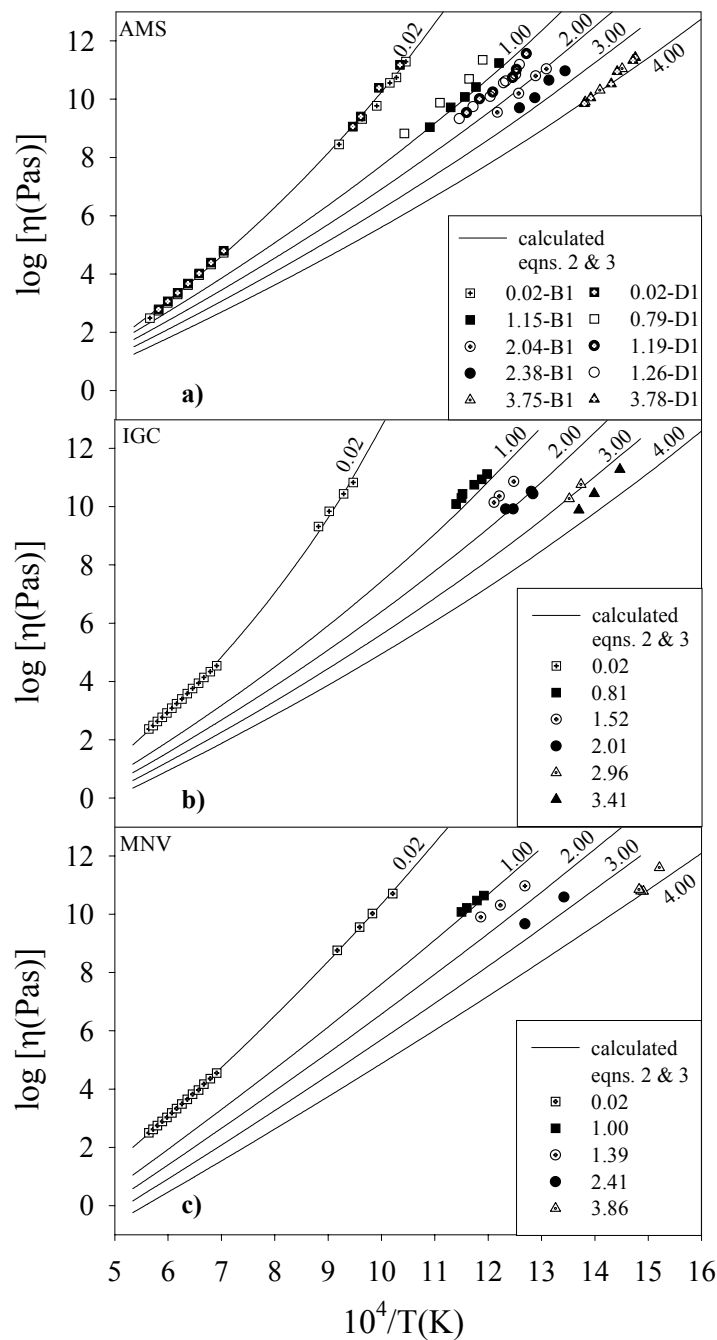


Fig. 6. 2.: Viscosity measurements (symbols) and calculations (lines) for the AMS (a), the IGC (b) and the MNV (c) samples. The lines are labelled with their water content (wt%). Each symbol refers to a different water content (shown in the legend). Samples from two different stratigraphic layers (level B1 and D1) were measured from AMS.

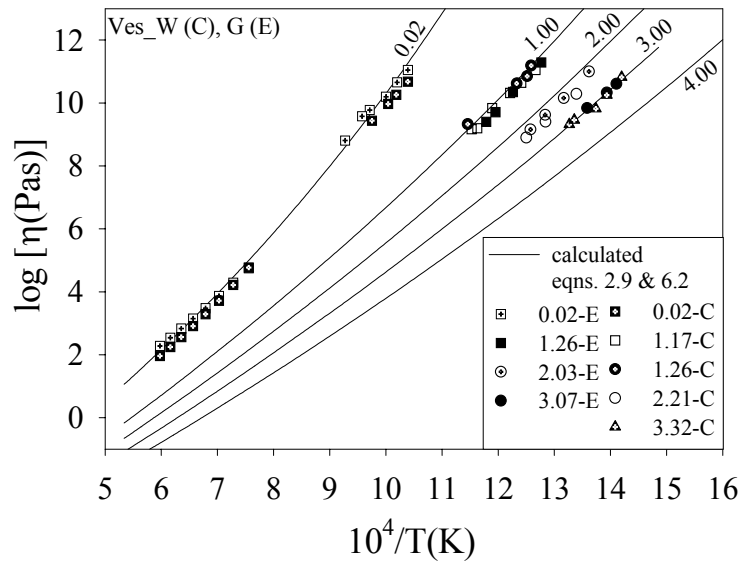


Fig. 6. 3.: Viscosity measurements (symbols) and calculations (lines) for the AMS (B1, D1) samples. The lines (calculations) are labelled with their water contents (wt%). The symbols refer to the water content dissolved in the sample. Samples from two different stratigraphic layers (level C and E) corresponding to Ves\_W and Ves\_G were analyzed from the 1631 AD Vesuvius eruption.

These figures also show the viscosity analysed (lines) calculated from the parameterisation of Eqs.2.9, 6.1/6.3. The  $a_1$ ,  $a_2$ ,  $b_1$ ,  $b_2$ ,  $c_1$  and  $c_2$  fit parameters for each of the investigated compositions are listed in Table 14.

In general, the explored viscosity interval becomes more and more restricted as further water is added to the initial base-composition. The addition of water to the melts results in a large shift of the viscosity-temperature relationship, which is in good agreement with the trend observed for a wide range of natural and synthetic melts (e.g. Whittington et al., 2001; Dingwell et al., 1996; Holtz et al., 1999; Romano et al., 2000).

In general, the explored viscosity interval becomes more and more restricted as further water is added to the initial base-composition. The addition of water to the melts results in a large shift of the viscosity-temperature relationship, which is in good agreement with the trend observed for a wide range of natural and synthetic melts (e.g. Whittington et al., 2001; Dingwell et al., 1996; Holtz et al., 1999; Romano et al., 2000).

The melt viscosity drops dramatically when the first 1 wt% H<sub>2</sub>O is added to the melt, then tends to level off with further addition of water. The drop in viscosity as water is added to the melt is slightly higher for the Vesuvius phonolites than for the AMS trachytes.

Figure 6.4 shows the calculated viscosity curves for several different liquids of rhyolitic, trachytic, phonolitic, and basaltic compositions, including those analysed in previous studies by Whittington et al. (2001) and Hess and Dingwell (1996). The curves refer to the viscosity

at a constant temperature of 1100 K, at which the values for hydrated conditions are extrapolated using Eqs. 2.9 and 6.1/6.3.

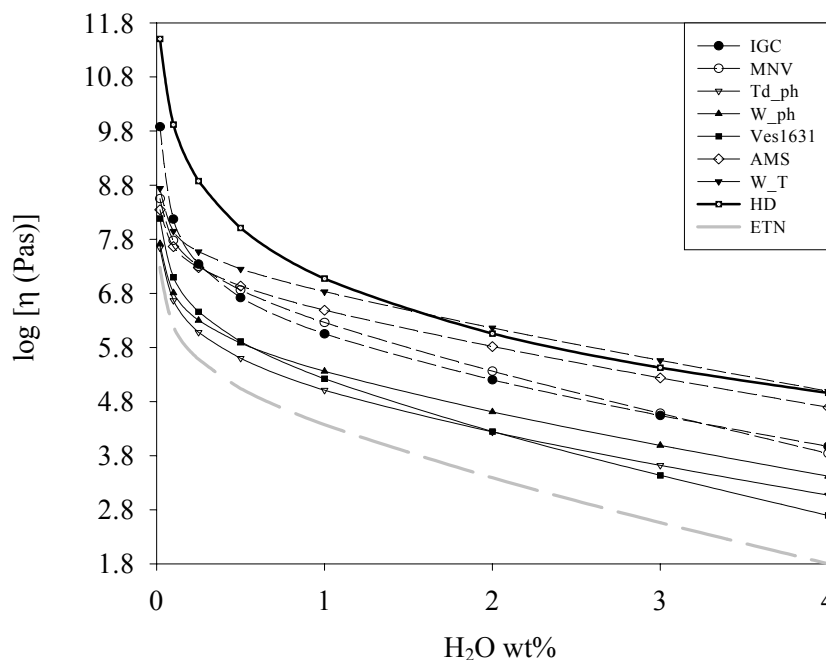


Fig. 6.4.: Viscosity as a function of water content for natural rhyolitic, trachytic, phonolitic, and basaltic liquids, at  $T = 1100$  K. In this figure, and in figures 6.5-6.8, the different compositional groups are indicated with different lines: solid thick line for rhyolite, dashed lines for trachytes, solid thin lines for phonolites, long-dashed grey line for basalt.

Consequently, the calculated uncertainties for the viscosities in hydrated conditions are larger than those calculated at dry conditions. The curves show well distinct viscosity paths for each different compositional group. The viscosities of rhyolites and trachytes at dissolved water contents greater than about 1-2 wt% are very similar.

At lower water contents rhyolites have higher viscosities by up to 4 orders of magnitude. The new viscosity data presented in this study confirm this trend, with the exception of the dry viscosity of the Campanian Ignimbrite liquid, which is about 2 orders of magnitude higher than that of the other analysed trachytic liquids from the Phlegrean Fields, and the hydrous viscosities of the IGC and MNV samples, which are appreciably lower (by less than 1 order of magnitude) than that of the AMS sample.

The field of phonolitic liquids is distinct from that of trachytic liquids, with the phonolitic liquids having substantially lower viscosities, except in dry conditions, where viscosities of the two compositional groups are comparable. Finally, basaltic liquids from Mount Etna are

significantly less viscous than the other compositions in both dry and hydrous conditions (Figure 6.4).

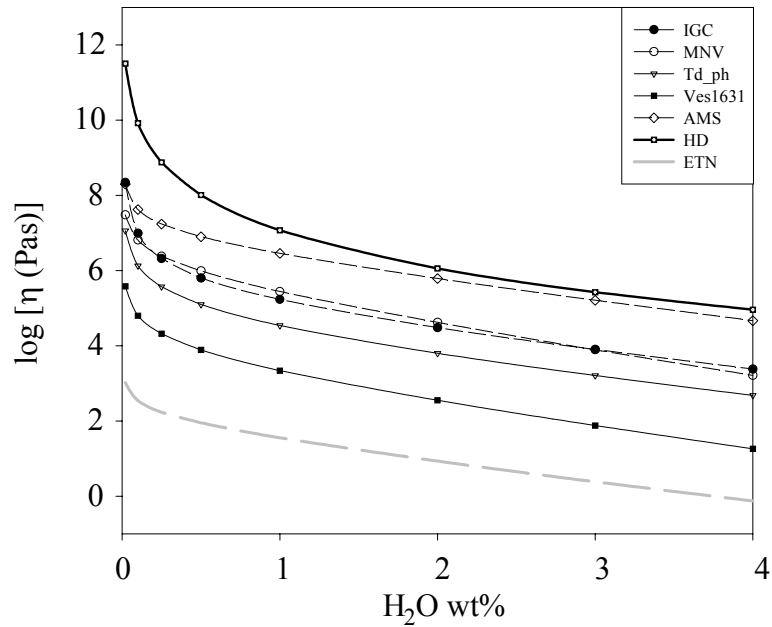


Fig. 6.5.: Viscosity as a function of water content for natural rhyolitic, trachytic, phonolitic, and basaltic liquids, at their respective estimated eruptive temperature. Eruptive temperatures from Ablay et al. (1995) (Td\_ph), Roach and Rutherford (2001) (AMS, IGC and MNV), Rosi et al. (1993) (Ves1631). A typical eruptive temperature for rhyolite is assumed to be equal to 1100 K.

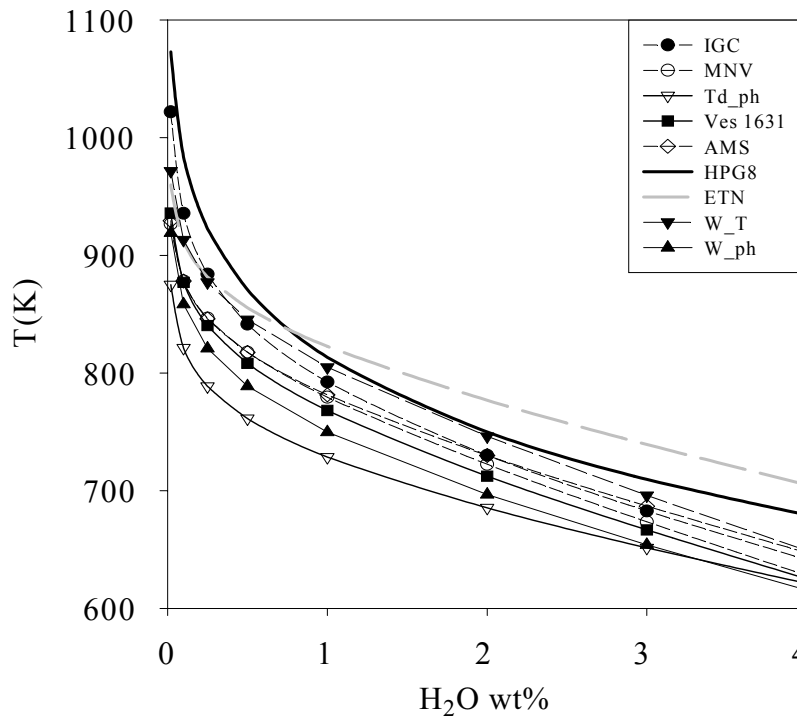


Fig. 6.6.: Isokom temperature at  $10^{12}$  Pa·s, as a function of water content for natural rhyolitic, trachytic, phonolitic and basaltic liquids.

Figure 6.5 shows the calculated viscosity curves for the compositions in Fig. 6.4, at their eruptive temperature. The general relationships between the different compositional groups remain the same, but the differences in viscosity between basalt and phonolites, and between phonolites and trachytes, become larger.

At dissolved water contents larger than 1-2 wt%, the trachytes have viscosities on the order of 2 orders of magnitude lower than rhyolites with the same water content, and viscosities from less than 1 to about 3 orders of magnitude higher than those of phonolites with the same water content. The Etnean basalt has viscosities at eruptive temperature which are about 2 orders of magnitude lower than those of the Vesuvius phonolites, 3 orders of magnitude lower than those of the Teide phonolite, and up to 4 orders of magnitude lower than those of the trachytes and rhyolites.

Figure 6.6 shows the isokom temperature (i.e., the temperature at fixed viscosity) in this case  $10^{12}$  Pa·s, for the compositions analysed in this study and those from other studies that have been used for comparison.

Such a high viscosity is very close to the glass transition (Richet and Bottinga, 1986), and it is close to the experimental conditions at all water contents employed in the experiments (Table 13 and Figs. 6.2-6.3). This ensures that the errors introduced by the viscosity parameterisation of Eqs. 2.9 and 6.1 are at a minimum, giving an accurate picture of the viscosity relationships for the considered compositions. The most striking feature of the relationship are the crossovers between the isokom temperatures of the basalt and the rhyolite, and the basalt and the trachytes from the IGC eruption and W\_T (Whittington et al., 2001), at a water content of less than 1 wt%. Such crossovers were also found to occur between synthetic tephritic and basanitic liquids (Whittington et al., 2000) and interpreted to be due to the larger depolymerising effect of water in liquids that are more polymerised at dry conditions (Whittington et al., 2000). The data and parameterisation show that the isokom temperature of the Etnean basalt at dry conditions is higher than those of phonolites and AMS and MNV trachytes. This implies that the effect of water on viscosity is not the only explanation for the high isokom temperature of basalt at high viscosity. Crossovers do not occur at viscosities less than about  $10^{10}$  Pa·s (not shown in the figure). Apart from the basalt, the other liquids in Fig. 6.6 show relationships similar to those in Fig. 6.4, with phonolites occupying the lower part of the diagram, followed by trachytes, then by rhyolite.

Less relevant changes with respect to the lower viscosity fields in Fig. 6.4 are represented by the position of the IGC curve, which is above those of other trachytes over most of the

investigated range of water contents and by the position of the Ves1631 phonolite, which is still below but close to the trachyte curves.

If the trachytic and the phonolitic liquids with high viscosity (low T, high H<sub>2</sub>O content) are plotted against a modified total alkali silica ratio ( $TAS^* = (Na+K+H) / (Si+Al)$  - elements calculated on molar basis) they both follow the same well defined trend. Such a trend is best evidenced in an isokom temperature vs.  $1/TAS^*$  diagram, where the isokom temperature is the temperature corresponding to a constant viscosity value of  $10^{10.5}$  Pa·s. Such a high viscosity falls within the range of the measured viscosities for all conditions from dry to hydrous (Fig. 6.2-6.3), therefore, the error introduced by the viscosity parameterisation at Eqs. 2.9 and 6.1 is minimum. Figure 6.7 shows the relationship between the isokom temperatures and the  $1/TAS^*$  parameter for the Phlegrean Fields and the Vesuvius samples. It also includes the calculated curves for the Etnean Basalt and the haplogranitic composition HPG8 from

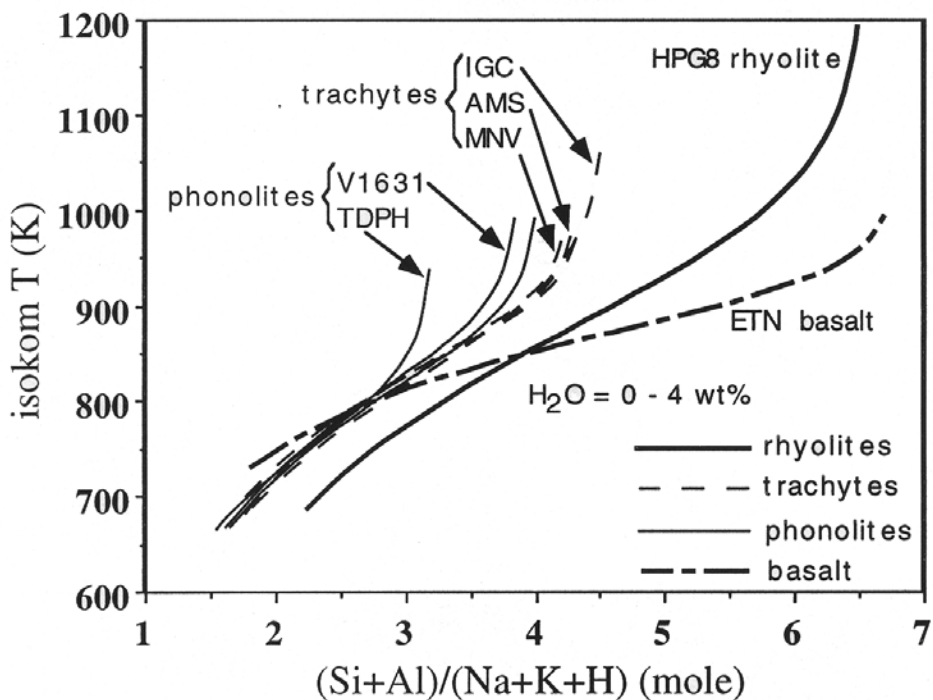


Fig. 6.7.: Isokom temperature corresponding to  $10^{10.5}$  Pa·s plotted against the inverse of  $TAS^*$  parameter defined in the text. The HPG8 rhyolite (Dingwell et al., 1996) has been used to obtain appropriate  $TAS^*$  values for rhyolites.

Dingwell et al. (1996). As can be seen, the existence of a unique trend for hydrous trachytes and phonolites is confirmed by the measurements and parameterisations performed in this study. In spite of the large viscosity differences between trachytes and phonolites, as well as between different trachytic and phonolitic liquids (shown in Fig. 6.4), these liquids become the same as long as hydrous conditions ( $w_{H_2O} > 0.3$  wt%, or  $> 0.6$  wt% for the Teide phonolite) are considered together with the compositional parameter  $TAS^*$ . The Etnean basalt

(ETN) and the HPG8 rhyolite display very different curves in Fig. 6.7. This is interpreted as being due to the very large structural differences characterizing highly polymerised (HPG8) or highly de-polymerised (ETN) liquids compared to the moderately polymerised liquids with trachytic and phonolitic composition (Romano et al., 2002).

#### **6.4. Discussion.**

In this study the viscosities of dry and hydrous trachytes from the Phlegrean Fields were measured that represent the liquid fraction flowing along the volcanic conduit during plinian phases of the Agnano Monte Spina, Campanian Ignimbrite and Monte Nuovo eruptions. These measurements represent the first viscosity data, not only for Phlegrean Fields trachytes, but for natural trachytes in general. Viscosity measurements on a synthetic trachyte and a synthetic phonolite presented by Whittington et al. (2001) are discussed together with the results for natural trachytes and other compositions from the present investigation. Results obtained for rhyolitic compositions (Hess and Dingwell, 1996) were also analysed.

The results clearly show that separate viscosity fields exist for each of the compositions, with trachytes being in general more viscous than phonolites and less viscous than rhyolites. The high viscosity plot in Fig. 6.7 shows the trend for calculations made at conditions close to those of the experiments. The same trend is also clear in the extrapolations of Figs. 6.4 and 6.5, which correspond to temperatures and water contents similar to those that characterize the liquid magmas in natural conditions. In such cases the viscosity curve of the AMS liquid tends to merge with that of the rhyolitic liquid for water contents greater than a few wt%, deviating from the trend shown by IGC and MNV trachytes. Such a deviation is shown in Fig. 6.4, which refers to the 1100 K isotherm, and corresponds to a lower slope of the viscosity vs. water content curve of the AMS with respect to the IGC and MNV liquids. The only points in Fig. 6.4 that are well constrained by the viscosity data are those corresponding to dry conditions (see Fig. 6.2). The accuracy of viscosity calculations at the relatively low-viscosity conditions in Figs. 6.4 and 6.5 decrease with increasing water content. Therefore it is possible that the diverging trend of AMS with respect to IGC and MNV in Fig. 6.4 is due to the approximations introduced by the viscosity parameterisation of Eqs. 2.9 and 6.1/6.3. However, it is worth noting that the synthetic trachytic liquid analysed by Whittington et al. (2001) (W\_T sample) produces viscosities at 1100 K which are closer to that of AMS trachyte, or even slightly more viscous, when the data are fitted by Eqs. 2.9 and 6.1/6.3.

In conclusion, while it is now clear that hydrous trachytes have viscosities that are intermediate between those of hydrous rhyolites and phonolites, the actual range of possible viscosities for trachytic liquids from Phlegrean Fields at close-to-eruptive temperature conditions can currently only be approximately constrained. These viscosities vary, at equal water content, from that of hydrous rhyolite to values about one order of magnitude lower (Fig. 6.4), or two orders of magnitude lower when the different eruptive temperatures of rhyolitic and trachytic magmas are taken into account (Fig. 6.5). In order to improve our

capability of calculating the viscosity of liquid magmas at temperatures and water contents approaching those in magma chambers or volcanic conduits, it is necessary to perform viscosity measurements at these conditions. This requires the development and standardization of experimental techniques that are capable of retaining the water in the high temperature liquids for a time longer than is required for the measurement. Some steps have been made in this direction, by employing the falling sphere method in conjunction with a centrifuge apparatus (CFS) (Dorfman et al., 1996). The CFS increases the apparent gravity acceleration, thus significantly reducing the time required for each measurement. It is hoped that similar techniques will be routinely employed in the future to measure hydrous viscosities of silicate liquids at intermediate to high temperature conditions.

The viscosity relationships between the different compositional groups of liquids in Figs. 6.4 and 6.5 are also consistent with the dominant eruptive styles associated with each composition. A relationship between magma viscosity and eruptive style is described in Papale (1999) on the basis of numerical simulations of magma ascent and fragmentation along volcanic conduits. Other conditions being equal, a higher viscosity favours a more efficient feedback between decreasing pressure, increasing ascent velocity, and increasing multiphase magma viscosity. This culminates in magma fragmentation and the onset of an explosive eruption. Conversely, low viscosity magma does not easily achieve the conditions for the magma fragmentation to occur, even when the volume occupied by the gas phase exceeds 90% of the total volume of magma. Typically it erupts in effusive (non-fragmented) eruptions. The results presented here show that at eruptive conditions, largely irrespective of the dissolved water content, the basaltic liquid from Mount Etna has the lowest viscosity. This is consistent with the dominantly effusive style of its eruptions. Phonolites from Vesuvius are characterized by viscosities higher than those of the Mount Etna basalt, but lower than those of the Phlegrean Fields trachytes. Accordingly, while lava flows are virtually absent in the long volcanic history of Phlegrean Fields, the activity of Vesuvius is characterized by periods of dominant effusive activity alternated with periods dominated by explosive activity. Rhyolites are the most viscous liquids considered in this study, and as predicted rhyolitic volcanoes produce highly explosive eruptions.

Different from hydrous conditions, the dry viscosities are well constrained from the data at all temperatures from very high to close to the glass transition (Fig. 6.2). Therefore, the viscosities of the dry samples calculated using Eqs. 2.9 and 6.1/6.3 can be regarded as an accurate description of the actual (measured) viscosities. Figs. 6.4-6.6 show that at temperatures comparable with those of eruptions, the general trends in viscosity outlined above for hydrous

conditions are maintained by the dry samples, with viscosity increasing from basalt to phonolites to trachytes to rhyolite. However, surprisingly at low temperature, close to the glass transition (Fig. 6.6) the dry viscosity (or the isokom temperature) of phonolites from the 1631 Vesuvius eruption becomes slightly higher than that of AMS and MNV trachytes, and even more surprising is the fact that the dry viscosity of basalt from Mount Etna becomes higher than those of trachytes, except the IGC trachyte which shows the highest dry viscosity among trachytes. The crossover between basalt and rhyolite isokom temperatures, corresponding to a viscosity of  $10^{12}$  Pa·s, (Fig. 6.6) is not only due to a shallower slope, as pointed out by Whittington et al. (2000), but it is also due to a much more rapid increase in

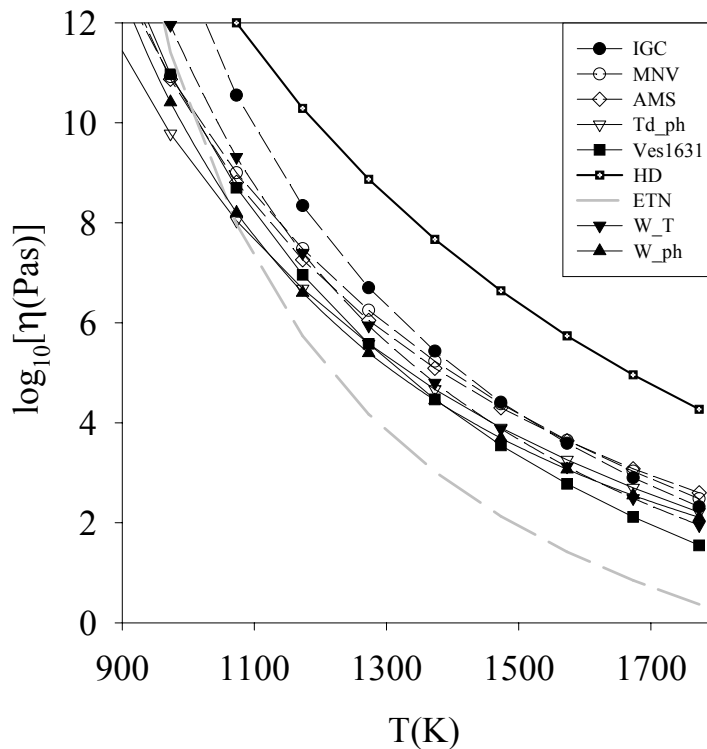


Figure 6.8.: Viscosity versus temperature for rhyolitic, trachytic, phonolitic, and basaltic liquids with water content of 0.02 wt%.

the dry viscosity of the basalt with decreasing temperature approaching the glass transition temperature (Fig. 6.8). This increase in the dry viscosity in the basalt is related to the more fragile nature of the basaltic liquid with respect to other liquid compositions. Fig. 6.5 also shows that contrary to the hypothesis in Whittington et al. (2000), the viscosity of natural liquids of basaltic composition is always much less than that of rhyolites, irrespective of their water contents.

The hydrous trachytes and phonolites that have been studied in the high viscosity range are equivalent when the isokom temperature is plotted against the inverse of TAS\* parameter (Fig. 6.7). This indicates that as long as such compositions are considered, the TAS\* parameter is sufficient to explain the different hydrous viscosities in Fig. 6.6. This is despite the relatively large compositional differences, with total FeO ranging from 2.90 (MNV) to 4.80 wt% (Ves1631), CaO from 0.7 (Td\_ph) to 6.8 wt% (Ves1631), MgO from 0.2 (MNV) to 1.8 (Ves1631) (Romano et al., 2002, and Table 1). Conversely, dry viscosities ( $w_{H_2O} < 0.3$  wt%, or 0.6 wt% for Td\_ph) lie outside the hydrous trend, with a general tendency to increase with  $1/TAS^*$  although AMS and MNV liquids show significant deviations (Fig. 6.7).

The curves shown by rhyolite and basalt in Fig. 6.7 are very different from those of trachytes and phonolites, indicating that there is a substantial difference between their structures. A guide parameter is the NBO/T value, which represents the ratio of non-bridging oxygens to tetrahedrally coordinated cations, and is related to the extent of polymerisation of the melt (Mysen, 1988). Stebbins and Xu (1997) pointed out that NBO/T values should be regarded as an approximation of the actual structural configuration of silicate melts, since non-bridging oxygens can still be present in nominally fully polymerised melts. For rhyolite the NBO/T value is zero (fully polymerised), for trachytes and phonolites it ranges from 0.04 (IGC) to 0.24 (Ves1631), and for the Etnean basalt it is 0.47. Therefore, the range of polymerisation conditions covered by trachytes and phonolites in the present paper is rather large, with the IGC sample approaching the fully polymerisation typical of rhyolites. While the very low NBO/T value of IGC is consistent with the fact that it shows the largest viscosity drop with addition of water to the dry liquid among the trachytes and the phonolites (Figs. 6.4-6.6), it does not help to understand the similar behaviour of all hydrous trachytes and phonolites in Fig. 6.7, compared to the very different behaviour of rhyolite (and basalt). It is also worth noting that rhyolite, trachytes, and phonolites show similar slopes in Fig. 6.7, while the Etnean basalt shows a much lower slope with its curve crossing the curves for all the other compositions. This crossover is related to that shown by ETN in Fig. 6.6.

## **6.5. Conclusions.**

The dry and hydrous viscosity of natural trachytic liquids that represent the glassy portion of pumice samples from eruptions of Phlegrean Fields have been determined. The parameters of a modified TVF equation that allows viscosity to be calculated for each composition, as a function of temperature and water content have been calibrated. The viscosities of natural trachytic liquids fall between those of natural phonolitic and rhyolitic liquids, consistent with the dominantly explosive eruptive style of Phlegrean Fields volcano, compared to the similar style of rhyolitic volcanoes, the mixed explosive-effusive style of phonolitic volcanoes, such as Vesuvius, and the dominantly effusive style of basaltic volcanoes which are associated with the lowest viscosities among those considered in this work. Variations in composition between the trachytes translate into differences in liquid viscosity of nearly two orders of magnitude at dry conditions, and less than one order of magnitude at hydrous conditions. Such differences can increase significantly when the estimated eruptive temperatures of different eruptions at Phlegrean Fields are taken into account.

Particularly relevant in the high viscosity range is that all hydrous trachytes and phonolites become indistinguishable when the isokom temperature is plotted against the reciprocal of the compositional parameter, TAS\*. In contrast, rhyolitic and basaltic liquids show distinct behaviour.

For hydrous liquids in the low viscosity range, or for temperatures close to those of natural magmas, the uncertainty of the calculations is large although it cannot be quantified, due to a lack of measurements in these conditions. Although special care has been taken in the regression procedure in order to obtain physically consistent parameters, the large uncertainty represents a limitation to the use of the results for the modelling and interpretation of volcanic processes. Future improvements are required to develop and standardize the employment of experimental techniques that determine the hydrous viscosities in the intermediate to high temperature range.

## 7. Conclusions

Newtonian viscosities of silicate liquids were investigated in a range between  $10^{-1}$  to  $10^{11.6}$  Pa s and parameterised using the non-linear TVF equation. There are strong numerical correlations between parameters ( $A_{TVF}$ ,  $B_{TVF}$  and  $T_0$ ) that mask the effect of composition. Wide ranges of  $A_{TVF}$ ,  $B_{TVF}$  and  $T_0$  values can be used to describe individual datasets. This is true even when the data are numerous, well-measured and span a wide range of experimental conditions.

It appears that strong non-Arrhenian datasets have the greatest leverage on compositional dependencies. Strong liquids place only minor restrictions on the absolute ranges of  $A_{TVF}$ ,  $B_{TVF}$  and  $T_0$ . Therefore, strategies for modelling the effects on compositions should be built around high-quality datasets collected on non-Arrhenian liquids. As a result, viscosity of a large number of natural and synthetic Arrhenian (haplogranitic composition) to strongly non-Arrhenian (basanite) silicate liquids have been investigated.

Undersaturated liquids have higher  $T_0$  values and lower  $B_{TVF}$  values, contrary to SiO<sub>2</sub>-rich samples.  $T_0$  values (0-728 K), that vary from strong to fragile liquids, show a positive correlation with the NBO/T ratio. On the other hand, glass transition temperatures are negatively correlated to the NBO/T ratio and show only a small deviation from 1000 K, with the exception of pure SiO<sub>2</sub>.

On the basis of these relationships, kinetic fragilities ( $F$ ), representing the deviation from Arrhenian behaviour, have been parameterised for the first time in terms of composition:

$$F = -0.0044 + 0.6887 * [1 - \exp(-5.4767 * \text{NBO}/T)]$$

Initial addition of network modifying elements to a fully polymerised liquid (i.e. NBO/T=0) results in a rapid increase in  $F$ . However, at NBO/T values above 0.4-0.5 further addition of a network modifier has little effect on fragility. This parameterisation indicates that this sharp change in the variation of fragility with NBO/T is due to a sudden change in the configurational properties and rheological regimes, owing to the addition of network modifying elements.

The resulting TVF parameterisation has been used to build up a predictive model for Arrhenian to non-Arrhenian melt viscosity. The model accommodates the effect of composition via an empirical parameter called here the “structure modifier” (SM). SM is the summation of molar oxides of Ca, Mg, Mn, half of the total iron  $Fe_{\text{tot}}$ , Na and K. The model

reproduces all the original data sets within about 10% of the measured values of  $\log \eta$  over the entire range of composition in the temperature interval 700-1600 °C according to the following equation:

$$\log_{10} \eta = c_1 + \frac{c_2 * c_3}{c_3 + SM}$$

where  $c_1$ ,  $c_2$ ,  $c_3$  have been determined to be temperature-dependent

$$c_1 = [-17.80106 + 0.01808103 \cdot T(^{\circ}\text{C})] / (1 - 2.2869 \cdot 10^{-3} \cdot T(^{\circ}\text{C}))$$

$$c_2 = \frac{1}{[0.02532 + 2.5124 \cdot \exp(-6.3679 \cdot 10^{-3} \cdot T(^{\circ}\text{C})) + 40.4562 \cdot 10^{-6} \cdot T(^{\circ}\text{C})]}$$

$$c_3 = [1 - 1.6569 \cdot 10^{-3} \cdot T(^{\circ}\text{C})] / [0.017954 - 63,90597 \cdot 10^{-6} \cdot T(^{\circ}\text{C})]$$

The combination of calorimetric and viscosimetric data has enabled a simple expression to be used to predict shear viscosity at the glass transition. The basis for this stems from the equivalence of the relaxation times for both enthalpy and shear stress relaxation in a wide range of silicate melt compositions (Gottsmann et al., 2002). A shift factor that relates cooling rate data with viscosity at the glass transition appears to be slightly dependent on the melt composition.

The effect of water content on decreasing the viscosity of silicate melts has also been parameterised using a modified TVF expression (Giordano et al., 2000). The viscosities of basalts are shown to be lower than those of phonolites; whereas the viscosity of natural trachytes are higher than that of phonolites, but lower than that of rhyolites. This is consistent with the style of eruption associated with these compositions, with trachytes generating eruptions that are dominantly explosive (e.g. Phlegrean Fields volcano), compared to the highly explosive style of rhyolitic volcanoes, the mixed explosive-effusive style of phonolitic volcanoes (e.g. Vesuvius) and the dominantly effusive style of basalts. Variations in composition between the trachytes translate into differences in liquid viscosity of nearly two orders of magnitude in dry conditions, and less than one order of magnitude in hydrous

conditions. These differences increase significantly when the estimated eruptive temperatures of different eruptions at Phlegrean Fields are taken into account.

At temperatures close to those of natural magmas and in the case of low viscosity hydrous liquids the uncertainty of the calculations is large, although it cannot be quantified, due to a lack of measurements under these conditions.

## 8. Outlook

A future objective will be to discover if it is possible to define a single value for the high-T limiting value of  $\log [\eta]$  (e.g.  $A_{TVF}$ ) for a large number of natural and synthetic systems. The corollary to this would be to assign all compositional effects to the parameters  $B_{TVF}$  and  $T_0$ . Furthermore, it appears that non-Arrhenian datasets have the greatest leverage on compositional dependencies. Strong liquids that exhibit near Arrhenian behaviour place only minor restrictions on the absolute ranges of values of  $A_{TVF}$ ,  $B_{TVF}$  and  $T_0$ . Therefore, strategies for modelling the effects of composition should be built around high quality datasets collected from non-Arrhenian melts. A large dataset will be needed to define the high-T limiting value of  $\log [\eta]$ , which will require new rheological measurements.

Such measurements would also be useful in order to interpret the results obtained in section 5.2, which permitted the identification of the chemical constraints on the empirical quantities of the TVF law (that describes the viscosity of silicate melts). Interpretation of the TVF temperature will be described in the light of these new data. The capability of single oxide-components to play different roles within a multi-component structure could also be investigated.

Test of the empirical model here described must be extended to larger compositional range.

The results obtained for dry and hydrous samples must be considered carefully in future investigations. In particular, the effect that the addition of a structure modifier has on the TVF temperature of dry liquids ( $T_0$  increases with addition of modifier cations), which is opposite to the effect of water, which also is a modifier. This indicates that it is necessary to understand whether this is due solely to the presence of water or if it is due to the use of regression laws to describe the viscosity of these liquids that are (conceptually) incorrect.

To solve this problem a large number of measurements must be performed systematically at conditions relevant for volcanic eruptions between viscosities of  $10^5$  to  $10^{8.5}$  Pas. This may be performed using a modified falling sphere method integrated by a centrifuge apparatus (Dorfmann et al., 1996).

The rheology of silicate melts containing of other volatile species (e.g.  $\text{CO}_2$ , F, Cl), should be investigated along with the rheology of multiphase (liquid+vesicles+crystals) systems that are relevant to volcanic scenarios.

## 9. Appendices

### *Appendix I: Computation of confidence limits*

I have used the minimization of the  $\chi^2$  function (Eq. 5.1) to obtain estimates of the TVF parameters,  $a_j$  ( $j=1, m$ ) for a set of  $n$  measurements ( $y_i$ ;  $i=1, n$ ). Essentially this is a weighted least-squares process where the weighting scheme depends on estimates of the measurement uncertainties (e.g.  $\sigma_i$ ; Tables 3 and 6). The  $\chi^2$  minimization strategy provides a means of establishing confidence limits for the values of the model parameters. This is performed by mapping boundaries of constant  $\chi^2$  (values of  $\Delta\chi^2$ ) around the optimal solution in the manner described by Press et al. (1986). These confidence limits provide objective estimates of the uncertainties for the model parameters based on the quality and distribution relative to the model equation (e.g. Russell and Hauksdóttir, 2001; Russell et al., 2001). Specifically, this strategy is used to portray the full range of TVF parameters that must be considered to be consistent with the experimental data. The projected confidence limits on the model parameters (e.g. Figs. 5.4, 5.7 and 5.10) represent linear approximations to the  $\chi^2$  solution surface; near the solution the linear model is indistinguishable from the actual  $\chi^2$  surface.

Operationally, the following calculations (e.g. Press et al., 1986) were employed. Establish the optimal fit by solving for the minimum  $\chi^2$  (e.g.  $\chi^{2,\min}$ ). Compute the value  $\Delta\chi^2$  ( $\chi^{2,*} - \chi^{2,\min}$ ) where the value of  $\chi^{2,*}$  depends on the degrees of freedom ( $n-m$ ) and the confidence level of interest (e.g. 95 %). The matrix  $\alpha$  ( $m \times m$ ) is then calculated for the  $\chi^{2,\min}$  fit from:

$$\alpha_{k,l} = \sum_{i=1}^n \frac{1}{\sigma_i} \begin{bmatrix} \partial y_i^* \partial y_i^* \\ \partial a_k \partial y_l \end{bmatrix} \quad (\text{A-1})$$

where  $\alpha_{k,l}$  are the individual entries on the matrix and  $y_i^*$  denotes the values of the functions predicted by the model. The covariance matrix (C) to the problem is then calculated from  $\alpha^{-1}$ .

The constant  $\chi^2$  boundaries (confidence limits) are computed from the matrix equation:

$$\Delta\chi^2 = \mathbf{p} \cdot [\alpha] \cdot \mathbf{p} \quad (\text{A-2})$$

where  $\mathbf{p}$  is an  $m$ -component vector that describes the position of the confidence limits relative to the optimal solution. For a 3-parameter problem, Eq. A-2 describes a 3-D ellipsoid.

The confidence limits as 2-D ellipses resulting from the projection of the entire 3-D ellipsoid onto a single plane (e.g. Figs. 5.4, 5.7 and 5.10) were portrayed. These ellipses are calculated from:

$$\Delta\chi^2 = \mathbf{r} \cdot [\mathbf{C}_p]^{-1} \cdot \mathbf{r} \quad (\text{A-3})$$

where  $\mathbf{C}_p$  is the 2 x 2 submatrix of  $\mathbf{C}$  containing rows and columns of the parameters of interest (e.g.  $A_{TVF}$  and  $B_{TVF}$  or  $B_{TVF}$  and  $T_\theta$ ). The unknowns to this matrix equation are the two components of the relative displacement vector  $\mathbf{r}$  (e.g.  $r_x$  and  $r_y$ ). In its quadratic form, Eq. A-3 becomes:

$$r_x^2 \cdot C_{p_{1,1}} + r_x r_y \cdot C_{p_{1,2}} + r_y^2 \cdot C_{p_{2,2}} = \Delta\chi^2 \quad (\text{A-4})$$

The coordinates to the ellipse are computed by fixing one unknown (e.g.  $r_y$ ) and solving the roots of the resulting equation. Given arbitrary values of  $r_y$ , the values of  $r_x$  are computed from:

$$r_x^2 = \frac{r_y \cdot C_{p_{1,2}} \pm \sqrt{(r_y \cdot C_{p_{1,2}})^2 - C_{p_{1,1}} \cdot (r_y^2 \cdot C_{p_{2,2}} - \Delta\chi^2)}}{C_{p_{1,1}}} \quad (\text{A-5})$$

Coordinate pairs across the minimum and maximum range of values for  $r_y$  are established using the relationship:

$$r_y = \pm \sqrt{\frac{-C_{p_{1,1}} \cdot \Delta\chi^2}{C_{p_{1,2}}^2 - C_{p_{1,1}} \cdot C_{p_{2,2}}}} \quad (\text{A-6})$$

These 2-D projections of the ellipsoids are linear approximations to the shadow cast by the entire 3-D confidence envelope onto this 2-dimensional plane. Axis-parallel tangents to these ellipses establish the maximum range of parameter values that are supported by the data at the specified confidence limits.

A second set of confidence limits (e.g. smaller ellipses in Fig. 5.4) have been calculated. These represent the confidence limits for two parameters, where the 3<sup>rd</sup> parameter is fixed at

the optimal solution. These ellipses are computed in exactly the same way as described above, except that the projection matrix  $C_p$  in Eq. A-3 is calculated from:

$$C_p = [\alpha_p]^{-1} \quad (\text{A-7})$$

where the matrix  $\alpha_p$  is a 2 x 2 submatrix of  $\alpha$  comprising the rows and columns of the parameters that are not fixed (parameters that constitute the plane of projection). For example, in Fig. 5.4 a, the small ellipse represents the intersection of the plane  $T_0 = 359$  with the 3-D ellipsoid. It shows the range of permitted values of  $A_{TVF}$  and  $B_{TVF}$  (and the apparent correlation) at this fixed value of  $T_0$ .

## 10. References

- Ablay, G.J., Ernst, G.G.J., Marti, J. and Sparks, R.S.J. (1995). The ~ 2 ka subplinian eruption of Montana Blanca, Tenerife. *Bull. Volcanol.* 57, 337-355.
- Adam, G. and Gibbs, J.H. (1965). On the temperature dependence of cooperative relaxation properties in glass-forming liquids. *Journal of Chemical Physics* 43, 139-146.
- Angell, C.A. (1985). Strong and fragile liquids. In K.L. Ngai and G.B. Wright, Eds., *Relaxations in complex systems*, p. 3-11. U.S. Department of Commerce National Technical Information Service, Springfield, Virginia.
- Angell, C.A. (1988). Structural instability and relaxation in liquid and glassy phases near the fragile liquid limit. *J. Non-Cryst. Solid*, 102, 205-221.
- Angell, C.A. (1988): Perspectives on the glass transition. *J. Physics Chemistry Solids*, 49, 863-871.
- Angell, C.A. (1995). Formation of Glasses from Liquids and Biopolymers. *Science* 265, 1924-1935.
- Angell, C. A. (1997). Entropy and fragility in supercooled liquids. *J. Res. NIST* 102, 171-185.
- Baker, D.R. (1996): Granitic melt viscosities: Empirical and configurational entropy models for their calculation. *Am. Mineral.*, 81, 126-134.
- Behrens, H. (1995). Determinations of water solubilities in high-viscosity melts: an experimental study of NaAlSi<sub>3</sub>O<sub>8</sub> and KAlSi<sub>3</sub>O<sub>8</sub>. *Eur. J. Mineral.* 7, 905-920.
- Behrens, H., Romano, C., Nowak, M., Holtz, F., Dingwell, D.B., (1996) Near-infrared spectroscopic determination of water species in glasses of the system MAlSi<sub>3</sub>O<sub>8</sub> (M= Li, Na, K): an interlaboratory study. *Chem. Geol.* 128, 41-63.
- Böhmer, R. and Angell, C.A. (1992). Correlations of the nonexponentiality and state dependence of mechanical relaxations with bond connectivity in Ge-As-Se supercooled liquids. *Phys. Rev.* 45, 10091-10094.
- Bottinga, Y. and Weill, D. (1972). The viscosity of magmatic silicate liquids: a model for calculation. *Am. Jour. Sci.* 272, 438-475.
- Bottinga, Y., Richet, P., Sipp, A. (1995). Viscosità regimes of homogeneous silicate melts. *Am. Mineral.* 80, 305-318.
- Carroll, M. and Blank, J. (1997) The solubility of water in phonolitic melts. *Am. Mineral.* 82, 549-556.

- Civetta, L., Carluccio, E., Innocenti, F., Sbrana, A., Taddeucci, G. (1991). Magma chamber evolution under Phlegrean Fields during the last 10 ka: trace element and isotope data. *Eur. J. Mineral.* 3, 415-428.
- Cohen, M.H. and Grest, G.S. (1979). Liquid-glass transition, a free volume approach. *Phys. Rev.* 20, 1077-1098.
- Cooney, T., Sharma, S.K., Urmos, J.P. (1987). Structure of glasses along the join forsterite-fayalite and tephroite-fayalite (abstract). *EOS*, 68, 436.
- Cranmer, D. & Uhlmann, D.R. (1981): Viscosities in the system albite-anorthite. *J. Geophys. Res.*, 86, 7951-7956.
- Cukierman, M. and Uhlmann, D.R. (1974). Effect of iron oxidation state on viscosity, lunar composition 1555. *J. Geophys. Res.* 79, 1594-1598.
- De Bolt, M.A., Easteal, A.J., Macero, P.B. and Moynihan, C.T. (1976). Analysis of structural relaxation in glass using rate heating data. *J. Am. Ceram. Soc.* 59, 16-21.
- de Vita, S. Orsi, G., Civetta, A., Carandente, A., D'Antonio, M., Deino, A., di Cesare, T., Di Vito, M.A., Fischer, R.V., Isaia, R., Marotta, E., Necco, A., Ort, M., Pappalardo, L., Piochi, M., Southon, J. (1999). The Agnano Monte Spina eruption (4100 years BP) in the restless Campi Flegrei caldera (Italy). *J. Volcanol. Geoth. Res.* 91, 269-301
- Dingwell, D.B. (1986). Viscosity-temperature relationships in the system  $\text{Na}_2\text{Si}_2\text{O}_5\text{-Na}_4\text{Al}_2\text{O}_5$ . *Geochim. Cosmochim. Acta* 10, 1261-1265.
- Dingwell, D.B. (1987). Melt viscosities in the system  $\text{NaAlSi}_3\text{O}_8\text{-H}_2\text{O-F}_2\text{O}^{-1}$ . In B.O. Mysen. Ed. Dingwell D.B., (1987) Melt viscosities in the system  $\text{NaAlSi}_3\text{O}_8\text{-H}_2\text{O-F}_2\text{O}^{-1}$ . In B.O. Mysen. Ed., *Magmatic processes: physicochemical principles*, 423-433. The *Geochem. Soc. Spec. Pub.*No. 1.
- Dingwell, D.B. (1989a) The effect of fluorine on the viscosity of diopside melt. *Am. Mineral.* 74, 333-338.
- Dingwell, D.B. (1989b). Shear viscosities of ferrosilicate liquids. *Am. Mineral.* 74, 1038-1044.
- Dingwell, D.B. (1991). Redox viscometry of some Fe-bearing silicate liquids. *Am. Mineral.* 76, 1560-1562.
- Dingwell, D.B. (1993): Experimental strategies for the determination of granitic melt properties at low temperature. *Chem. Geol.* 108, 19-30.
- Dingwell, D.B. (1995). Relaxation in silicate melts: Some Applications, in: *Structure, Dynamics & Properties of Silicate Melts*, (Eds. J.F. Stebbins, P.F. McMillan & D.B. Dingwell). *Rev. Mineral.* 32, 21-66.

- Dingwell, D.B. (1996). Volcanic dilemma: flow or blow? *Science*, 273, 1054-1055.
- Dingwell, D.B. (1998). Magma degassing and fragmentation. Recent experimental advances, in: J.S. Gilbert, R.S.J. Sparks (Eds.), *The Physics of Explosive Volcanic Eruptions*, Special Publications, Geological Society, London, 145, pp. 9-26.
- Dingwell, D.B. (2001). Explosive volcanism. (submitted to *Am. Rev. Earth Planet. Sci.*)
- Dingwell, D.B and Virgo, D. (1987). The effect of oxidation state on the viscosity of melts in the system  $\text{Na}_2\text{O-FeO-Fe}_2\text{O}_3\text{-SiO}_2$ . *Geochim. Cosmochim. Acta* 51, 195-205.
- Dingwell, D.B. and Virgo, D. (1988) Melt viscosities in the  $\text{Na}_2\text{O-FeO-Fe}_2\text{O}_3\text{-SiO}_2$  system and factors controlling the relative viscosities of fully polymerized silicate melts. *Geochim. Cosmoch. Acta* 52, 395-403.
- Dingwell, D.B. and Webb, S.L. (1990). Relaxation in silicate melts. *Eur. J. Mineral.* 2, 427-449.
- Dingwell, D.B., Knoche, R. and Webb, S.L. (1993). The effect of  $\text{P}_2\text{O}_5$  on the viscosity of haplogranitic liquid. *Eur. J. Mineral.* 5, 133-140.
- Dingwell, D.B., Bagdassarov, N.S., Bussod, G.Y., Webb, S.L. (1993). *Magma Rheology. Short Course Handbook on Experiments at High Pressure and Applications to Earth's Mantle*, 21, Luth, R.H. eds.
- Dingwell, D.B., Romano, C., Hess, K.U., (1996) The effect of water on the viscosity of a haplogranitic melt under P-T-X conditions relevant to silicic volcanism. *Contrib. Mineral. Petrol.* 124, 19-28.
- Dingwell, D.B., Hess K.U., Romano, C. (1998a) "Viscosity data for hydrous peraluminous granitic melts: Comparison with a metaluminous model". *Am. Mineral.* 83, 236-239.
- Dingwell, D.B., Hess K.U., Romano, C. (1998b). Extremely fluid behaviour of hydrous peralkaline rhyolites. *Earth and Planet. Sci. Lett.* 158, 31-38.
- Di Vito, M.M., Isaia, R. Orsi, G., Southon, J., de Vita, S., D'Antonio, M., Pappalardo, L. and Piochi, M. (1999). Volcanism and deformation since 12,000 years at the Campi Flegrei caldera (Italy). *J. Volcanol. Geoth. Res.* 91, 221-246
- Dixon, P.K. and Nagel, S.R. (1988). *Phys. Rev. Lett.* 61, 341-350.
- Dixon, J. E., Stolper, E. M., Holloway, J. R. (1995). An experimental study of water and carbon dioxide solubilities in Mid-Ocean Ridge Basaltic liquids. Part I: calibration and solubility models. *J. Petrol.* 36, 1607-1631
- Dorfman, A., Hess, K.U., Dingwell, D.B. (1996). Centrifuge-assisted falling-sphere viscometry. *Eur. J. Mineral.* 8, 507-514.
- Eyring, (1936). Absolute rate theory. *Jour. Chem. Phys.* 3, 340-375.

- Fulcher, G.S. (1925): Analysis of recent measurements of the viscosity of glasses. *Am. Ceramic Soc. J.* 8, 339-355.
- Gaillard, F., Scaillet, B., Pichavant, M., Beny, J.M. (2001). The effect of water and fO<sub>2</sub> on the ferric-ferrous ratio of silicic melts. *Chem. Geol.* 174, 255-273.
- Ghiorso, M.S. & Sack, R.O. (1995): Chemical Mass Transfer in Magmatic Processes IV: A revised and internally-consistent thermodynamic model for the interpolation and extrapolation of liquid-solid equilibria in magmatic systems at elevated temperatures and pressures. *Contrib. Mineral. Petrol.* 119, 197-212.
- Gibbs, J.H. and Di Marzio, E.A. (1958). Nature of glass transition and the glassy state. *J. Chem. Phys.* 28, 373-383.
- Giordano, D., Dingwell, D.B. (2002 a). Viscosity of hydrous Etna basalt: implications for Plinian-style basaltic eruptions. *Bull. Volcanol.* in press.
- Giordano, D., Dingwell, D.B. (2002 b). Toward a multicomponent model for the non-arrhenian temperature-dependence of volcanic melts. Submitted to *Earth Planet. Sci. Lett.*
- Giordano, D., Dingwell D.B. and Romano C. (2000) "Viscosity of a Teide phonolite in the welding interval. *J. Volcanol. Geoth. Res.* 103, 239-245.
- Giordano, D., Romano, C., Papale, P., Dingwell, D. B.(2002). Viscosity of trachytes from Phlegrean Fields, and comparison with basaltic, phonolitic, and rhyolitic melts. Submitted to *J. Volcanol. Geotherm. Res.*
- Glastone, S., Laidler, K.J., Eyring, H. (1941). *The theory of rate processes.* 486 p McGraw-Hill, New York.
- Götze, W. (1991). Aspects of structural glass transitions. In J.P. Hansen, D. Levesque, and J. Zin-Justin, Eds., *Liquids, freezing, and the glass transition*, Volume 1, 292-503.
- Gottsmann, J. and Dingwell, D.B. (2000). The cooling history of sub-marine vitrophyres: a preliminary calorimetric study on drill cores of the HSDP. *Eos* 81, 1348.
- Gottsmann, J. and Dingwell, D.B. (2001a). Cooling dynamics of spatter-fed phonolite obsidian flows on Tenerife, Canary Islands. *J. Volcanol. Geoth. Res.* 105, 323-342.
- Gottsmann, J. and Dingwell, D.B. (2001b). The cooling of frontal flow ramps: A calorimetric study on the Rocche Rosse rhyolite flow, Lipari, Aeolian Islands, Italy. *Terranova* 13, 157-164.
- Gottsmann, J. and Dingwell, D.B. (2002). The thermal history of a spatter-fed lava flow: the 8-ka pantellerite flow on Major Island, New Zealand. *Bull. Volcanol.*, in press.

- Gottsmann, J., Giordano, D. and Dingwell, D.B. (2001). Predicting shear viscosity at the glass transition during volcanic processes: a calorimetric calibration. *Earth Planet. Sci. Lett.*, in press.
- Hess, K.U., Dingwell, D.B. & Rossler, E. (1996). Parameterisation of viscosity-temperature relations of aluminosilicate melts. *Chem. Geol.* 128, 155-163.
- Hess, K.U., Dingwell, D.B., Webb, S.L., (1995). The influence of excess alkalis on the viscosity of a haplogranitic melt. *Am. Mineral.* 80, 297-304.
- Hess, K.U., Dingwell, D.B. (1996). Viscosities of hydrous leucogranitic melts: A non-Arrhenian model. *Am. Mineral.* 81, 1297-1300.
- Hess, K-U. (1996) Zur Temperaturabhängigkeit der Viskosität von haplogranitischen Schmelzen. Doctoral Thesis, University of Bayreuth (in German).
- Hess, K.U., Dingwell, D.B., Gennaro, C., Mincione, V. (2001). Viscosity-temperature behaviour of dry melts in the Qz-Ab-Or system. *Chem. Geol.* 174, 133-142.
- Holtz, F., Behrens, H., Dingwell, D.B., Taylor, R.P. (1992). Water solubility in aluminosilicate melts of haplogranitic compositions at 2 kbar. *Chem. Geol.* 196, 289-302.
- Holtz, F., Dingwell, D.B., Behrens, H. (1993). Effects of F, B<sub>2</sub>O<sub>3</sub> and P<sub>2</sub>O<sub>5</sub> on the solubility of water in haplogranitemelts compared to natural silicate melts. *Contrib. Mineral. Petrol.* 113, 492-501.
- Holtz, F., Behrens, H., Dingwell, D.B., Johannes, W. (1995). H<sub>2</sub>O solubility in haplogranitic melts: compositional, pressure and temperature dependence. *Am. Mineral.* 80, 94-108.
- Hummel, W. and Arndt, J. (1985): Variation of viscosity with temperature and composition in the plagioclase system. *Contrib. Mineral. Petrol.* 90, 83-92.
- Ihinger, P.D., Hervig, R.L., McMillan, P.F. (1994). Analytical methods for volatiles in glasses. In: M.R. Carroll and J.R. Holloway (Editors), *Volatiles in Magmas. Reviews in Mineralogy*, Mineralogical Society of America, Washington, D.C., pp. 67-121.
- Ito, K., Cornelius, T., Moynihan, C.T. and Angell, C.A (1999). Thermodynamic determination of fragility in liquids and fragile-to-strong liquid transition in water. *Nature* 398, 492-495.
- Kauzmann, W. (1948). The nature of the glassy state and the behaviour of liquids at low temperature. *Chem. Rev.* 43, 219-256
- Kohn, S.C. (2000): The dissolution mechanisms of water in silicate melts: A synthesis of recent data. *Mineral. Mag.* 64, 389-408.

- Kushiro, I. (1975). On the nature of silicate melt and its significance in magma genesis: regularities in the shift of liquidus boundaries involving olivine pyroxene, and silica materials. *Am. J. Sci.* 275, 411-431.
- Lange, R.A and Navrotsky, A. (1992). Heat capacity of Fe<sub>2</sub>O<sub>3</sub>-bearing silicate liquids. *Contrib. Mineral. Petrol.* 110, 311-320.
- Lange, R.A and Navrotsky, A. (1993). Heat capacities of TiO<sub>2</sub>-bearing silicate liquids: evidence for anomalous changes in configurational entropy with temperature. *Geochim. Cosmochim. Acta* 57, 3001-3011.
- Le Bas, M.J., Le Maitre, R.W., Streckeisen, A. and Zanetti, R. (1986). A chemical classification of volcanic rocks based on the total-alkali-silica diagram. *Journal of Petrology* 27, 745-750.
- Lejeune, A.M. and Richet, P., (1995). Rheology of crystal-bearing melts. *J. Geophys. Res.* 100, B3, 4215 – 4229.
- Litovitz, T.A. (1960). Liquid relaxation phenomena and the glass state. *J. non-Cryst. Solids*, edited by V.N. Frechette, pp.252-268, John Wiley
- Liska, M., Simurka, P., Antalík, J., Perichta, P. (1996). Viscosity of titania-bearing silicate melts. *Chem. Geol.* 128, 199-206.
- Marsh, B.D. (1981). On the crystallinity, probability of occurrence, and rheology of lava and magma. *Contrib. Mineral. Petrol.* 78, 85-98.
- Martinez, L.-M. and Angell, C. A. (2001). A thermodynamic connection to the fragility of glass-forming liquids. *Nature*, 5 April 2001.
- Maxwell, J.C. (1867). On the dynamical theory of gases. *Phil. Trans. Roy. Soc. Londo*, Ser. A, 157, 49-88.
- Miller, A.A. (1978). *Macromolecules* 11, 859.
- Moynihan, C.T. (1995). Structural relaxation in the glass transition. In: J.F. Stebbins, P.W. McMillan and D.B. Dingwell (Editors), *Structure, Dynamics and Properties of Silicate Melts*. Reviews in Mineralogy, Mineralogical Society of America, Washington, D.C., pp. 1-19.
- Mysen, B.O, Ryerson, F.J., Virgo, D. (1980). The influence of TiO<sub>2</sub> on structure and derivative properties of silicate melts. *Am. Mineral.* 65, 1150-1165.
- Mysen, B.O, Virgo, D., Seifert, F.A. (1985). Relationships between properties and structure of aluminosilicate melts. *Am. Mineral.* 70, 88-105.
- Mysen, B.O. (1988). *Structure and properties of Silicate Melts*. Elsevier, Amsterdam, 354 pp.

- Narayanswamy, O.S. (1988). Thermorheological simplicity in the glass transition. *J. Am. Ceram. Soc.* 71, 900-904.
- Navrotsky, A., Hon, R., Weill, D.F., Henry, D.J. (1980). Thermochemistry of glasses and liquids in the system  $\text{CaMgSi}_2\text{O}_6$ - $\text{CaAl}_2\text{Si}_2\text{O}_6$ - $\text{NaAlSi}_3\text{O}_8$ ;  $\text{SiO}_2$ - $\text{CaAl}_2\text{Si}_2\text{O}_8$ - $\text{NaAlSi}_3\text{O}_8$  and  $\text{SiO}_2$ - $\text{Al}_2\text{O}_3$ - $\text{CaO}$ - $\text{Na}_2\text{O}$ . *Geochim. Cosmochim. Acta* 44, 1409-1433.
- N'Dala, I., Cambier, F., Anseau, M.R., Urbain, G. (1984): Viscosity of liquid feldspars Part 1: Viscosity measurements. *British Ceramic Trans. J.* 83, 105-107.
- Neuville, D.R., Courtial, P., Dingwell, D.B., Richet, P. (1993). Thermodynamic and rheological properties of rhyolite and andesite melts. *Contrib. Mineral. Petrol.* 113, 572-581.
- Newmann, S., Stolper, E.M., Epstein, S. (1986). Measurement of water in rhyolitic glasses: calibration of an infrared spectroscopic technique. *Am. Mineral.* 71, 1527-1541.
- Ngai, K.L. and Wright, G.B (eds) Office of Naval Research and National Technical Information Service.
- Ohlhorst, S., Behrens, Holtz, F. (2001). Compositional dependence of molar absorptivities of near-infrared OH- and  $\text{H}_2\text{O}$  bands in rhyolitic to basaltic glasses. *Chem. Geol.* 174, 5-20.
- Papale, P. and Dobran, F. (1994). Magma flow along the volcanic conduit during the plinian and pyroclastic flow phases of the may 18, 1980, mount st. helens eruption. *J. Geophys. Res.* 99, 4355-4373.
- Papale, P. (1999). Strain-induced magma fragmentation in explosive eruptions. *Nature* 397, 425-428.
- Persikov, E.S.; Zharikov, V.A., Bukhtiyarov, P.G., Pol'skoy, S.F. (1990). The effect of volatiles on the properties of magmatic melts. *Eur. J. Mineral.* 2, 621-642.
- Persikov, E.S. (1991) The viscosity of magmatic liquids: experiment, generalized patterns. A model for calculation and prediction. Applications. In *Adv. Phys. Geochem.* 9, 1-40.
- Pinkerton, H and Stevenson, R.J. (1992). Methods of determining the rheological properties of magmas at sub-liquidus temperatures. *J. Volcanol. Geoth. Res.* 53, 47-66.
- Plazek, D.J. and Ngai, K.L. (1991). Correlation of polymer segmental chain dynamics with temperature-dependent time-scale shifts. *Macromolecules* 24, 1222-1224.
- Pocklington, H.C. (1940). Rough measurement of high viscosities. *Proceedings of the Cambridge Philosophical Society* 36, 507-508.
- Press, W.H., Flannery, B.P., Teukolsky, S.A. and Vetterling, W.T. (1986). *Numerical recipes. The art of scientific computing*, 818pp. Cambridge University Press, New York.

- Prusevich, A.A. (1988): Refinement of calculation of viscosity of magmatic melts according to their chemical composition. *Geologiya i Geofizika* 29, 67-69.
- Richet, P. (1984) Viscosity and configurational entropy of silicate melts. *Geochimica et Cosmochimica Acta* 48, 471-483.
- Richet, P. and Bottinga, Y. (1985) Heat capacity of aluminium-free liquid silicate. *Geochim Cosmochim. Acta* 49, 471-486.
- Richet, P. Robie, R.A. and Hemingway, B.S. (1986). Low-temperature heat capacity of diopside glass ( $\text{CaMgSi}_2\text{O}_6$ ): a calorimetric test of the configurational-entropy theory applied to the viscosity of liquid silicates. *Geochim Cosmochim. Acta* 50, 1521-1533.
- Richet, P. and Bottinga, Y. (1986) Thermochemical properties of silicate glasses and liquids: a review. *Rev. Geophys.* 24, 1-25.
- Richet, P. Robie, R.A. and Hemingway, B.S. (1993). Entropy and structure of silicate glasses and melts. *Geochim. Cosmochim. Acta* 57, 2751-2766.
- Richet, P. and Bottinga, Y. (1995). Rheology and configurational entropy of silicate melts. In *Structure, Dynamics and Properties of Silicate Melts*, (Eds. J.F. Stebbins, P.F. McMillan and D.B. Dingwell), *Rev. in Mineral.* 32, 67-94.
- Riebling, E.F. (1964). Structure of magnesium aluminosilicate liquids at 1700 °C. *Can. J. Chemistry* 42, 2811-2821.
- Riebling, E.F. (1966). Structure of sodium aluminosilicate melts containing at least 50 mole %  $\text{SiO}_2$  at 1500° C. *J. Chem. Phys.* 44, 2857-2865.
- Risbud, et al., 1987;
- Roach, A. and Rutherford, M.J.(2001). Experimental petrology of the trachytes of Agnano Monte Spina, Campi Flegrei, proceedings of the meeting “Frame Programme for the Monitoring and Research Activity on Italian Volcanoes 2000-2002”, Gruppo Nazionale per la Vulcanologia, Roma, 9-11 October 2001: 196-197.
- Rössler, E., Hess, K.U. and Novikov, V.N. (1998). Universal representation of viscosity in glass forming liquids. *J. Non-Cryst. Solids* 223, 207-222.
- Romano, C., Poe, B., Mincione, V., Hess, K.U., Dingwell, D.B., (2000). The viscosities of hydrous  $\text{XAlSi}_3\text{O}_8$  (X=Li, Na, K, Ca0.5, Mg0.5) melts. *Chem. Geol.* 174, 115-132.
- Romano, C., Giordano, D., Papale, P., Mincione, V., Dingwell, D., Rosi, M. (2002). The dry and hydrous viscosities of alkaline melts from Vesuvius and Phlegrean Fields. Submitted to *Chem. Geol.*
- Rosi, M. and Santacroce, R. (1984). Volcanic hazard assessment in the Phlegrean Fields: a contribution based on stratigraphic and historical data. *Bull. Volcanol.* 47, 359-370.

- Rosi, M., Principe, C. and Vecci, R. (1993). The Vesuvius 1631 eruption. A reconstruction based on historical and stratigraphical data. *J. Volcanol. Geoth. Res.* 58, 151-182.
- Rosi, M., Vezzoli, L., Castelmennano, A., Greco, G. (1999). Plinian pomice fall deposit of the Campanian Ignimbrite eruption (Phlegren Fields, Italy). *J. Volcanol. Geoth. Res.* 91, 179-198.
- Rossin, R., Bersain, J., Urbain, G. (1964). Etude de la viscosite de laitiers liquids appartenant au systeme ternaire:  $\text{SiO}_2\text{-Al}_2\text{O}_3\text{-CaO}$ . *Revue Hautes temperatures Refractaires* 1, 159-170.
- Ryerson, F.J. and Hess, P.C. (1980). The role of  $\text{P}_2\text{O}_5$  in silicate melts. *Geochim. Cosmochim. Acta* 44, 611-625.
- Russell, J.K. and Hauksdóttir, S. (2001): Estimates of crustal assimilation in Quaternary lavas from the northern cordillera, British Columbia. *Can. Min.* 39, 361-383.
- Russell, J.K., Dipple, G.M., Kopylova, M.G. (2001): Heat production and heat flow in the mantle lithosphere to the Slave craton, Canada. *Phys. Earth Planet. Int.* 123, 27-44.
- Russell, J.K., Giordano, D., Dingwell, D.B. & Hess, K-U. (2002). Modelling the non-Arrhenian rheology of silicate melts: Numerical considerations. *Eur. J. Mineral.*, 14, 417-427.
- Sato, H., Fugii, T. and Nakada, S. (1992). Crumbling of dacite dome lava and generation of pyroclastic flows at Unzen volcano. *Nature*, 360, 664-666.
- Scamehorn, C. and Angell, C.A. (1991). Viscosity-temperature relations and structure in fully polymerised aluminosilicate melts from ion dynamics simulations. *Geochim. Cosmochim. Acta* 55, 721-730.
- Scandone, R., Bellocci, F., Lirer, L., Rolandi, G. (1991). The structure of the Campanian Plain and the activity of Neapolitan volcanoes (Italy). *J. Volcanol. Geoth. Res.* 48, 1-31.
- Scarfe, C.M. (1986): Viscosity and density of silicate melts. In: *Short Course in Silicate Melts* (Ed. C.M. Scarfe). *Mineralogical Association Canada* 12, 36-56.
- Scarfe, C.M., Cronin, D.J., Wenzel, J.T., Kaufman, D.A. (1983): Viscosity-temperature relationships at 1 atmosphere in the system diopside-anorthite. *Am. Mineral.* 68, 1083-1088.
- Scarfe, C.M., Mysen, B.O., Virgo, D. (1987). Pressure dependence of the viscosity of silicate melts. In: *Magmatic processes: Physicochemical Principles*. *Geochem. Soc. Spec. Pub.* 1, 59-67.

- Scherer, G.W. (1984). Use of the Adam-Gibbs equation in the analysis of structural relaxation. *J. Am. Ceram. Soc.* 67, 504-511.
- Scholze, H. and Kreidl, N.J. (1986). Technological aspects of viscosity. In: D.R. Uhlmann and N.J. Kreidl (Editors), *Glass. Science and Technology*. Academic Press, Inc, London, pp. 233-273.
- Scholze, H. (1960). Zur Frage der Unterscheidung zwischen H<sub>2</sub>O-Molekeln und OH-Gruppen in Gläsern und Mineralen. *Naturwissenschaften* 47, 226-227.
- Schulze, F., Behrens, H., Holtz, F., Roux, J., Johannes, W. (1996) "The influence of H<sub>2</sub>O on the viscosity of a haplogranitic melt" *Am. Mineral.* 81, 1155-1165.
- Sethna, J.P. (1988). *Eur. Phys. Lett.* 6, 529.
- Shaw, H.R. (1963): Obsidian-H<sub>2</sub>O viscosities at 1000 and 2000 bars in the temperature range 700 to 900 °C. *J. Geophys. Res.* 68, 6337-6343.
- Shaw, H. R., (1972). Viscosities of magmatic silicate liquids: an empirical method of prediction. *Am. Jour. Sci.* 272, 870 - 893.
- Sipp, A., Bottinga, Y., Richet, P. (2001). New high viscosity data for 3D network liquids and new correlations between old parameters.
- Sowerby, J.R. and Keppler, H. (1999). Water speciation in rhyolitic melt determined by in-situ infrared spectroscopy. *Am. Mineral.* 84, 1843-1849.
- Stebbins, J.F., Carmichael, L.S.E., Weill, D.F. (1983). The high-temperature liquid and glass heat contents and heats of fusion of diopside, albite, sanidine and nepheline. *Am. Mineral.* 68, 717-731.
- Stebbins, J.F., Carmichael, L.S.E., Moret, L.K. (1984). Heat capacity and entropy of silicate liquids and glasses. *Contrib. Mineral. Petrol.* 86, 131-148.
- Stebbins, J.F., Xu, Z. (1997). NMR evidence for excess non-bridging oxygen in an aluminosilicate glass. *Nature* 390, 60-62.
- Stein, D.J. and Spera, F.J. (1993). Experimental rheometry of melts and supercooled liquids in the system NaAlSiO<sub>4</sub>-SiO<sub>2</sub>: implications for structure and dynamics. *Am. Mineral.* 78, 710-728.
- Stein, D.J. and Spera, F.J. (1995). Molecular dynamics simulations of liquids and glasses in the system NaAlSiO<sub>4</sub>-SiO<sub>2</sub>: methodology and melt structures. *Am. Mineral.* 80, 417-431.
- Stevenson, R.J., Dingwell, D.B., Webb, S.L. and Bagdassarov, N.S. (1995). The equivalence of enthalpy and shear stress relaxation in rhyolitic obsidian and quantification of the liquid-glass transition in volcanic processes. *J. Volcanol. Geoth. Res.* 68, 297-306.

- Stillinger, F.H. (1995). A topographic view of supercooled liquids and glass formation. *Science* 267, 1935-1939.
- Stolper, E. (1982). Water in silicate glasses: an infrared spectroscopic study. *Contrib. Mineral. Petrol.* 81, 1-17.
- Tammann, G. and Hesse, W. (1926). Die Abhängigkeit der Viskosität von der Temperatur bei unterkühlten Flüssigkeiten. *Zeitschrift für anorganische und allgemeine Chemie* 156, 245-257.
- Tauber, P. and Arndt, J. (1987): The relationship between viscosity and temperature in the system anorthite-diopside. *Chem. Geol.* 62, 71-81.
- Tobolsky, A.V. and Taylor, R.B. (1963). Viscoelastic properties of a simple organic glass. *J. Phys. Chemistry* 67, 2439-2442.
- Toplis, M.J. and Dingwell, D.B. (1996). The variable influence of P<sub>2</sub>O<sub>5</sub> on the viscosity of melts of differing alkali/aluminium ratio: implications for the structural role of phosphorus in silicate melts. *Geoch. Cosmoch. Acta* 60, 4107-4121.
- Toplis, M.J., Dingwell, D.B., Hess, K.-U., Lenci, T. (1997): Viscosity, fragility and configurational entropy of melts along the join SiO<sub>2</sub>-NaAlSiO<sub>4</sub>. *Am. Mineral.* 82, 979-990.
- Toplis, M.J. (1998): Energy barriers to viscous flow and the prediction of glass transition temperatures of molten silicates. *Am. Mineral.* 83, 480-490.
- Urbain, G., Bottinga, Y., Richet, P. (1982): Viscosity of silica, silicates and aluminosilicates. *Geochim. Cosmoch. Acta* 46, 1061-1071.
- Virgo, D. and Mysen, B.O. (1985). The structural state of iron in oxidized vs. reduced glasses at 1 atm: a <sup>57</sup>Fe Mossbauer study. *Physics and Chemistry of Minerals* 12, 65-76.
- Vogel, D.H. (1921). Temperaturabhängigkeitsgesetz der Viskosität von Flüssigkeiten. *Physikalische Zeitschrift* 22, 645-646.
- Waychunas, G.A., Apter, M.J., Brown, G.E. (1983). X-ray K-edge absorption spectra of Fe minerals and model compounds: Near-edge structure. *Physics and Chemistry of Minerals* 10, 1-9.
- Webb, S.L. (1992). Shear, volume, enthalpy and structural relaxation in silicate melts. *Chem. Geol.* 96, 449-457.
- Webb, S.L. and Dingwell, D.B. (1990). Non-Newtonian rheology of igneous melts at high stresses and strain-rates: experimental results for rhyolite, andesite, basalt and nephelinite. *J. Geophys. Res.* 95, 15695-15701.

- Webb, S.L., Knoche, R. And Dingwell, D.B. (1992). Determination of silicate liquid thermal expansivities using dilatometry and Calorimetry. *Eur. J. Mineral.* 4, 95-104.
- Webb, S.L. (1997) Silicate melts: relaxation, rheology, and the glass transition, *Rev. Geophys.* 35, 191-218.
- Whittington, A., Richet, P., Linard, Y., Holtz, F., (2000). Water and the viscosity of depolymerized aluminosilicate melts. *Geoch. Cosmoch. Acta* 64, 3725-3736.
- Whittington, A., Richet, P., Linard, Y., Holtz, F., (2001). The viscosity of hydrous phonolites and trachytes. *Chem. Geol.* 174, 209-223.
- Wilding, M., Webb, S.L. and Dingwell, D.B. (1995). Evaluation of a relaxation geothermometer for volcanic glasses. *Chem. Geol.* 125, 137-148.
- Wilding, M., Webb, S.L., Dingwell, D.B., Abla, G. and Marti, J. (1996). Cooling variation in natural volcanic glasses from Tenerife, Canary Islands. *Contrib. Mineral. Petrol.* 125, 151-160.
- Wilding, M., Dingwell, D.B., Batiza, R. and Wilson, L. (2000). Cooling rates of hyaloclastites: applications of relaxation geospeedometry to undersea volcanic deposits. *Bull. Volcanol.* 61, 527-536.
- Withers, A.C. and Behrens, H. (1999). Temperature induced changes in the NIR spectra of hydrous albite and rhyolitic glasses between 300 and 100 K. *Phys. Chem. Minerals* 27, 119-132.
- Zhang, Y., Jenkins, J. and Xu, Z. (1997). Kinetics of reaction  $H_2O + O = 2 OH$  in rhyolitic glasses upon cooling: geospeedometry and comparison with glass transition. *Geoch. Cosmoch. Acta* 11, 2167-2173.

Table 1: Compositions of the investigated samples : **a)** in terms of wt of the oxides; **b)** in molar basis.  
 The symbols refer to: + data from Dingwell et al. (1996); \* data from Whittington et al. (2001);  
 ^ data from Whittington et al. (2000); \*\*data from Neuville et al. (1993).

<b>(a)</b> <i>wt oxides</i>	<b>SiO<sub>2</sub></b>	<b>Al<sub>2</sub>O<sub>3</sub></b>	<b>FeO<sub>tot</sub></b>	<b>TiO<sub>2</sub></b>	<b>MnO</b>	<b>MgO</b>	<b>CaO</b>	<b>Na<sub>2</sub>O</b>	<b>K<sub>2</sub>O</b>	<b>P<sub>2</sub>O<sub>5</sub></b>	<b>Tot wt</b>	<b>alkalies</b>
<b>HPG8<sup>+</sup></b>	78.60	12.50	0.00	0.00	0.00	0.00	0.00	4.60	4.20	0.00	99.90	8.81
<b>Td_ph</b>	60.46	18.81	3.31	0.56	0.20	0.36	0.67	9.76	5.45	0.06	99.64	15.27
<b>W_Ph<sup>*</sup></b>	58.82	19.42	0.00	0.79	0.00	1.87	2.35	9.31	7.44	0.00	100.00	16.75
<b>W_T<sup>*</sup></b>	64.45	16.71	0.00	0.50	0.00	2.92	5.36	6.70	3.37	0.00	100.01	10.07
<b>Ves_W</b>	52.02	19.28	4.65	0.59	0.14	1.72	6.58	4.53	7.69	0.65	97.82	12.49
<b>Ves_G</b>	51.24	19.14	4.55	0.58	0.12	1.71	6.51	4.60	7.99	0.71	97.14	12.96
<b>AMS_B1</b>	60.10	18.03	3.43	0.38	0.14	0.73	2.92	4.49	7.89	0.16	98.27	12.61
<b>AMS_D1</b>	59.98	18.01	3.82	0.39	0.11	0.88	2.91	4.06	8.37	0.21	98.75	12.59
<b>MNV</b>	63.88	17.10	2.90	0.31	0.13	0.24	1.82	5.67	6.82	0.05	98.93	12.63
<b>ATN</b>	59.70	18.52	3.60	0.46	0.17	0.65	2.80	3.89	8.45	0.15	98.39	12.54
<b>PVC</b>	63.99	16.96	2.55	0.45	0.14	0.32	0.83	6.33	6.39	0.09	98.04	12.98
<b>UNZ</b>	66.00	15.23	4.08	0.36	0.10	2.21	5.01	3.84	2.16	0.14	99.13	6.05
<b>N_An<sup>**</sup></b>	61.17	17.29	5.39	0.84	0.00	3.35	5.83	3.85	1.39	0.00	99.11	5.29
<b>Ves_G_tot</b>	49.20	16.40	7.20	0.83	0.13	5.10	10.20	2.70	6.50	0.72	98.98	9.30
<b>Ves_W_tot</b>	51.20	18.60	6.10	0.67	0.13	2.50	7.30	3.75	7.90	0.40	98.55	11.82
<b>W_Tph<sup>^</sup></b>	50.56	14.03	0.00	2.35	0.00	8.79	15.00	7.04	3.01	0.00	100.78	9.97
<b>ETN</b>	47.03	16.28	10.13	1.61	0.20	5.17	10.47	3.75	1.94	0.59	97.18	5.85
<b>EIF</b>	41.15	12.10	10.11	2.74	0.00	11.24	15.66	2.76	3.04	1.02	99.82	5.81
<b>NIQ<sup>^</sup></b>	43.57	10.18	0.00	2.97	0.00	9.17	26.07	7.59	0.96	0.00	100.51	8.51
<b>IGC</b>	60.74	19.22	3.37	0.27	0.18	0.28	2.11	5.28	6.32	0.06	97.83	11.86

Table 1: (continued)

<i>(b)</i> <i>mole ox %</i>											<i>molar</i>	<i>basis</i>	<i>parameters</i>
	<b>SiO<sub>2</sub></b>	<b>Al<sub>2</sub>O<sub>3</sub></b>	<b>FeO<sub>tot</sub></b>	<b>TiO<sub>2</sub></b>	<b>MnO</b>	<b>MgO</b>	<b>CaO</b>	<b>Na<sub>2</sub>O</b>	<b>K<sub>2</sub>O</b>	<b>P<sub>2</sub>O<sub>5</sub></b>	<b>A.I.</b>	<b>NBO/T</b>	<b>SM</b>
<b>HPG8<sup>+</sup></b>	84.42	7.91	0.00	0.00	0.00	0.00	0.00	4.79	2.88	0.00	0.97	0.02	7.73
<b>Td_ph</b>	67.84	12.44	3.11	0.47	0.19	0.60	0.81	10.62	3.90	0.03	1.17	0.10	17.89
<b>W_Ph*</b>	65.41	12.72	0.00	0.66	0.00	3.10	2.80	10.03	5.28	0.00	1.20	0.19	21.27
<b>W_T*</b>	69.00	10.54	0.00	0.40	0.00	4.66	6.15	6.95	2.30	0.00	0.88	0.21	20.12
<b>Ves_W</b>	59.79	13.06	4.47	0.51	0.13	2.94	8.10	5.05	5.64	0.32	0.82	0.27	24.57
<b>Ves_G</b>	59.42	13.08	4.41	0.50	0.12	2.95	8.08	5.17	5.91	0.35	0.85	0.28	24.81
<b>AMS_B1</b>	68.56	12.12	3.27	0.32	0.14	1.24	3.56	4.97	5.74	0.08	0.88	0.10	17.50
<b>AMS_D1</b>	68.18	12.06	3.63	0.33	0.11	1.50	3.54	4.48	6.07	0.10	0.87	0.11	17.76
<b>MNV</b>	71.85	11.33	2.72	0.26	0.13	0.40	2.20	6.19	4.90	0.02	0.98	0.07	15.35
<b>ATN</b>	68.38	12.50	3.44	0.40	0.16	1.11	3.44	4.32	6.17	0.08	0.84	0.12	18.07
<b>PVC</b>	72.56	11.33	2.41	0.38	0.13	0.54	1.01	6.96	4.62	0.04	1.02	0.06	14.63
<b>UNZ</b>	71.30	9.70	3.68	0.30	0.09	3.56	5.80	4.02	1.49	0.06	0.57	0.16	17.37
<b>N_An**</b>	66.23	11.03	4.88	0.68	0.00	5.41	6.76	4.04	0.96	0.00	0.45	0.28	19.94
<b>Ves_G_tot</b>	55.16	10.84	4.48	0.70	0.12	8.52	12.25	2.93	4.65	0.34	0.70	0.50	31.15
<b>Ves_W_tot</b>	59.15	12.66	3.93	0.58	0.13	4.31	9.04	4.20	5.82	0.20	0.79	0.28	25.86
<b>W_Tph^</b>	51.32	8.39	0.00	1.79	0.00	13.30	16.31	6.93	1.95	0.00	1.06	0.86	38.53
<b>ETN</b>	51.94	10.60	9.36	1.34	0.19	8.52	12.40	4.01	1.36	0.28	0.51	0.43	30.51
<b>EIF</b>	43.28	7.50	6.47	2.17	0.00	17.62	17.65	2.81	2.04	0.45	0.65	1.16	44.75
<b>NIQ^</b>	42.98	5.92	0.00	2.20	0.00	13.48	27.55	7.26	0.60	0.00	1.33	1.51	48.93
<b>IGC</b>	69.74	13.00	3.23	0.23	0.18	0.49	2.60	5.88	4.63	0.03	0.81	0.04	15.58

**A.I.** = (Na<sub>2</sub>O+K<sub>2</sub>O)/Al<sub>2</sub>O<sub>3</sub>  
**NBO/T** = (Mysen, 1988)  
**SM** = sum (Fetot/2+MnO+MgO+CaO+Na<sub>2</sub>O+K<sub>2</sub>O)

Table 2.: Water contents, water speciatin and densities of the samples for which viscosity was measured.

Sample		H <sub>2</sub> O wt%			ρ	Thick	Absorbance at			H <sub>2</sub> O wt%	
n°	name	KFT_1	KFT_2	KFT_3			Aver. (Kg/m <sup>3</sup> )	(μm)	3500	4500	5200
							cm-1	cm-1	cm-1		
813	IGC	2.87	3.05		2.96	2484	-	-	-	-	
IGC1	IGC	1.98	2.03		2.01	2464	-	-	-	-	
IGC2	IGC	1.50	1.56	1.56	1.54	2471	-	-	-	-	
IGC5	IGC	3.39	3.43		3.41	2476	-	-	-	-	
800	ETN	1.09	1.18		1.13	2802	-	-	-	-	
801-2	ETN	0.63	0.63	0.66	0.64	2744	-	-	-	-	
802	ETN	2.27	2.35		2.31	2777	-	-	-	-	
803-2	ETN	2.98			2.98	2768	-	-	-	-	
Bet1	ETN	1.58	1.69		1.64	2796	-	-	-	-	
MNV4	MNV	3.66	4.06		3.86	2453	-	-	-	-	
805	MNV	2.35	2.47		2.41	2471	-	-	-	-	
806	MNV	1.37	1.40		1.39	2492	-	-	-	-	
G 637	Ves_G	-	-	-	-	2595	50	0.64	-	-	1.26
G 638	Ves_G	-	-	-	-	2582	21	0.43	-	-	2.04
G 639	Ves_G	-	-	-	-	2546	27	0.82	-	-	3.07
G dry	Ves_G	-	-	-	-	2586	-	-	-	-	0.02
W 640	Ves_W	-	-	-	-	2558	50	0.58	-	-	1.17
W 642	Ves_W	-	-	-	-	2496	27	0.87	-	-	3.32
W 643	Ves_W	-	-	-	-	2541	24	0.52	-	-	2.21
W dry	Ves_W	-	-	-	-	2549	-	-	-	-	0.02
D1 643	AMS_D1	-	-	-	-	2500	98	1.09	-	-	1.15
D1 639	AMS_D1	-	-	-	-	2413	31	1.09	-	-	3.75
D1 641	AMS_D1	-	-	-	-	2468	42	0.82	-	-	2.04
D1 641	AMS_D1	-	-	-	-	2485	42	0.82	-	-	2.02
D1 640	AMS_D1	-	-	-	-	2448	49	1.11	-	-	2.38
D1 dry	AMS_D1	-	-	-	-	2475	-	-	-	-	0.02
B1 642	AMS_B1	-	-	-	-	2503	82	0.63	-	-	0.79
B1 638	AMS_B1	-	-	-	-	2560	49	0.58	-	-	1.19
B1 637	AMS_B1	-	-	-	-	2396	31	1.09	-	-	3.78
B1 636	AMS_B1	-	-	-	-	2588	97	1.23	-	-	1.26
B1 dry	AMS_B1	-	-	-	-	2481	-	-	-	-	0.02
Tn.5	Td_ph	-	-	-	-	2461	1022	-	0.0967	0.0458	0.85
Tn.1	Td_ph	-	-	-	-	2506	1026	-	0.1084	0.0538	0.95
Tn.2	Td_ph	-	-	-	-	2423	1023	-	0.1730	0.1710	2.10
Tn.3	Td_ph	-	-	-	-	2442	1037	-	0.1920	0.4120	3.75

Table 3: Viscosity data for the dry compositions used in the modelling.

Name	T(C)	log $\eta$ (Pa s)	Name	T(C)	log $\eta$ (Pa s)
IGC	1495.50	2.37	AMS_B1	784.75	9.06
IGC	1470.89	2.49	AMS_D1	1495.50	2.49
IGC	1446.28	2.63	AMS_D1	1446.28	2.74
IGC	1421.67	2.77	AMS_D1	1397.06	3.01
IGC	1397.06	2.92	AMS_D1	1347.84	3.30
IGC	1372.45	3.08	AMS_D1	1298.62	3.62
IGC	1347.84	3.24	AMS_D1	1249.40	3.96
IGC	1323.23	3.40	AMS_D1	1200.18	4.33
IGC	1298.62	3.58	AMS_D1	1150.96	4.73
IGC	1274.01	3.76	AMS_D1	683.60	11.29
IGC	1249.40	3.94	AMS_D1	700.09	10.75
IGC	1224.79	4.14	AMS_D1	711.88	10.56
IGC	1200.18	4.34	AMS_D1	736.40	9.77
IGC	1175.57	4.54	AMS_D1	765.17	9.32
IGC	782.45	10.83	AMS_D1	813.95	8.45
IGC	803.10	10.44	Ves_W	1397.06	1.96
IGC	835.55	9.84	Ves_W	1347.84	2.25
IGC	860.70	9.32	Ves_W	1298.62	2.56
MNV	1495.50	2.50	Ves_W	1249.40	2.91
MNV	1470.89	2.62	Ves_W	1200.18	3.29
MNV	1446.28	2.75	Ves_W	1150.96	3.72
MNV	1421.67	2.89	Ves_W	1101.74	4.22
MNV	1397.06	3.03	Ves_W	1052.52	4.77
MNV	1372.45	3.18	Ves_W	689.20	10.68
MNV	1347.84	3.33	Ves_W	708.50	10.26
MNV	1323.23	3.49	Ves_W	722.95	9.97
MNV	1298.62	3.65	Ves_W	752.25	9.44
MNV	1274.01	3.82	Ves_W	755.12	9.01
MNV	1249.40	3.97	Ves_W	770.00	8.98
MNV	1224.79	4.17	Ves_G	1397.06	2.28
MNV	1200.18	4.36	Ves_G	1347.84	2.54
MNV	1175.57	4.55	Ves_G	1298.62	2.83
MNV	685.45	11.08	Ves_G	1249.40	3.15
MNV	743.80	10.03	Ves_G	1200.18	3.48
MNV	706.10	10.71	Ves_G	1150.96	3.87
MNV	816.80	8.76	Ves_G	1101.74	4.29
MNV	769.30	9.56	Ves_G	1052.52	4.75
AMS_B1	1446.28	2.79	Ves_G	688.95	11.05
AMS_B1	1397.06	3.06	Ves_G	707.25	10.66
AMS_B1	1347.84	3.35	Ves_G	726.70	10.20
AMS_B1	1298.62	3.67	Ves_G	756.35	9.78
AMS_B1	1249.40	4.02	Ves_G	771.15	9.58
AMS_B1	1200.18	4.39	Ves_G	805.10	8.81
AMS_B1	1150.96	4.80	Td_ph	1495.50	2.20
AMS_B1	693.93	11.18	Td_ph	1470.89	2.32
AMS_B1	732.45	10.39	Td_ph	1446.28	2.44
AMS_B1	768.25	9.41	Td_ph	1421.67	2.57

Table 3 (continued)

Name	T(C)	log $\eta$ (Pa s)	Name	T(C)	log $\eta$ (Pa s)
Td_ph	1397.06	2.70	VES_Gt	696.80	10.98
Td_ph	1372.45	2.83	VES_Gt	707.45	10.55
Td_ph	1347.84	2.97	VES_Gt	720.20	10.17
Td_ph	1323.23	3.11	VES_Gt	729.15	9.78
Td_ph	1298.62	3.26	VES_Gt	744.75	9.51
Td_ph	1274.01	3.42	VES_Gt	756.25	9.13
Td_ph	1249.40	3.57	VES_Gt	766.95	8.79
Td_ph	1224.79	3.74	VES_Wt	1544.72	0.97
Td_ph	1200.18	3.91	VES_Wt	1520.11	1.07
Td_ph	1175.57	4.07	VES_Wt	1495.50	1.17
Td_ph	1150.96	4.27	VES_Wt	1470.89	1.28
Td_ph	1126.35	4.46	VES_Wt	1446.28	1.38
Td_ph	1101.74	4.65	VES_Wt	1421.67	1.50
Td_ph	614.71	11.63	VES_Wt	1397.06	1.63
Td_ph	650.81	10.85	VES_Wt	1372.45	1.75
Td_ph	672.74	10.32	VES_Wt	1347.84	1.88
Td_ph	691.64	10.00	VES_Wt	705.00	10.66
Td_ph	737.26	8.99	VES_Wt	724.35	10.15
UNZ	1470.89	2.09	VES_Wt	743.25	9.75
UNZ	1446.28	2.21	HPG8+	1642.80	3.24
UNZ	1421.67	2.34	HPG8+	1593.60	3.58
UNZ	1397.06	2.48	HPG8+	1544.40	3.81
UNZ	1372.45	2.62	HPG8+	1495.20	4.15
UNZ	1347.84	2.76	HPG8+	1446.00	4.53
UNZ	1323.23	2.92	HPG8+	1396.80	4.90
UNZ	1298.62	3.08	HPG8+	881.70	11.02
UNZ	1274.01	3.25	HPG8+	905.00	10.63
UNZ	1249.40	3.43	HPG8+	925.70	10.28
UNZ	1224.79	3.61	HPG8+	938.80	10.16
UNZ	1200.18	3.80	HPG8+	1180.00	6.79
UNZ	1175.57	4.00	PVC	1593.94	2.14
UNZ	1150.96	4.21	PVC	1569.33	2.25
UNZ	1126.35	4.44	PVC	1544.72	2.37
UNZ	1101.74	4.66	PVC	1520.11	2.50
UNZ	761.00	10.50	PVC	1495.50	2.63
UNZ	784.65	9.85	PVC	1470.89	2.76
UNZ	801.00	9.28	PVC	1446.28	2.91
UNZ	818.00	8.91	PVC	1421.67	3.05
VES_Gt	1544.72	0.53	PVC	1397.06	3.20
VES_Gt	1520.11	0.62	PVC	1372.45	3.36
VES_Gt	1495.50	0.71	PVC	1347.84	3.52
VES_Gt	1470.89	0.81	PVC	1323.23	3.68
VES_Gt	1446.28	0.90	PVC	1298.62	3.85
VES_Gt	1421.67	1.01	PVC	1274.01	4.00
VES_Gt	1397.06	1.12	PVC	1249.40	4.21
VES_Gt	1372.45	1.24	PVC	1224.79	4.40
VES_Gt	1347.84	1.36	PVC	1200.18	4.59

Table 3 (continued)

Name	T(C)	log $\eta$ (Pa s)	Name	T(C)	log $\eta$ (Pa s)
PVC	722.88	10.77	W_T*	725.25	11.14
PVC	737.15	10.53	W_T*	721.05	11.23
PVC	738.59	10.41	W_T*	708.65	11.67
PVC	743.13	10.49	W_T*	700.15	11.96
PVC	749.70	10.19	W_T*	677.95	12.77
PVC	760.60	9.95	W_ph*	1542.35	1.92
PVC	781.80	9.63	W_ph*	1492.85	2.12
PVC	806.55	9.11	W_ph*	1448.75	2.33
EIF	1470.89	-0.22	W_ph*	1396.25	2.57
EIF	1446.28	-0.16	W_ph*	1344.25	2.86
EIF	1421.67	-0.09	W_ph*	773.25	8.66
EIF	1397.06	-0.02	W_ph*	761.65	8.97
EIF	1372.45	0.07	W_ph*	753.65	9.15
EIF	1347.84	0.16	W_ph*	742.05	9.38
EIF	691.85	10.77	W_ph*	731.95	9.62
EIF	702.00	10.26	W_ph*	716.85	9.97
EIF	709.60	9.81	W_ph*	700.15	10.39
EIF	710.00	10.05	W_ph*	689.35	10.67
ETN	1544.72	0.18	W_ph*	679.15	10.94
ETN	1520.11	0.26	W_ph*	668.35	11.29
ETN	1495.50	0.34	W_ph*	659.05	11.55
ETN	1470.89	0.43	W_ph*	646.85	11.96
ETN	1446.28	0.52	W_ph*	637.85	12.25
ETN	1421.67	0.62	W_ph*	625.05	12.71
ETN	1397.06	0.72	W_ph*	616.05	13.12
ETN	731.63	10.23	W_Tf^	1445.45	0.50
ETN	711.85	10.82	W_Tf^	1393.05	0.70
ETN	715.85	10.70	W_Tf^	1341.25	0.91
W_T*	1655.55	1.46	W_Tf^	1291.85	1.13
W_T*	1606.45	1.64	W_Tf^	1240.05	1.38
W_T*	1554.55	1.86	W_Tf^	1224.35	1.45
W_T*	1503.35	2.09	W_Tf^	1190.35	1.65
W_T*	1452.65	2.32	W_Tf^	1140.75	1.96
W_T*	1404.65	2.56	W_Tf^	734.95	8.73
W_T*	1355.35	2.83	W_Tf^	724.05	9.18
W_T*	1304.85	3.12	W_Tf^	718.95	9.30
W_T*	1258.55	3.41	W_Tf^	713.55	9.57
W_T*	840.55	8.37	W_Tf^	709.95	9.71
W_T*	829.95	8.58	W_Tf^	703.15	9.93
W_T*	818.85	8.81	W_Tf^	698.05	10.21
W_T*	809.45	8.99	W_Tf^	694.15	10.38
W_T*	792.65	9.34	W_Tf^	687.45	10.61
W_T*	784.05	9.53	W_Tf^	683.55	10.75
W_T*	771.85	9.82	W_Tf^	673.25	11.32
W_T*	762.95	10.04	W_Tf^	660.95	11.86
W_T*	741.45	10.59	W_Tf^	657.55	12.05
W_T*	726.05	11.09	W_Tf^	644.85	12.85

Table 3 (continued)

Name	T(C)	log $\eta$ (Pa s)	Name	T(C)	log $\eta$ (Pa s)
NIQ^	1300.00	0.41	N_an**	752.35	10.90
NIQ^	719.55	8.66	N_an**	738.65	11.25
NIQ^	709.75	8.94	N_an**	719.05	11.83
NIQ^	704.25	9.16	N_an**	707.95	12.33
NIQ^	698.85	9.35	N_an**	698.65	12.64
NIQ^	693.25	9.57	N_an**	688.55	12.85
NIQ^	686.35	9.88	N_an**	677.45	13.30
NIQ^	685.05	9.93	N_an**	666.15	13.66
NIQ^	679.65	10.17	ATN	1470.89	2.45
NIQ^	671.55	10.51	ATN	1446.28	2.58
NIQ^	667.75	10.75	ATN	1421.67	2.72
NIQ^	660.95	11.04	ATN	1347.84	3.16
NIQ^	656.05	11.26	ATN	1323.23	3.32
NIQ^	651.05	11.56	ATN	1298.62	3.48
NIQ^	645.55	11.83	ATN	1274.01	3.66
NIQ^	640.45	12.16	ATN	1249.40	3.83
NIQ^	638.95	12.22	ATN	1224.79	4.02
NIQ^	626.05	12.99	ATN	1200.18	4.20
NIQ^	619.15	13.40	ATN	1175.57	4.40
NIQ^	613.35	13.70	ATN	1150.96	4.60
N_an**	1593.85	2.33	ATN	761.4	10.30
N_an**	1544.85	2.52	ATN	774.5	10.11
N_an**	1494.85	2.74	ATN	794.3	9.73
N_an**	1445.85	2.97	ATN	810.6	9.55
N_an**	1396.85	3.19	ATN	830.9	9.11
N_an**	763.65	10.67			

The symbol

+ refers to data from Dingwell et al. (1996)

\* refers to data from Whittington et al. (2001)

^ refers to data from Whittington et al. (2000)

\*\*refers to data from Neuville et al. (1993).

Table 4: Pre-exponential factor ( $A_{TVF}$ ), pseudo-activation-energy ( $B_{TVF}$ ) and TVF temperature values ( $T_0$ ) obtained by fitting the experimental determinations via Eqs. 2.9. Glass transition temperatures defined as the temperature at  $10^{11}$  ( $T_{11}$ ) Pa s and the  $T_g$  determined using calorimetry (calorim  $T_g$ ). Fragility  $F$  defined as the ratio  $T_0/T_g$  and the fragilities calculated as a function of the NBO/T ratio (Eq. 5.2).

Sample	$A_{TVF}$ (Pa s)	$B_{TVF}$ (K)	$T_0$ (K)	$T_g=T_{11}$ (K)	calorim $T_g$ (K)	$F$	$F$ calc. Eq. 5.2
SiO <sub>2</sub> *	-7.26	26984	0	1477.60	1480	0.00	-
HPG8 <sup>o</sup>	-7.32	18859	128.39	1157.74		0.11	0.07
Td_ph	-4.94	11069	220.81	915.31	917	0.24	0.33
W_ph <sup>^</sup>	-3.22	7009	458.59	951.40		0.48	0.44
W_T <sup>^</sup>	-3.61	7201	510.12	1002.98		0.51	0.47
Ves_W	-6.76	12183	265.80	951.80		0.28	0.33
Ves_G	-6.34	11559	304.77	971.33		0.31	0.35
AMS_B1	-3.82	9056	362.22	973.22		0.37	0.33
AMS_D1	-3.86	9108	350.20	963.15		0.36	0.35
MNV	-6.05	13654	165.02	965.91	981	0.17	0.24
ATN	-4.99	10078	382.53	1012.70	996	0.38	0.35
PVC	-5.68	13004	205.45	985.01	980	0.21	0.24
UNZ	-3.63	6879	545.14	1015.42	1005	0.54	0.41
N_an	-2.97	7184	508.67	1022.93		0.50	0.54
VesGt	-4.98	6987	531.99	969.35	972	0.55	0.52
VesWt	-5.05	8070	467.16	969.79	985	0.48	0.54
W_Tph#	-3.93	4663	639.99	952.39		0.67	0.68
ETN	-4.84	6019	602.38	982.35	995	0.61	0.66
EIF	-4.24	4171	687.91	961.56	972	0.72	0.68
NIQ#	-5.06	5289	605.55	934.94		0.65	0.68
Di <sup>†</sup>	-4.42	4351	728.15	1011.14	1005	0.72	0.68

\*Data from Toplis et al. (1997);

<sup>o</sup> Regression using data from Dingwell et al. (1996)

<sup>^</sup> Regression using data from Whittington et al. (2001)

# Regression using data from Whittington et al. (2000)

<sup>†</sup> Regression using data from Sipp et al. (2001); Scarfe & Cronin (1983); Tauber & Arndt (1986); Urbain et al. (1982);

\*\* Regression using data from Neuville et al. (1993)

The calorimetric  $T_g$  for SiO<sub>2</sub> and Di are taken from Richet & Bottinga (1995).

Table 5: Results of fitting viscosity data on alkali trachyte (AMS\_D1; Table 1) to TVF equation.

Parameter	3-D <sub>proj</sub>		2-D Error Envelopes (1 $\sigma$ )			Covariance		
	Values	1 $\sigma$ <sup>1</sup>	at Solution			[A:i]	[B:i]	[T <sub>0</sub> :i]
			$A_{TVF}$	$B_{TVF}$	$T_0$			
$A_{TVF}$	-3.74	2.96	-	0.27	0.45	0.70	-1290	60.5
$B_{TVF}$	8906	5509	498	-	381	-1290	2407926	-113476
$T_0$	359	260	39.8	18.0	-	60.5	-113476	5373
min $\chi^2$		381 <sup>2</sup>						

Table 6: Compilation of viscosity data for haplogranitic melt with addition of 20 wt. % Na<sub>2</sub>O. Data include results of high-T concentric cylinder (CC) and low-T micropenetration (MP) techniques and centrifuge assisted falling sphere (CFS) viscometry.

T(K)	log $\eta$ (Pa s) <sup>1</sup>	Method	Source <sup>2</sup>
1571	1.40	CC	H
1522	1.58	CC	H
1473	1.77	CC	H
1424	1.98	CC	H
1375	2.21	CC	H
1325	2.46	CC	H
1276	2.74	CC	H
1227	3.07	CC	H
1178	3.42	CC	H
993	5.73	CFS	D
993	5.58	CFS	D
993	5.60	CFS	D
973	5.99	CFS	D
903	7.29	CFS	D
1043	4.99	CFS	D
1123	4.00	CFS	D
822.5	9.35	MP	H
795.5	10.10	MP	H
777.4	10.90	MP	H
755.4	11.90	MP	H

<sup>1</sup> Experimental uncertainty (1  $\sigma$ ) is 0.1 units of log  $\eta$ .

<sup>2</sup> Sources include: (H) Hess et al. (1995) and (D) Dorfman et al. (1996).

Table 7: Summary of results for fitting subsets of viscosity data for HPG8 + 20 wt. % Na<sub>2</sub>O to the TVF equation (see Table 3; after Hess et al. 1995 and Dorfman et al. 1996).

Data Subsets	N	$\chi^2$	Parameter Values			Projected 1 $\sigma$ Limits [Maximum - Minimum]		
			$A_{TVF}$	$B_{TVF}$	$T_0$	$\Delta A$	$\Delta B$	$\Delta C$
1 MP & CFS	11	4.0	-2.85	4784	429	4.54	4204	193
2 CC & CFS	16	3.4	-2.35	4060	484	3.70	3661	283
3 MP & CC	13	2.2	-2.38	4179	463	1.82	2195	123
4 ALL Data	20	7.1	-2.76	4672	436	1.57	1809	98

Table 8: Results of fitting viscosity data<sup>1</sup> on albite and diopside melts to the TVF equation

	Albite	Diopside
N	47	53
T(K) range	1099 - 2003	989 - 1873
$A_{TVF}$ [min - max]	-6.46 [-14.6 to -2.8]	-4.66 [-6.3 to -3.6]
$B_{TVF}$ [min - max]	14,816 [7,240 to 40,712]	4,514 [3,306 to 6,727]
$T_0$ [min - max]	288 [-469 to 620]	718 [611 to 783]
$\chi^2$	5.57	8.41

<sup>1</sup> Sources include: Urbain et al. (1982), Scarfe et al. (1983), N'Dala et al. (1984), Tauber and Arndt (1987), Dingwell (1989).

Table 9: Viscosity calculations via Eq. 5.7 and comparison through the residuals with the results from Eq. 2.9.

T (°C)	1600	1500	1400	1300	1200	1100	1000	900	800	700
<i>Viscosities calculated on the basis of Eq. 5.7</i>										
SiO <sub>2</sub>	7.01	7.84	8.77	9.80	10.99	12.34	13.92	15.75	17.94	20.56
HPG8	3.92	4.51	5.18	5.93	6.80	7.81	8.98	10.36	11.96	13.73
Td_ph	1.80	2.26	2.80	3.42	4.15	5.02	6.09	7.42	9.15	11.52
W_ph	1.30	1.74	2.24	2.84	3.54	4.39	5.45	6.80	8.59	11.13
W_T	1.46	1.90	2.41	3.01	3.72	4.58	5.65	6.99	8.76	11.24
Ves_W	0.95	1.37	1.86	2.44	3.13	3.97	5.02	6.38	8.22	10.88
Ves_G	0.91	1.33	1.82	2.39	3.08	3.92	4.97	6.34	8.18	10.85
AMS_B1	1.86	2.33	2.86	3.49	4.22	5.09	6.17	7.50	9.22	11.57
AMS_D1	1.83	2.29	2.83	3.45	4.18	5.05	6.12	7.46	9.18	11.54
MNV	2.22	2.70	3.26	3.90	4.65	5.55	6.63	7.96	9.64	11.87
ATN	1.92	2.39	2.93	3.55	4.29	5.17	6.24	7.58	9.29	11.62
PVC	2.35	2.84	3.40	4.05	4.81	5.71	6.80	8.13	9.80	11.99
UNZ	1.94	2.41	2.95	3.58	4.31	5.19	6.27	7.60	9.31	11.63
N_An	1.52	1.96	2.48	3.08	3.80	4.66	5.72	7.07	8.83	11.29
Ves_Gt	0.30	0.69	1.15	1.70	2.36	3.19	4.24	5.63	7.57	10.45
Ves_Wt	0.80	1.21	1.70	2.27	2.95	3.79	4.84	6.21	8.06	10.77
W_Teph	-0.27	0.09	0.53	1.06	1.70	2.52	3.57	5.00	7.03	10.11
ETN	0.27	0.65	1.11	1.66	2.32	3.14	4.20	5.59	7.53	10.43
EIF	-0.56	-0.21	0.22	0.74	1.37	2.18	3.25	4.69	6.77	9.96
NIQ	-0.84	-0.50	-0.08	0.43	1.06	1.87	2.93	4.40	6.53	9.81
<i>Residuals Eq. 2.9 – Eq. 5.7</i>										
SiO <sub>2</sub>	0.14	0.12	0.10	0.09	0.06	0.05	0.01	-0.01	-0.06	-0.09
HPG8	-0.43	-0.37	-0.29	-0.20	-0.10	0.02	0.17	0.37	0.68	1.27
Td_ph	-0.04	-0.07	-0.11	-0.17	-0.24	-0.35	-0.51	-0.74	-1.10	-1.74
W_ph	0.43	0.37	0.30	0.23	0.14	0.05	-0.07	-0.21	-0.41	-0.73
W_T	0.22	0.19	0.17	0.15	0.14	0.15	0.18	0.26	0.42	0.70
Ves_W	-0.13	-0.05	0.04	0.12	0.20	0.27	0.31	0.28	0.11	-0.41
Ves_G	0.11	0.20	0.29	0.38	0.47	0.56	0.62	0.63	0.52	0.10
AMS_B1	0.31	0.27	0.22	0.17	0.11	0.04	-0.05	-0.15	-0.30	-0.56
AMS_D1	0.29	0.25	0.20	0.14	0.08	-0.01	-0.11	-0.25	-0.44	-0.78
MNV	-0.27	-0.26	-0.25	-0.25	-0.26	-0.29	-0.36	-0.46	-0.66	-1.03
ATN	-0.15	-0.14	-0.11	-0.08	-0.04	0.01	0.08	0.18	0.31	0.45
PVC	-0.23	-0.22	-0.22	-0.22	-0.23	-0.25	-0.30	-0.37	-0.49	-0.73
UNZ	-0.39	-0.44	-0.48	-0.51	-0.53	-0.51	-0.45	-0.27	0.09	0.81
N_An	0.78	0.75	0.72	0.69	0.68	0.68	0.70	0.78	0.93	1.21
Ves_Gt	-0.07	-0.04	0.00	0.04	0.09	0.14	0.21	0.29	0.37	0.41
Ves_Wt	-0.12	-0.09	-0.06	-0.03	0.02	0.06	0.12	0.17	0.20	0.12
W_Teph	0.13	0.10	0.06	0.02	-0.03	-0.08	-0.13	-0.18	-0.19	-0.04
ETN	-0.37	-0.35	-0.33	-0.30	-0.25	-0.18	-0.06	0.12	0.42	0.97
EIF	-0.17	-0.19	-0.23	-0.27	-0.31	-0.34	-0.36	-0.34	-0.19	0.42
NIQ	-0.05	-0.03	-0.03	-0.02	-0.02	-0.04	-0.07	-0.14	-0.28	-0.48

Table 10: Comparison of the regression parameters obtained via Eq. 5.7 (composition-dependent and temperature-independent) with those deriving Eq. 5. (composition- and temperature-dependent).

T (°C)	$c_1$	$c_1(T)$	Residual	$c_2$	$c_2(T)$	Residual	$c_3$	$c_3(T)$	Residual
1600	19.695	19.488	0.207	10.999	11.038	-0.039	-3.994	-4.146	0.152
1500	19.026	18.996	0.030	11.579	11.559	0.020	-3.739	-3.802	0.063
1400	18.311	18.414	-0.103	12.152	12.119	0.032	-3.386	-3.386	0.000
1300	17.594	17.714	-0.120	12.744	12.712	0.032	-2.942	-2.873	-0.069
1200	16.727	16.855	-0.129	13.326	13.316	0.010	-2.335	-2.225	-0.110
1100	15.732	15.779	-0.046	13.846	13.876	-0.031	-1.502	-1.378	-0.123
1000	14.433	14.388	0.045	14.228	14.280	-0.051	-0.308	-0.228	-0.080
900	12.649	12.522	0.127	14.289	14.315	-0.026	1.463	1.426	0.037
800	9.920	9.887	0.033	13.731	13.666	0.065	4.214	4.008	0.206
700	5.842	5.887	-0.045	12.030	12.045	-0.015	8.529	8.603	-0.075

Table 11: Viscometry and differential scanning calorimetry results.

Sample	viscometry				calorimetry		
	T (°C)	10000/T (K <sup>-1</sup> )	log <sub>10</sub> η (Pa s)	q (K/min)	log <sub>10</sub> q (K/s)	T <sub>g</sub> (°C)	10000/T <sub>g</sub> (K <sup>-1</sup> )
EIF	680	10.49	11.41	5	-1.08	695	10.33
	692	10.36	10.77	10	-0.78	699	10.28
	702	10.25	10.26	20	-0.48	706	10.21
	710	10.17	9.94				
	740	9.87	8.69				
ETN	673	10.57	11.65	5	-1.08	712	10.15
	731	9.96	10.23	10	-0.78	722	10.05
	747	9.80	9.94	15	-0.60	729	9.98
				20	-0.48	735	9.92
R839-5.8	678	10.51	10.47	5	-1.08	663	10.68
	689	10.39	10.00	8	-0.88	669	10.62
	696	10.32	9.68	10	-0.78	672	10.58
	712	10.15	9.14	16	-0.57	678	10.51
	731	9.96	8.73	20	-0.48	681	10.48
Ves_W_tot	705	10.22	10.66	5	-1.08	700	10.28
	724	10.03	10.15	10	-0.78	712	10.15
	743	9.84	9.85	20	-0.48	723	10.04
Ves_G_tot	729	9.98	9.78	5	-1.08	691	10.38
	745	9.82	9.51	10	-0.78	699	10.28
	756	9.71	9.13	20	-0.48	712	10.15
	767	9.61	8.79				
PVC	723	10.04	10.77	5	-1.08	696	10.32
	739	9.88	10.41	10	-0.78	707	10.20
	750	9.78	10.19	20	-0.48	721	10.06
	761	9.67	9.95				
	782	9.48	9.63				

Table 11 (continued)

Sample	viscometry			calorimetry			
	T (°C)	$10^4/T$ (K <sup>-1</sup> )	$\log_{10} \eta$ (Pa s)	q (K/min )	$\log_{10} q$ (K/s)	$T_g$ (°C)	$10000/T_g$ (K <sup>-1</sup> )
MNV	696	10.32	11.32	5	-1.08	699	10.29
	744	9.83	10.83	10	-0.78	708	10.19
	757	9.71	10.71	20	-0.48	721	10.06
	795	9.36	10.36				
ATN	761	9.67	10.30	5	-1.08	708	10.19
	775	9.55	10.11	10	-0.78	723	10.04
	794	9.37	9.73	20	-0.48	735	9.92
	831	9.06	9.11				
Td_ph	615	11.26	11.63	5	-1.08	634	11.03
	651	10.82	10.85	8	-0.88	640	10.95
	673	10.57	10.32	10	-0.78	643	10.91
	692	10.37	10.00	16	-0.57	654	10.79
	737	9.90	8.99	20	-0.48	659	10.72
UNZ	774	9.55	9.90	5	-1.08	722	10.05
	801	9.31	9.28	10	-0.78	732	9.95
	818	9.16	8.91	20	-0.48	744	9.83
P3RR	720	10.06	11.10	5	-1.08	713	10.14
	738	9.89	10.78	8	-0.88	722	10.05
	770	9.59	10.18	10	-0.78	730	9.97
	811	9.23	9.56	16	-0.57	742	9.85
	841	8.98	9.15	20	-0.48	746	9.81

Table 12: Comparison of parameters derived from viscometry and differential scanning calorimetry

Sample	Viscosity measurements		DSC measurements		Shift factor
	$\log_{10} A\eta$	$E\eta$ (kJ/mol)	$\log_{10} A_{DSC}$	$E_{DSC}$ (kJ/mol)	
EIF	-34.4±0.2	845±70	-51.1 ±0.1	915±68	9.64±0.08
ETN	-20.3±0.1	516±42	-25.3 ±0.1	524±28	9.72±0.08
R839-5.8	-22.9±0.1	613±38	-30.8 ±0.1	577±38	9.81±0.07
Ves_G_tot	-17.6±0.1	533±35	-26.9 ±0.3	514±33	9.80±0.07
Ves_W_tot	-10.9±0.0	488±29	-24.6 ±0.1	484±34	9.84±0.06
PVC	-10.8±0.1	417±19	-21.4 ±0.2	421±87	10.17±0.08
MNV	-7.1±0.1	387±30	-25.6 ±0.2	422±39	10.14±0.08
ATN	-8.3±0.1	390±31	-21.5 ±0.2	417±48	10.18±0.10
MB5-6.61 <sup>§</sup>	-9.8±0.2	365±38	-20.3 ±0.2	372±37	10.03±0.08
Td_ph	-10.0±0.1	373±28	-21.2 ±0.2	380±32	10.16±0.08
UNZ	-15.6±0.1	490±33	-25.1 ±0.1	518±26	10.10±0.09
P3RR	-7.0±1.2	349±23	-16.7 ±0.1	338±21	10.24±0.08
BL6*	-8.6±0.1	389±14	-19.5 ±0.1	391±33	10.80±0.16
EDF*	-7.1±0.1	374±22	-18.6 ±0.1	396±25	10.39±0.16
LGB*	-7.9±0.1	387±8	-19.8 ±0.1	412±14	10.61±0.15
8 ka*	-8.8±0.1	327±12	-18.7 ±0.1	322±31	10.21±0.16
KE5*	-8.6±0.1	297±8	-17.9 ±0.1	287±10	10.07±0.16

<sup>§</sup> data from Gottsmann and Dingwell (2001b).

\* data from Stevenson et al. (1995).

Table 13.: Viscosities of hydrous samples from this study. Viscosities of the samples W\_T, W\_ph (Whittington et al., 2001) and HD (Hess and Dingwell, 1996) are not reported.

Sampl	T (°C)	log [ $\eta$ (Pas)]	H <sub>2</sub> O (wt%)	Sample	T (°C)	log [ $\eta$ (Pas)]	H <sub>2</sub> O (wt%)
ETN	575.2	11.60	0.64	MNV	400	10.80	3.86
ETN	597.2	10.80	0.64	MNV	398	10.79	3.86
ETN	601.9	10.74	0.64	MNV	385	11.60	3.86
ETN	611.6	10.50	0.64	MNV	515	9.67	2.41
ETN	618.5	10.42	0.64				
ETN	619.4	10.33	0.64	AMSB1	585.9	10.70	0.79
ETN	553.2	10.99	1.13	AMSB1	628.4	9.88	0.79
ETN	557.9	10.89	1.13	AMSB1	686.3	8.83	0.79
ETN	564.5	10.73	1.13	AMSB1	567.6	11.35	0.79
ETN	575.3	10.37	1.13	AMSB1	571.9	10.01	1.19
ETN	532.3	11.20	1.64	AMSB1	554.4	10.24	1.19
ETN	544.6	10.88	1.64	AMSB1	589.6	9.54	1.19
ETN	549.2	10.57	1.64	AMSB1	529.7	10.74	1.19
ETN	551.7	10.54	1.64	AMSB1	525.1	11.02	1.19
ETN	556.8	10.25	1.64	AMSB1	513.3	11.56	1.19
ETN	576.8	9.75	1.64	AMSB1	557.7	10.09	1.26
ETN	524.6	10.16	2.31	AMSB1	541.0	10.56	1.26
ETN	534.8	9.77	2.31	AMSB1	580.6	9.74	1.26
ETN	544.9	9.57	2.31	AMSB1	538.1	10.62	1.26
				AMSB1	599.7	9.33	1.26
IGC	562	11.12	0.81	AMSB1	526.0	10.85	1.26
IGC	569	10.94	0.81	AMSB1	521.5	11.19	1.26
IGC	579	10.75	0.81	AMSB1	425.6	10.52	3.78
IGC	595	10.44	0.81	AMSB1	451.1	9.85	3.78
IGC	596	10.30	0.81	AMSB1	404.2	11.43	3.78
IGC	604	10.09	0.81	AMSB1	420.2	10.95	3.78
IGC	529	10.86	1.52	AMSB1	444.9	10.05	3.78
IGC	546	10.36	1.52	AMSB1	406.3	11.33	3.78
IGC	553	10.14	1.52				
IGC	508	10.52	2.01	AMSC1	576.7	10.42	1.15
IGC	506	10.44	2.01	AMSC1	591.9	10.08	1.15
IGC	529	9.92	2.01	AMSC1	612.3	9.72	1.15
IGC	538	9.92	2.01	AMSC1	644.3	9.04	1.15
IGC	459	10.76	2.96	AMSC1	546.5	11.24	1.15
IGC	467	10.27	2.96	AMSC1	502.6	10.80	2.04
IGC	418	11.28	3.41	AMSC1	522.3	10.20	2.04
IGC	442	10.45	3.41	AMSC1	548.5	9.55	2.04
IGC	457	9.88	3.41	AMSC1	490.7	11.04	2.04
				AMSC1	521.4	9.70	2.38
MNV	566	10.64	1.00	AMSC1	488.1	10.65	2.38
MNV	575	10.47	1.00	AMSC1	503.5	10.05	2.38
MNV	589	10.22	1.00	AMSC1	470.7	10.97	2.38
MNV	597	10.08	1.00	AMSC1	436.2	10.31	3.75
MNV	515	10.97	1.39	AMSC1	415.7	11.05	3.75
MNV	545	10.31	1.39	AMSC1	450.5	9.90	3.75
MNV	570	9.90	1.39				
MNV	472	10.59	2.41				

Table 13.: (continued).

Sample	T (°C)	log [ $\eta$ (Pas)]	H <sub>2</sub> O (wt%)
Ves_W	532.4	10.64	1.17
Ves_W	545.7	10.32	1.17
Ves_W	567.5	9.84	1.17
Ves_W	516.4	11.05	1.17
Ves_W	586.9	9.20	1.17
Ves_W	594.2	9.17	1.17
Ves_W	526.8	8.90	2.21
Ves_W	505.4	9.40	2.21
Ves_W	473.6	10.29	2.21
Ves_W	454.6	9.82	3.32
Ves_W	480.6	9.32	3.32
Ves_W	431.2	10.82	3.32
Ves_W	444.5	10.25	3.32
Ves_W	475.6	9.46	3.32
Ves_G	542.2	10.35	1.26
Ves_G	563.6	9.71	1.26
Ves_G	510.0	11.29	1.26
Ves_G	575.1	9.40	1.26
Ves_G	461.3	11.00	2.04
Ves_G	486.3	10.16	2.04
Ves_G	505.9	9.62	2.04
Ves_G	522.0	9.16	2.04
Ves_G	444.5	10.33	3.07
Ves_G	462.9	9.84	3.07
Ves_G	435.7	10.61	3.07
Td_ph	593.9	8.79	0.85
Td_ph	531.4	10.33	0.85
Td_ph	520.8	10.59	0.85
Td_ph	507.3	11.05	0.85
Td_ph	548.6	9.90	0.85
Td_ph	490.6	10.84	0.95
Td_ph	501.8	10.82	0.95
Td_ph	505.3	10.45	0.95
Td_ph	512.5	10.25	0.95
Td_ph	469.0	10.16	2.10
Td_ph	455.2	10.55	2.10
Td_ph	485.9	9.59	2.10
Td_ph	430.2	9.57	3.75
Td_ph	389.7	11.00	3.75
Td_ph	402.2	10.50	3.75

Table 14.: Values of the calibrated parameters of Eqs. 6.1/6.3.

Sample	$a_1$	$a_2$	$b_1$	$b_2$	$c_1$	$c_2$
Td_Ph	-5.8996	-0.2857	10775	-394.83	148.71	-21.65
W_Ph	-3.0850	0.0519	7127	-419.51	305.42	-37.87
V1631	-6.7898	-0.0265	12143	-541.20	145.14	-33.34
AMS	-3.5405	0.1447	9619	-498.79	191.78	-35.52
MNV	-5.8630	-0.0509	12747	-673.50	103.42	-25.99
IGC	-4.4152	0.0981	9243	-428.05	255.35	-55.15
W_Tr	-2.2091	0.4879	7873	-552.28	304.91	-47.85
ETN	-4.6430	0.0000	5812	-427.04	499.31	-28.74
HPG8	-6.6955	-0.1056	15864	-623.50	3.93	-63.34

Values correspond to use of wt% H<sub>2</sub>O and absolute temperature in the equations, and restitute viscosity in Pa·s.

## **Tabellarischer Lebenslauf**

Name: Giordano

Vorname: Daniele

Anschrift: Via De Sanctis n° 28, 56123 - Pisa, Italia

Adelheidstr. 17, 80798 München, c/o Zech

Geburtsdatum: 01/07/1967

Geburtsort: Pisa, Italien

Staatsangehörigkeit: Italienisch

Familienstand: verheiratet

Kinder: 2

Tel.: 0039-050-552085 (Italien); 0049-89-21804272 (Deutschland)

Fax: 0039-050-221433

Email Adresse: [giordano@min.uni-muenchen.de](mailto:giordano@min.uni-muenchen.de);

[daniele\\_giordano@hotmail.com](mailto:daniele_giordano@hotmail.com)

---

## **Ausbildung**

1967 geboren an 01 July, Pisa, Italien

Eltern: Marco Giordano und Loredana Coleti;

seit 03 July 1999 verheiratet mit Erika Papi

1980-1986 Gymnasium

1986-1990 Biennium an der Physik Fakultät - Universität Pisa

1991-1997 Hochschulabschluss an der Fakultät Geologie – Universität Pisa